Max Planck Institute of Colloids and Interfaces

Cellulose Based Transition Metal Nano-Composites

Structuring and Development

Dissertation

zur Erlangung des akademischen Grades
“doctor rerum naturalium”
(Dr. rer. nat.)
in der Wissenschaftsdisziplin “Kolloidchemie“

eingereicht an der
Mathematisch-Naturwissenschaftlichen Fakultät
der Universität Potsdam

von
Stefan Glatzel
aus Berlin

Potsdam, November 2012

Published online at the
Institutional Repository of the University of Potsdam:
URL http://opus.kobv.de/ubp/volltexte/2013/6467/
URN urn:nbn:de:kobv:517-opus-64678
http://nbn-resolving.de/urn:nbn:de:kobv:517-opus-64678

CONTENT

Content i

I. Introduction 1

Patterns in the Work 1

II. Fundamentals 5

Nanoparticles 5

Carbides 6

Graphitisation 7

Patterning Techniques 8

III. Catalytic Graphitisation 11

Introduction 11

Synthesis and Analysis 11

Mechanism 23

Conclusions 24

IV. Ternary Carbides 27

Introduction 27

Synthesis 27

Tungsten-Iron-System 28

Manganese-Iron-System 33

V. Metal(0) Nanoparticles 43

Introduction 43

Copper-Iron-System 44

Nickel-Iron-System 50

Cobalt-Iron-System 56

VI. Structuring and Patterning 67

Introduction 67

Freestanding Origami Electrodes 68

Ink-Jet Printing 70

Conclusion and Prospect 77

VII. Green Synthesis and Applications 79

Introduction 79
Sunlight Driven Synthesis 80
Scrap Metal, Coffee Filters and some Wood 84
Dye-Filtration 87
Conclusion 88
VIII. Summary and Outlook 91
Outlook 94
IX. References 97
X. Appendix I
List of Abbreviations I
Chemicals and Analysis Techniques II
Additional Figures V
XI. Acknowledgments XXI
Eidesstattliche Erklärung / Statutory Declaration XXIII

I. INTRODUCTION

PATTERNS IN THE WORK

It takes only a few grams of paint, yet without means of ordering that paint in a controlled manner it will never become a Mona Lisa. As superficial and attention snatching as this statement may sound it does carry an important message: one cannot utilize a material – may it be old or novel – without a way of processing it. It is through processing that a raw material is given purpose; wood can become the foundation of a hut or a beautiful sculpture. Either way it fulfils a very important objective, but it needed to be converted from its raw state in order to do so.

Envisioning and synthesising new materials is undoubtedly the central facet of materials science but it is through the understanding of their formation, their properties and their behaviour that the most crucial point can be addressed: Control. Mankind has always been very resourceful when it came to shaping the world around us to our needs. Faced with challenges we invented new materials and techniques to overcome those obstacles, said techniques soon pervaded our entire society until we reached the boundaries of their usefulness. Presented with these new problems, materials were adapted to fulfil new purposes. Just like iron enabled us to perform new tasks until the tasks became ever more demanding and caused such wear on tools that the properties of pure iron needed to be adopted which, over the course of centuries, leaves us now with an enormous variety of steels that are tailored – through processing – to a myriad of different types for different applications.

What used to be learned over a long and costly period of time through trial-and-error is nowadays a highly focussed approach performed by scientist working at the frontier of invention. They then pass on those raw ideas and concepts to engineers that refine and adapt the novel materials and concepts and establish whether they can be useful on a large scale.

Consequently a new material becomes truly useful when every aspect of it can be tailored, from properties, such as particle size, hardness or colour to shaping and patterning of the final product. Today there is a whole plethora of morphology controlling techniques that have been refined over the years for their respective materials and target applications. Some materials need special structuring techniques due to their unique properties – just like diamonds cannot be cut with the proverbial butter knife one cannot simply use any technique to work with liquid precursors. Out of the multitude of approaches ink-jet printing has emerged as one of the most promising methods for processing liquid materials. It has especially been deemed the most capable way of manufacturing single unit and on-demand prototypes in the field

of future electronics.[1] It is not only highly refined (regular printers can easily dose ink drops in the 1 pL range, with newly developed printer heads reaching as low as some ten aL[2]), but also extremely inexpensive (simple ink-jet printers cost roughly 25 €). Even more importantly ink-jet printing is a technique that is very easy to use and that can be controlled finely without any specialised equipment.

Another well documented principle of exerting structural control over a material is the concept of biotemplating. Through evolution, nature has produced magnificent structures of unprecedented complexity and perfection. Even with modern manufacturing techniques man would struggle to produce intricate structures, the likes of which nature has created, with similar speed and in similar quantities. Subsequently a whole field revolves around employing them as templates, scaffolds or structure directing agents in general.[3]

Abiding by the idea of employing simple, inexpensive concepts to produce highly functional and advanced materials biotemplating, specifically the renewable resources cellulose or its predecessor wood, can be used as a means to control the morphology of desired products. Even though printing and paper intuitively belong together little has been done to combine the patterning powers of ink-jet printing with the biotemplating possibilities offered by cellulose. Doing so issues the challenge of transferring an established, well investigated technique to a new field. This challenge is, however, also a great opportunity and promises to pool the advantages of two highly regarded fields. Combining two pattering techniques, which each cover a different length scale, brings the enormous gain that the resulting structures are hierarchical. Even more so, since through this every stage of this hierarchy can be tailored fully independently of the others. The ability to harness all of the described advantages however hinges heavily on the understanding of every aspect of the underlying mechanics.

This work will concern itself with precisely this challenge and derive a way of combining ink-jet printing with biotemplating to produce novel and highly functional composite materials. Furthermore, the arising issues of grasping the concepts that govern each of the processes steps and the possibilities of performing this work in an environmentally sound way will be addressed.

Consequently the current chapter will be followed by a brief introduction into the fundamentals of nanoparticle and graphite synthesis, as well as shaping and patterning techniques. After this, *chapter III* will deliver a conclusive and well documented picture of the mechanism governing the graphitisation of carbons with the help of an iron salt solution. This is followed by a chapter expanding the presented concepts to ternary transition metal carbides. From this *chapter V* will present the synthesis of various well defined elemental metal and metal alloy nanoparticles

dispersed in a carbon framework. These synthesis chapters are succeeded by a chapter covering all the results obtained from the patterning techniques employed – most notably, but not exclusively, the results obtained from ink-jet printing of the precursors. The last chapter presents results regarding alternative synthesis methods, which effectively detach presented synthesis procedure from high-end equipment, such as inert atmosphere furnaces, and any source of electricity.

II. FUNDAMENTALS

NANOPARTICLES

In the widest sense any object, which is at least in one dimension less than 1 µm long can be considered a nanostructure.[4] However, particles being of 100 nm or less in at least two dimensions are more commonly referred to as nanoparticles.[4-5]

Nanoparticles have, albeit unknowingly, been used by mankind for thousands of years. The most renowned example for this is the use of dichroic ruby glass by the romans dating back to the year 300. The effect that a glass has a different colour depending on whether light is reflected from it or transmitted through it stems from gold nanoparticles of less than 60 nm embedded in the glass.[6] Nowadays nanostructures pervade virtually every aspect of our lives from microprocessors to cosmetics and from paints to medicine.

The reason why nanostructures are of such high interest is that they are the transition between single atoms or molecules and bulk materials. Where the physical and chemical properties of a bulk material are considered to be invariant with size, they are not with nanoparticulate systems. This is called the "size effect" and denotes the observation that with decreasing dimensions even basic physical properties such as melting point, magnetic properties and dielectric constant may change. A good example of this is the melting point depression in gold nanoparticles: bulk material gold melts at 1336 K and 2.5 nm gold particles at approximately 570 K, a drop of about 750 K.[7] Those changes are due to the increasing fraction of surface atoms. In contrast to bulk atoms, which are just surrounded by other bulk atoms and hence "see" a constant environment surfaces atoms are subject to asymmetric interactions as they are on one side in contact with the surrounding medium. This also means that the property changes are not abrupt but rather smooth transitions and can thus be controlled *via* the particle size. This, along with the emergence of entirely new properties, is the actual core reason behind the enormous interest in nanostructures. The multitude of observed effects and the underlying physical concepts have been the focus of decades of research culminating in tens of thousands of publications, from peer-reviewed journal articles over books to full encyclopaedias, covering virtually every aspect of the fundamental concepts.[4-5, 8]

Nanostructures are produced by one of two possible approaches, depending on whether the starting material is larger (i.e. bulk) or smaller (i.e. single atoms or molecules) than the desired nanoparticles. The first is fittingly termed the top-down approach, whereas the latter is called bottom-up approach. Typical top-down methods are volatilisation and re-condensation, milling and several lithography methods.

Bottom-up approaches include sol-gel syntheses, pyrolysis, various vapour phase condensation techniques and solvothermal reactions. Reducing the size of a material from bulk dimensions down to nanometre sizes is usually possible on the industrial scale – like the manufacturing of microprocessors, but comes either at very high monetary cost or lacks severely in size and shape control. The *de novo* synthesis from atomic or molecular starting materials is often less expensive and provides significantly better control over size and size distribution of the obtained nanostructures, but scaling to industrial quantities is in many cases very difficult or near impossible.

The size distribution of nanostructures is one of crucial factors, due to most of the properties depending strongly on the size of the particles. This is especially true in the size regime below 10 nm where the size dependence is most pronounced. For example the melting points of gold nanoparticles of 5 nm and 10 nm differ by approximately 130 K which means that even well-defined gold nanoparticles with a size of (6 ± 0.5) nm have a melting region of (1138.5 ±18.5) K.[7] The class of methods most commonly used to produce nanoparticles of narrow size distribution are solution based bottom-up approaches.[9-11] Even though they typically lack the scalability, they are, in terms of particle size and shape control, considered superior to high temperature synthesis approaches.[12] Consequently a method that can connect scalability with exceptional size control is highly sought after.

Lastly it is noteworthy that, mostly independent of the synthesis approach employed, nanoparticles follow a log-normal size distribution.[11, 13] The reasons for which have been subject of intense debate and are not fully understood. *Kiss* et. al. have derived a physically reasonable model that is based upon drift and diffusion in and out of a growth zone, but this model can only loosely be applied to syntheses in a liquid phase.[13]

CARBIDES

Metal carbides are a vast class of materials that are on the border between regular metals and ceramics. They possess properties of either class of materials, such as conductivity and catalytic activity commonly found among metals but also exceptional mechanical properties as well as high resistance to wear and chemical corrosion that are more associated with ceramics.[14-15] This combination of properties stems in the structure of the carbides; while they typically still possess the crystal structure of the pure metal, giving them metallic properties, they also have some or all of the interstitial voids filled with carbon atoms which results in the metal planes being fixed in their relative positions. The latter thus causes the compounds to be very stiff and extremely hard structures.

A model example of this is tungsten carbide, which is not only one of the hardest substances known, but was also the first non-noble metal compound reported to catalyse the oxygen reduction reaction (ORR), one of the half-cell reaction taking place in fuel cells.[16] Other important examples include titanium carbide and silicon carbide which possess similar hardness and very high resistance to chemical corrosion. Examples for good catalysts are iron carbide and iron nitride, the former being involved in the *Fischer-Tropsch* syntheses and the latter in the *Haber-Bosch* process, both of which are large scale industrial processes.[17-18]

More recently the focus is also shifting towards the catalytic properties of ternary carbides,[19] a field that has for a long time only been under investigation by the steel industry for the impact that carbide inclusions have on the properties of steels.[20]

Metal carbides are typically made by one of two general synthesis pathways. Either a deposition method such as physical vapour deposition (PVD) is used. This yields typically pure and well defined systems, but is a very costly method and only applicable to a limited number of systems, furthermore usually just the most stable polymorph is available *via* this method. The other path uses chemical synthesis approaches such as thermal decomposition or ammonolysis that often involve very high temperatures in excess of 1000 °C. The latter however lacks greatly in terms of control over morphology. In recent years advances in other chemical methods like sol-gel processes have allowed for the production of a wide variety of carbides and other interstitial alloys under more moderate conditions with better morphological control.[15] Size distributions are nevertheless not yet comparable to the well-established liquid phase synthesis techniques employed for the laboratory scale production of many elemental metal and metal oxides nanoparticles.

GRAPHITISATION

Graphitisation is the process of ordering amorphous carbon materials into mostly or fully aromatic, high C-content compounds, such as graphite, hence the name. Graphitisation commonly only refers to top-down processes in such a way that the graphite is obtained by converting bulk non-graphite carbons or carbon containing materials into graphitic carbon. The bottom-up approaches that prepare graphite *via* condensation of small molecules is not included in the typical meaning. Graphitisation can either be performed *via* a pure high temperature treatment or with the help of other substances. In the former case carbon materials are commonly divided into two classes: graphitisable and non-graphitisable materials.[21] The graphitisable materials can be converted into graphitic structures at temperatures below about 3000 °C (i.e. about the melting/sublimation point of carbon[22]) in some cases as low as 800 °C.

These processes usually take very long heating times of up to several days or even weeks.[23] Non-graphitisable materials will gain some degree of order but will not fully convert to graphite until a significant fraction of the inner molecular bonds and cross-links are broken due to extremely high temperatures.[21, 23-24] The reason for this is that graphitisation happens *via* a liquid-like phase that contains growing islands of graphite, which do not possess the necessary freedom of movement in order to grow and align if the degree of crosslinking in the material is too high. A typical example of such a material is cellulose, but it is also true for many other highly cross-linked carbon materials.[21]

Graphitisation processes that involve other substances can again be divided into two large classes. One is based upon the chemical or physical disintegration of carbon containing compounds, such as carbides. This process is more commonly used to produce porous carbons that may well be amorphous,[25] it can however also be used to produce high quality graphitic structures.[26] For this a carbide, often silicon carbide or titanium silicon carbide, is either thermally or chemically, with reactive gasses such as chlorine, decomposed to form some volatile species and pure carbon. Due to the structure of carbides the carbon atoms are often single carbon atoms in interstitial voids; when they get released they can bind together in the most stable form: graphite. The so obtained carbon structures, independent of their internal order, are hence named carbide derived carbons (CDC).

The other large process used to produce graphitic carbons form amorphous carbon stock is catalytic graphitisation. Some twenty-five metals, foremost the d-block metals iron, nickel and cobalt, have the ability to catalyse the process of graphitisation.[27-28] This, in close relation to the CDCs, progresses for some of the less effective metals first *via* the formation of stable carbides, which then later are decomposed again to form the graphitic carbons.[27] The more effective metals form a liquid carbon-metal eutectic which then precipitates ordered carbons while dissolving amorphous carbon.[24, 27-30] Here it is important to note that depending on the feeding speed and the size ratio of carbon precursor to catalytic metals either graphitic carbons,[27] carbon nanotubes[29, 31] or graphene flakes[26] are formed.

PATTERNING TECHNIQUES

Structuring and patterning techniques are an enormous field, not only in science, but even more so in industry. Lithography methods for example are undoubtedly the foundation of modern information technology.

Despite their close relation, the terms structuring and patterning commonly refer to two slightly different alterations of a material. Patterning most often means that parts or areas of a formerly uniform substrate are altered in some way, without

actually influencing the shape of the material. Common examples of this would be printing or the dyeing, where the shape of the paper or cloth is not altered and yet the material is divided into parts with different properties, such as colour or conductivity. Structuring, in contrast, typically involves noticeable changes to the actual shape of a material, in some cases without actually altering anything about the composition of a material. Everyday examples of this would be wood carving or paper folding, but also machine based techniques such as CNC milling[32-33] or the more recently developed rapid prototyping techniques,[34] both of which can work with (sub-)µm accuracy.[34-35] After the processing the substrate is still uniform in composition, yet its shape is changed immensely. Structuring however may also include techniques that alter the composition of a material such as etching or selective dissolution. The borders between the two types of alteration are nevertheless somewhat blurry. Ion implantation for example can be regarded as a patterning technique but may well be accompanied by structural changes as well. There is no fixed definition of the two terms and often something referred to as structuring will encompass changes that strictly seen should be regarded as patterning.

The only machine based patterning technique that is of great importance for this thesis is ink-jet printing, consequently only this technique will receive a more in-depth review here and in the beginning of the corresponding chapter "VI. Structuring and Patterning". Ink-jet printing has been employed, due to its versatility and ease of use, in many aspects of materials science. Specifically the printing of chemical objects has spurred key advances in several fields, including works in colloid science and bio-pharmacy[36-37] or *via* intermediate sol-gel chemistry in the construction of micro structured functional materials,[38] as well as in the manufacture of functional coatings.[39] This approach has furthermore already encompassed a wide variety of materials and properties.[40-42]

In the work at hand ink-jet printing will, among other things, be used to produce carbon in carbon conductors. Although some work has been done in the field of carbon conductors,[43] it relied thus far on dispersing and printing of pre-formed carbon structures rather than an *in-situ* process. To date, these processes are often difficult to scale up and, most importantly, they almost exclusively use thermally unstable precursors (usually the printing substrate or support). This has hampered integration of printing techniques with well-established high temperature processing techniques; a key requirement for future electronics. These challenges are overcome, without sacrificing simplicity, by using a paper support and catalytic ink as two reactants to generate functional carbon/ceramic arrays and 3D structures. This simple 'beyond the lab' process with off-the-shelf equipment is suitable for large scale and high temperature production of materials with electrode or catalytic applications.

III. Catalytic Graphitisation

Introduction

The understanding of a system is crucial for one's ability to alter its properties in a targeted way; consequently, the understanding of the model system iron / cellulose is the first focus point of this thesis. The knowledge gained here will be the foundation of all further chapters; it will illuminate the processes that bring about the formation of iron carbide as well as the mechanism of catalytic graphitisation facilitated by the presence of iron moieties.

With the emergence of *in-situ* imaging of nanometre sized systems, foremost *in-situ* TEM, a great many studies regarding the catalytic formation of a wide array of carbon structures, most of them concerning the growth of carbon nanotubes, have emerged.[29-31] The vast majority of the studies however rely on very controlled systems, e.g. they employ finely metered gaseous carbon sources, very well defined, prefabricated catalytic nanoparticles, *et cetera*. This is, when studying contributions of a singular component to a multicomponent system, absolutely essential, but applicability to "real-life-systems" may well be limited. Therefore the first concern was to ensure that different grades of cellulose – including raw wood – underwent the similar processes when calcined together with iron moieties. This is especially needed since here the carbon source and the iron precursors are on entirely different length scales, being several magnitudes apart in size. Initially it was planned to look at the formation of iron carbide separately from the process of catalytic graphitisation, but it soon became evident that the two processes are intertwined so closely that one must consider both at the same time. Therefore this chapter will be divided into the separate analysis techniques employed to shine light on the underlying chemistry, rather than the separate processes observed.

Synthesis and Analysis

The syntheses presented in this chapter are performed with one of two cellulose precursors, either lab-grade cellulose filter paper (CFP) is used to obtain large monolithic samples or microcrystalline cellulose (MMC) is used to obtain powdered samples. Other cellulose and cellulosic biomass precursors have been employed as well. Since this chapter is to deal with the exploration of the catalytic mechanism, the use of non-standard cellulose source will be described in a later chapter (see "VII. Green Synthesis and Applications"). The metal is provided by adding aqueous solutions of an iron salt. Several iron salts, namely iron(II) acetate, iron(II) acetylacetonate and iron(III) nitrate nonahydrate, have been probed for the syntheses, all of which proved to result in the same products. In the case of MCC 2.54 g of the cellulose are mixed

with 5 mL of 0.57 M iron salt solution. The cellulose to solution ratio was determined empirically by probing for the amount of cellulose needed to fully soak up 5 mL of water. For the filter paper based samples the paper is submersed in the same solution and then laid out twice on dry petri dishes to remove excess liquid. The received mixture is put directly into lidded crucibles and calcined in a chamber furnace under inert atmosphere (typically pure nitrogen). The calcination procedure involves purging the reaction chamber for 30 minutes with nitrogen and subsequent heating to the reaction temperature (800 °C unless otherwise noted) with a ramp of 10 $K \cdot min^{-1}$.

The remainder of this chapter follows the analysis techniques employed. Firstly the morphology of the phase pure iron carbide / carbon products obtained under optimal synthesis conditions is described, which then bridges over to temperature dependent analyses performed to explore the graphitic graphitisation. The chapter is concluded by the presentation of the mechanisms governing this system.

The iron carbide - carbon composite produced *via* the above described procedure is of black colour and highly magnetic. The general morphology resembles, save for the obvious change in colour, that of the employed cellulose template (**Figure 1**).

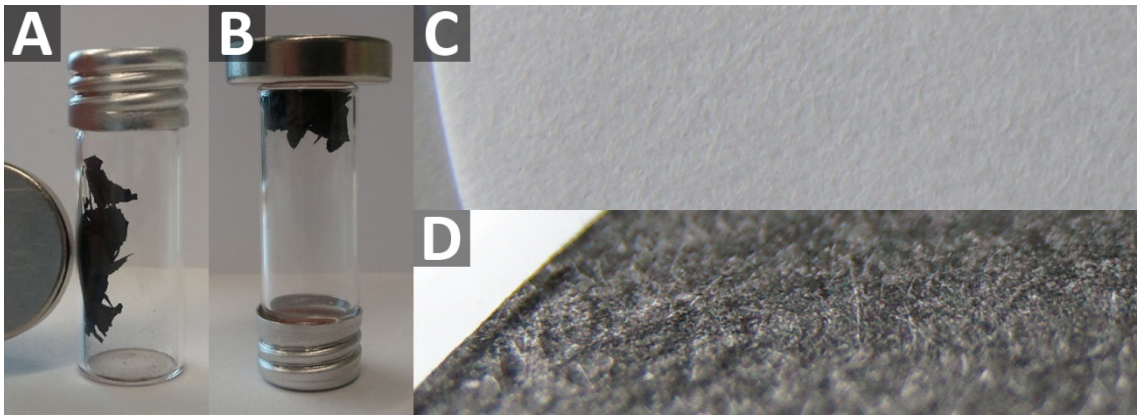

Figure 1: **A-B**: The resulting nano-composite is highly magnetic due to the embedded iron carbide nanoparticles. **C-D**: Visual assessment shows that the morphology is retained very well.

Using powdered cellulose results in a black or greyish shiny powder, using a filter paper results in a more brittle, paper-like product. The latter experiment makes it evident that the samples do undergo some shrinkage. The reasons for which will be discussed in the remainder of this chapter.

Scanning electron microscopy (SEM) was foremost employed to study the micrometre scale morphology of the carbon fibres. The analysis confirmed what visual assessment of the composite suggested already: the morphology of the employed CFP or MCC is retained exceptionally well. In fact it is retained so well that virtually no difference can be made out when comparing uncalcined cellulose fibres with fibres

that have been calcined in the presence of iron (**Figure 2**). On the centimetre scale however shrinkage to approximately 60 % of the initial dimensions and a colour change from white to black is evident.

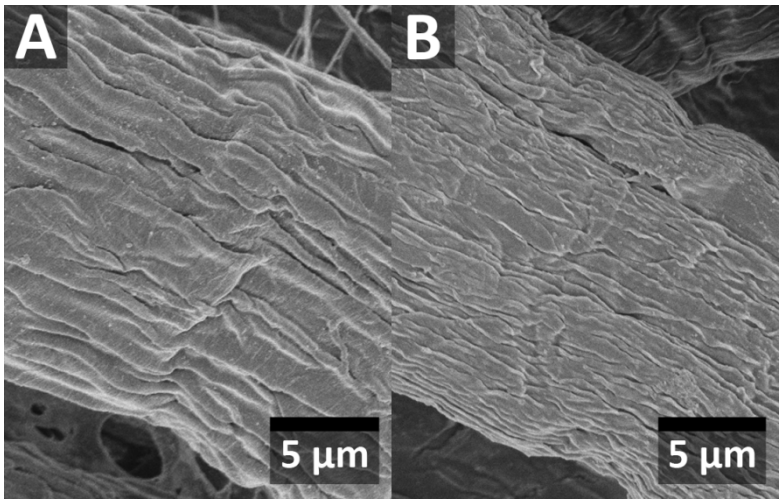

Figure 2: **A**: SEM of an uncalcined sample. **B**: SEM of a calcined sample.

A comparison of samples before and after calcination shows clearly that the morphology of the cellulose fibres is retained very well on the micrometre scale. This raises the question down to which point this shape retention continues. Higher magnification SEM images of fractured surfaces depict this point (**Figure 3**).

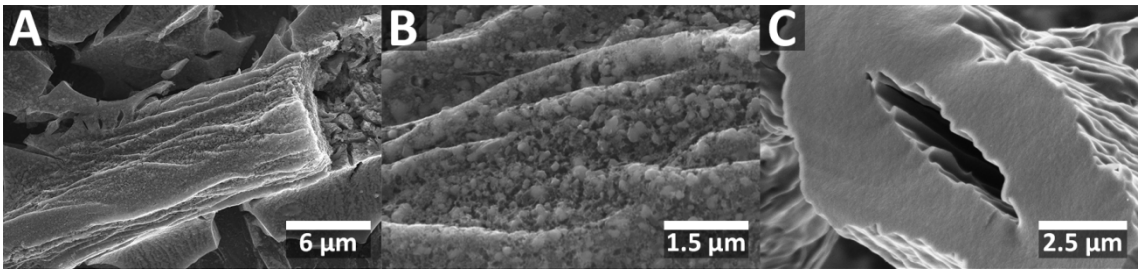

Figure 3: SEM micrographs. **A-B**: Highlighting the porous nature of the fibres after treatment. **C**: Cross-sections of fibres that have been calcined without any iron appear completely different.

These close-up images reveal the porous nature of the surface and the inner parts of the fibres – a feature that is not present in cellulose calcined without any iron.

However, regular SEM was only able to properly depict the general presence of porosity, but a limited resolution made further structural evaluation difficult. The logical choice was then to work with high resolution SEM (HR SEM) which simultaneously adds the benefit of having a good element contrast which, in brief, is due to the position of the detectors relative to the sample and the signal processing.

HR SEM clearly reveals the porous nature of the fibres (**Figure 4**) and in many micrographs shows a peculiar phenomenon: the iron carbide nanoparticles frequently

reshape to precisely follow the surface structure of the cellulose template (esp. **Figure 4 A**) where they remodel even small wrinkles on the fibres surfaces.

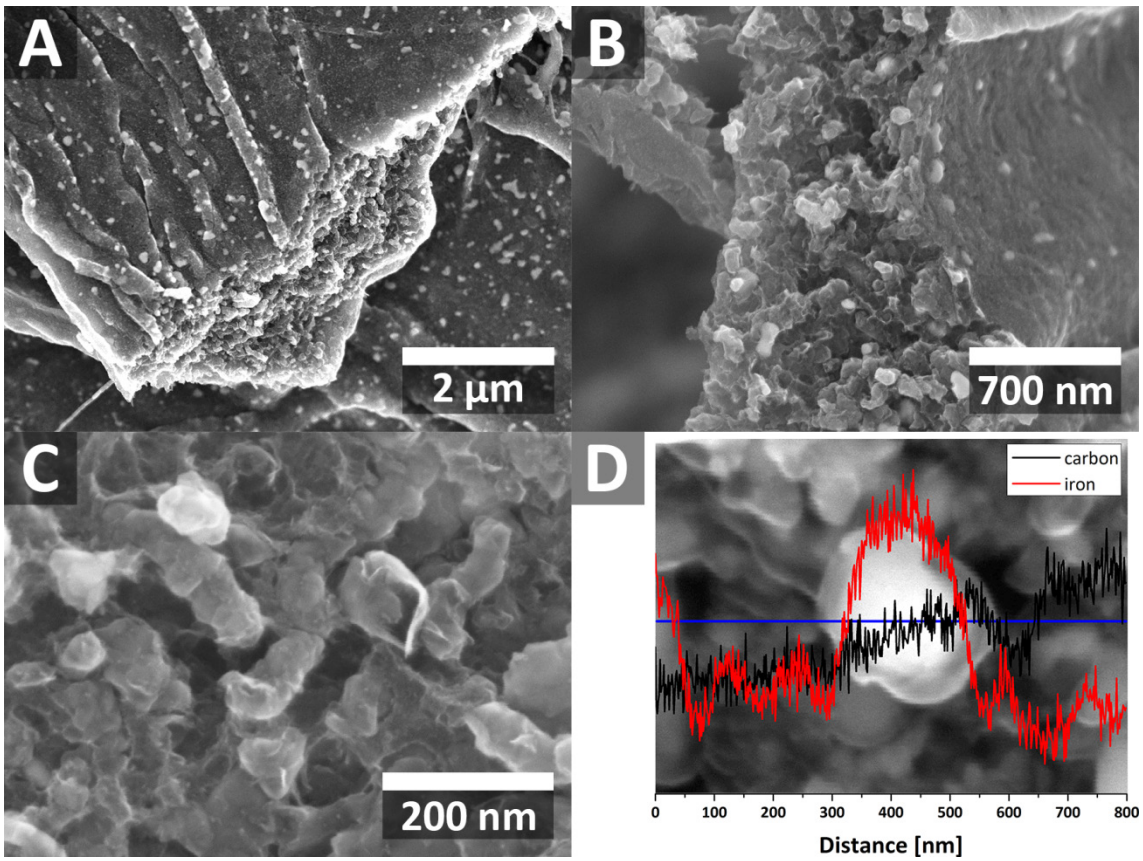

Figure 4: **A**: Note the iron carbide nano-particles that have reshaped to the surface wrinkles of the fibres. **B**: Zoomed out view showing the cross-section of a cellulose fibre, the porosity of the nano-composite and the fact that the whole fibre consists of graphitised carbon **C**: This is a SEM micrograph of ripped carbon-tubes showing that they are hollow and have very thin walls. **D**: Line EDX (for iron and carbon, along the turquois line) performed across a single particle.

Lastly this study confirms that the former cellulose fibres become porous throughout and that the iron carbide nanoparticles are evenly distributed within the composite.

To quantify the porosity, which is observed to result from the interplay of iron with cellulose, nitrogen sorption measurements were performed. Furthermore two reference isotherms were obtained to ensure that any effects found were caused by the iron moieties and their reactions with the carbon (**Figure 5**).

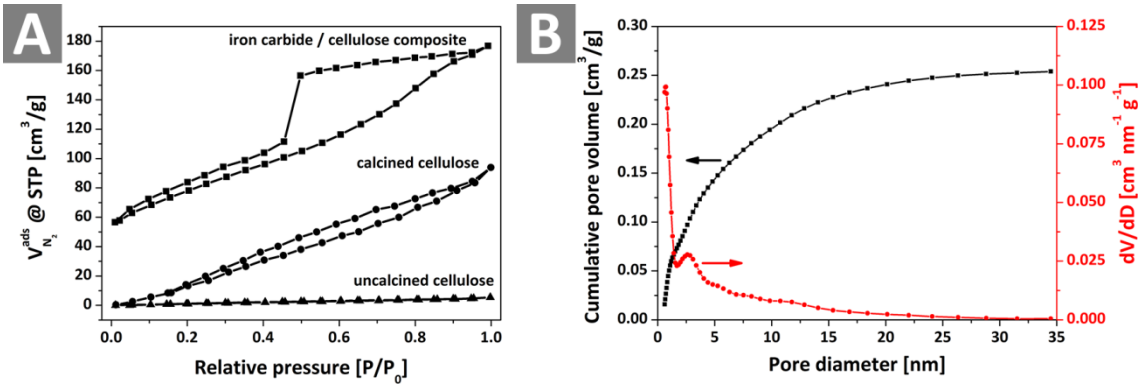

Figure 5: **A**: Nitrogen sorption isotherms of uncalcined cellulose, cellulose calcined without an iron salt and of the nano-composite. **B**: The corresponding pore size distribution (QSDFT model, adsorption branch) for the nano-composite.

Nitrogen sorption clearly shows that only the combination of cellulose with the aqueous iron salt solution yields in a highly porous material upon calcination. The specific surface area and the pore size distribution was evaluated with a quenched solid density functional theory (QSDFT) model[44-45] (**Table 1**). The QSDFT model was applied to the adsorption branch of the isotherm, since the pronounced hysteresis, with the sudden drop in the desorption branch, suggested that desorption happens *via* cavitation and consequently made this branch of the isotherm useless for pore size evaluation.[46-47] The resulting isotherm was a type IV isotherm and the pore size distribution showed a population of micropores as well as a broad distribution of mesopores (**Figure 5**). The specific apparent BET surface area ($SA_{BET, app.}$) was calculated to be 273 $m^2 \cdot g^{-1}$, which is significantly larger than the value for the uncalcined cellulose (4 $m^2 \cdot g^{-1}$) and also larger than the surface of the amorphous carbon gained from carbonising cellulose without any iron (62 $m^2 \cdot g^{-1}$).

Table 1: Summary of the nitrogen sorption results.

Sample	$SA_{BET, app.}$ [1] [m^2/g]	Cumulative surface area [2] [m^2/g]	Cumulative pore volume [2] [cm^3/g]
Raw coffee filter	4	4	0.007
Calcined filter	-- [3]	62	0.125
Fe_3C composite	273	264	0.255

[1]BET method. [2]Taken from the QSDFT calculations. [3]Due to the lack of porosity the BET model gave no reasonable values

In conclusion there is a significant improvement in both surface area and porosity. This is promising for possible applicability in catalysis and other fields that profit by having high surface area materials and thus demands a deeper look into the underlying mechanism.

X-ray diffractometry was primarily performed in order to address two points. One was to assess the product formation of cellulose at high temperatures with and without the iron moiety present (**Figure 6 A**). The other was to determine the phase-

changes, in dependence of the temperature, which are caused by the interplay of iron and cellulose (**Figure 6 B**). For the latter samples were prepared, calcined and cooled down from various temperatures in order to obtain a full temperature profile of the reaction.

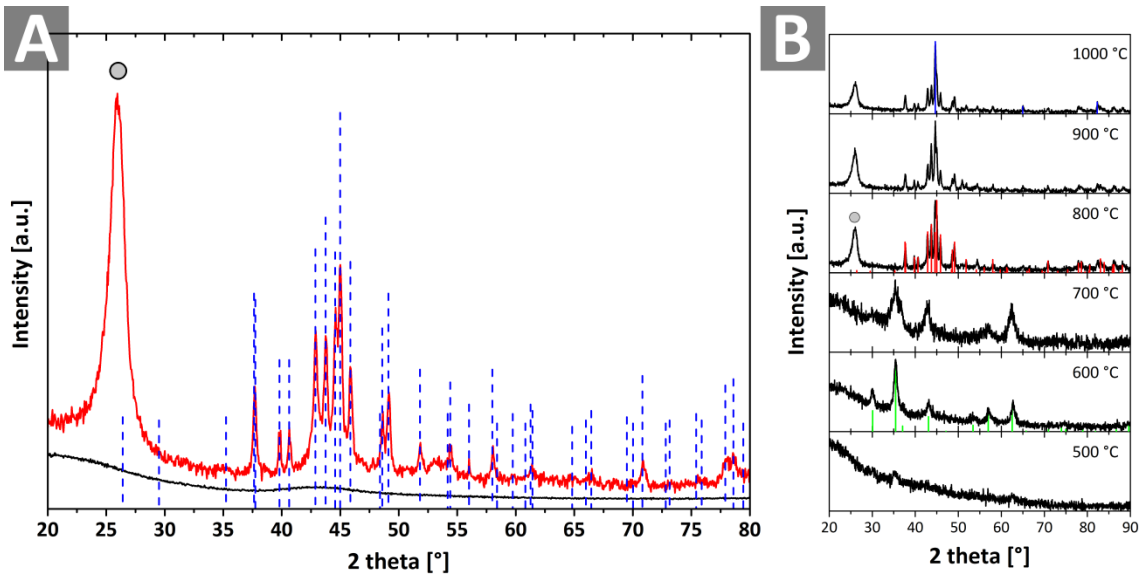

Figure 6: **A**: Comparison of the nano-composite (red) and cellulose calcined without any metal (black); the grey dot denotes the peak attributed to graphite (ICDD 04-015-2407) the blue lines represent a Fe_3C reference pattern (ICDD 00-035-0772). **B**: XRD patterns of samples quenched at 100 K intervals. The inserted reference patterns correspond to: Green: Fe_3O_4 (ICDD 01-077-1545), Red: Fe_3C (ICDD 00-035-0772), Blue: Fe^0 (ICDD 04-007-9453) and the grey circle at 26° 2 theta is attributed to graphitic carbon (ICDD 04-015-2407). A larger print of B can be found in the appendix.

Comparing samples with and without iron shows that the presence of iron is needed to graphitise cellulose at 800 °C and above, which was expected since cellulose is considered to be a non-graphitisable carbon.[21] The temperature dependent XRD patterns furthermore reveal two interesting results. One is that the only crystalline phase this system passes through is magnetite, iron(II,III) oxide, which starts to crystallize at about 500 °C. This is then directly converted to iron carbide, forming at 800 °C. Furthermore can be seen that the decomposition of said carbide to elemental iron sets in between 800 °C and 900 °C and progresses further at 1000 °C.

XRD not only yields characteristic diffractograms which can be used to identify phases, it can also be employed, to a limited extend, to judge particle sizes as well as defects in the crystalline lattice.[48] The crystallite size can be derived, in a first approximation, from the peak position θ (not the typically used 2θ) and breadth (full width at half maximum) B; both in radians, *via* the *Scherrer* equation[49]

$$d = \frac{K\lambda}{B\cos\theta}$$

with

$$K = 2\sqrt{\frac{\ln 2}{\pi}} \approx 0.94$$

where λ is the wavelength of the X-ray radiation and d is the diameter of the crystallites in the same units as the wavelength. Further information such as strain and compositional variations could not reliably be derived from XRD patterns due to large scattering of the corresponding data.

Deriving crystallite sizes gives rise to the other interesting point, which is that the crystallinity or the size of the iron oxide nano-particles is noticeably reduced when going from 600 °C to 700 °C, as can be seen from the severe broadening of the XRD reflexes. This broadening was observed several times with different specimens, which ensures that this behaviour not merely an experimental artefact. The observed effect is due to the onset of carbothermal reduction of the iron oxide, as the upcoming analyses will show. This makes it likely that the reflex broadening is, at least to a non-negligible part, caused by compositional – and thus defect – changes rather than just simple changes in crystallite size. Very small, systematic alterations in the peak positions further support this. The patterns obtained from samples prepared at 700 °C are better described by a $Fe_{2.929}O_4$ reference pattern.

Lastly the fact that the only oxide observed is Fe_3O_4, despite the use of Fe^{2+} and Fe^{3+} precursors, deserves some attention. At the temperature where the first crystalline phases are observed, magnetite is the most stable iron oxide.[30] If any other oxides are formed first (FeO or Fe_2O_3 depending on the valance of the precursor ions) they are converted quickly to magnetite, since no trace of other oxides was found. Another possibility is that the Fe^{2+}/Fe^{3+} ratio is reached before hand, because even though the atmosphere is inert, the counter ions and most notably the cellulose locally provide sufficient oxygen to oxidise Fe^{2+} and also possess the reductive power to reduce Fe^{3+} to Fe^{2+}. Hence this could be an alternative reaction path to the equilibrium oxide.

Raman spectroscopy is the standard technique for the analysis of carbonaceous compounds and a large number of studies have concerned themselves with the Raman spectra of diverse carbon structures.[50]

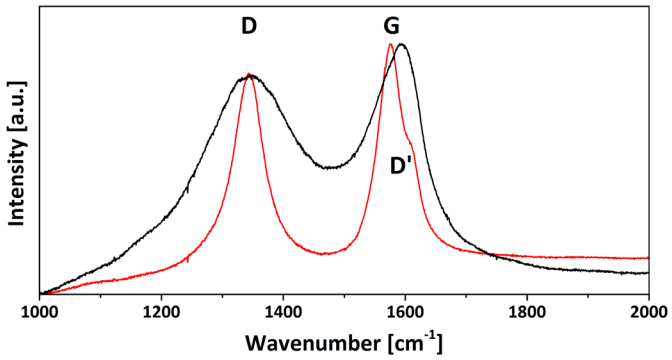

Figure 7: Raman spectrum of cellulose calcined with iron (red) and without (black). The D-, G- and D'-bands are clearly visible in the graphitised specimen.

The Raman spectra (**Figure 7**) clearly show a large difference in the degree of order. For the samples calcined with iron the G band is very prominent and more intense than the D band. The D' band is only present as a shoulder peak of the G band and also the full widths at half maxima (FWHM) of the peaks are relatively small. All of those are strong indicators of graphitic carbon. In contrast samples calcined without any metal are model examples of disordered carbons with very broad peaks and a unified G/D' band that almost has no trace of the former G peak.[51-53]

Regular transmission electron microscopy (TEM) studies were performed on ultra-microtome (UM) cuts of samples embedded in an epoxy resin. The reason cuts of the samples were used was that cellulose fibres have a cross-section of several micrometers, which is far too thick to be investigated in a TEM.

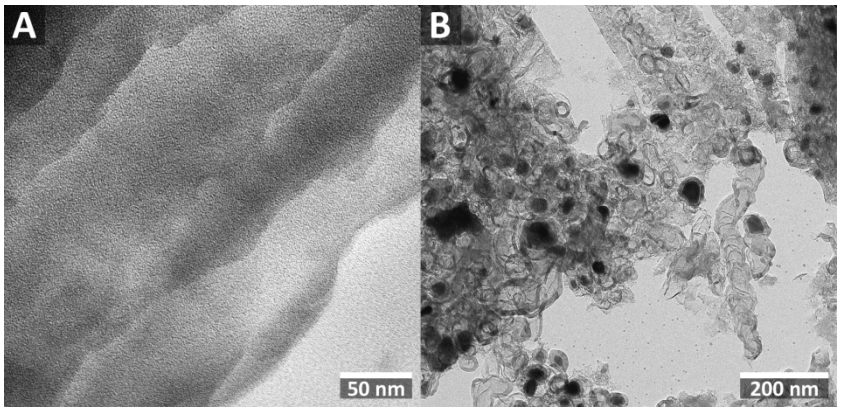

Figure 8: **A**: TEM (UM cut) of a cellulose sample calcined in the absence of any metal. The diagonal lines are due to the cutting and are not a feature of the sample. **B**: Cellulose calcined with added iron salt yields structures that are vastly different to the amorphous carbon obtained from cellulose alone.

Already the comparison of samples with and without iron shows a stark change in morphology. Where cellulose alone merely forms homogeneous amorphous carbons (**Figure 8 A**), the iron etches micrometre long tubular carbons, which run through the entire fibre (**Figure 8 B**), and lace the whole structure with iron carbide nanoparticles.

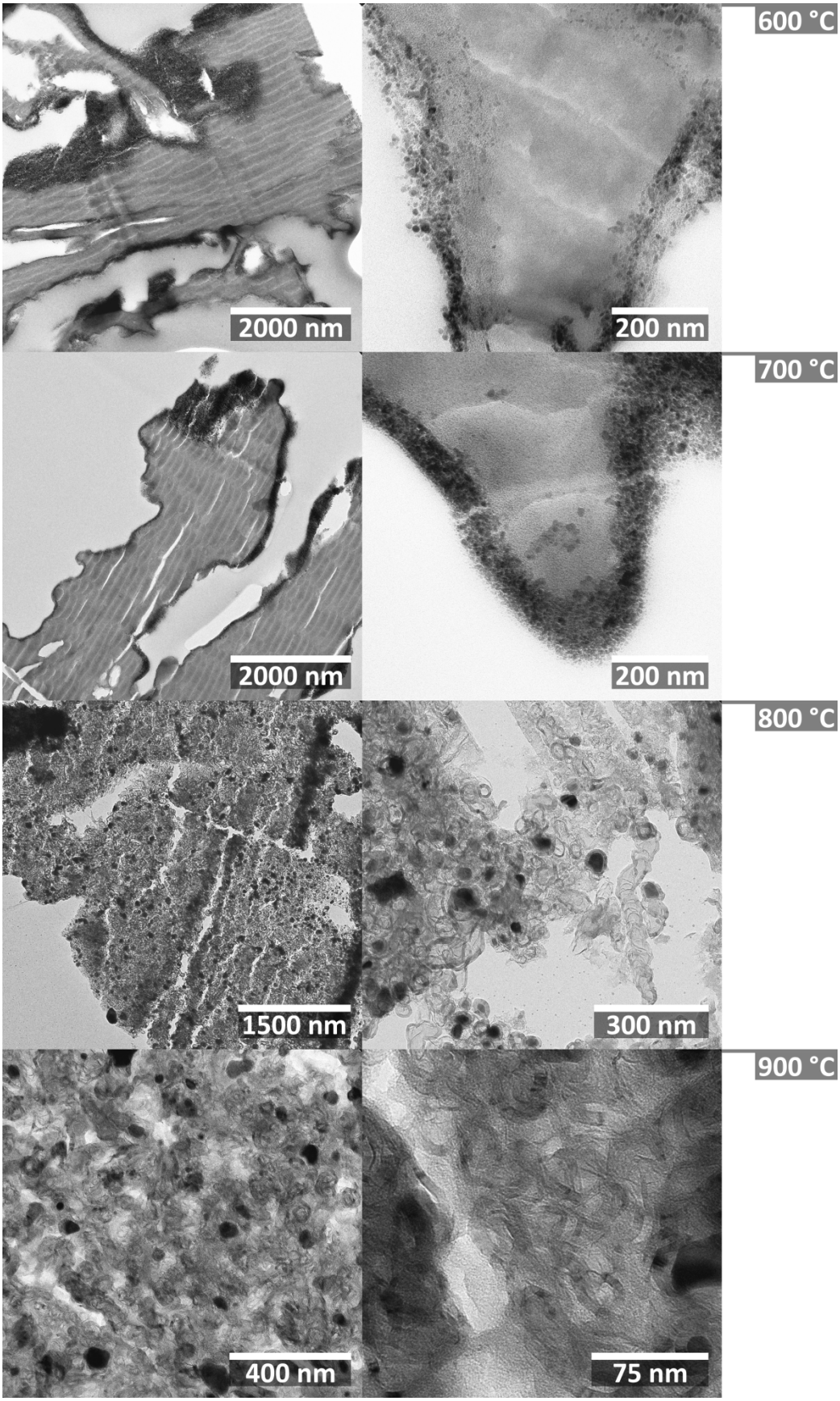

Figure 9: TEM micrographs of UM samples, which were quenched at various temperatures.

Ultramicrotomes of samples prepared at 100 K intervals – analogous to the XRD analyses – have been examined with the help of TEM to further investigate the mechanism that brings about these interesting structures (**Figure 9**). The TEM investigation of quenched samples depicts what the other analysis techniques have shown thus far. The reaction starts off at 500 °C with very small (approximately 5 nm) iron oxide nanoparticles. To this it moreover adds the valuable information that the initially formed Fe_3O_4 particles only reside on the surface of the fibres. It has to be noted though that, based on the available data, it cannot be ruled out that a small fraction of the iron fully enters the fibres. Upon close inspection some TEM micrographs show tiny dark spots within the carbon framework that may well be iron or iron oxide clusters.

These micrographs also shine light on the actual morphology of the graphitised carbons and show that the carbonaceous matrix consists of wrapped and wrinkled sheets, which form very long tubular structures with diameters ranging from 20 to 100 nm and an average wall thickness of 7 nm. The iron carbide nanoparticles themselves are of similar diameters (20 to 100 nm) and all have a shell of graphitised carbon which is of the same size or thicker than the observed tubular structures, i.e. 7 nm or thicker. The much larger size of the carbide compared to the iron oxide particles suggests that particle coalescence precedes the formation of the tubular carbons. If they were to graphitise the cellulose directly tubes of much smaller diameters would have to be present as well. Later analyses will show that once the tubes are formed they are not destroyed again by the catalytic processes. The presence of extended graphite networks is also underlined by resistivity measurements. These measurements resulted in an electrical conductivity of the samples that had undergone graphitisation, which is enhanced by a factor of 30 compared to the otherwise formed amorphous carbon. Furthermore, there are many cementite particles with peculiar shapes that deviate far from the typical spherical or facetted character observed for nanoparticles. The reason for the curious shapes actually lies in the catalytic process responsible for formation of the graphitic as will be shown in the following sections.

Further assessment of the nano-composite was done with the help of high resolution TEM (HR TEM) which is used, among other things, to image the lattice fringes of crystalline regions in a sample (**Figure 10**). As opposed to regular TEM, HR TEM relies on phase contrast imaging, rather than variations in exit wave intensity, the latter directly depicts electron density.

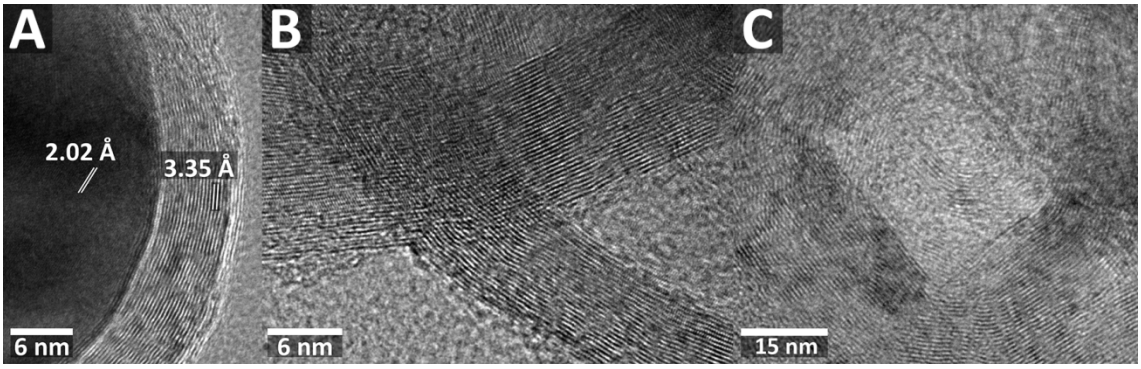

Figure 10: HR TEM images. **A**: Micrograph with labelled lattice fringes for iron carbide and graphite. **B**: free graphite highlighting the fact that not just carbon in close vicinity of the iron carbide is highly ordered. **C**: Sharp bends (here 90°) in the carbon layers confirm that these are in fact graphene layers and not simple tubular carbons.

HR TEM micrographs of samples prepared at 800 °C confirm the high degree of crystallinity of the iron carbide (a lattice spacing of 2.02 Å is attributed to the (031) plane according to ICDD 00-035-0772), as well as the carbon (the 3.35 Å corresponds to the (002) plane in graphite). Additionally sharp bends in the carbon lattices (e.g. 90°, **Figure 10 C**) confirm that the carbon is not of a tubular nature, but rather stacks of graphene layers; hence not carbon nanotube growth but, the actual formation of graphene from catalytic nanoparticles.

Thermo-gravimetric analysis (TGA) is a good technique to compliment the temperature dependent studies of quenched samples. Hereby the weight – or loss thereof – of a sample is monitored precisely during calcination. This allows drawing inferences about decomposition processes, which, for organic substances, typically happens under loss of volatile agents, such as carbon oxides.

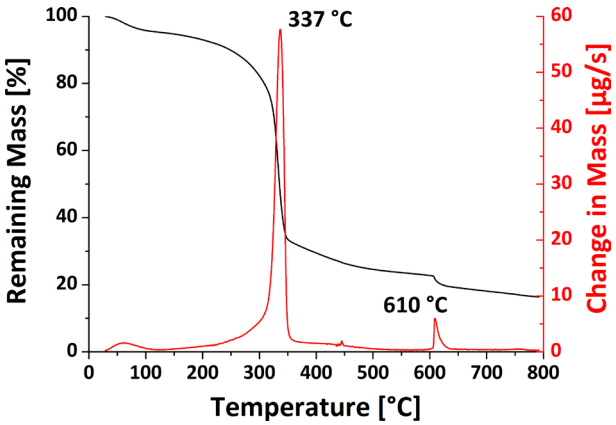

Figure 11: TGA shows that the cellulose matrix decomposes at about 340 °C and that the carbothermal reduction happens at about 610 °C.

TGA shows an initial weight loss of 5 wt% attributed to water remaining in the pre-dried sample, followed by the decomposition of cellulose with the main drop-off at 337 °C. Somewhat surprising is that the carbothermal reduction at 610 °C is visible as a

pronounced step in the TGA trace. This means that the reduction process is extremely fast, since it releases most of the CO_x within a few degrees Celsius. Taking into account the heating ramp of the TGA (10 $K \cdot min^{-1}$) the reduction is completed in about 2 minutes. Furthermore, this drop-off hints at the fact, that most of the CO_x is released in the form of CO. The step accounts for a mass loss of 3.32 wt%, which, corrected for the 5 wt% water content, equals a loss of 3.49 wt%. XRD had already shown that the iron, at this stage of the reaction, is present in the form of Fe_3O_4. If all of it were to decompose to form Fe^0 and CO_2 this would cause a mass loss of 2.77 wt%, whereas decomposition to CO would result in a mass loss of 3.53 wt%. This suggests that virtually all of the reduction happens *via* the release of carbon monoxide.

The most impressive proof of the mechanism proposed at the end of this chapter (see "Mechanism" section) is obtained from *in-situ* TEM between 700 and 800 °C, which allows the real time observation of the formation of the final product (video[54] and **Figure 12**). Here, liquid droplets of an iron-carbon eutectic with a size of 50 – 200 nm can be followed "eating up" the amorphous carbon, leaving a trail of crystallised graphitic carbon. This process is driven by the lower free energy of the perfected graphitic structures as compared to amorphous carbon. It is noteworthy that the melting point of pure iron is T_m = 1538 °C. This means that the melting point of iron is depressed by 900 K, which has been reported before but is astonishing none the less.[30] Reasons for this dramatic decrease in melting temperature are still subject to intense debate.[29] The most common causes for the melting temperature depression, such as nano-size effects[7] or local heating due to exothermic reactions[55] can be ruled out.[30-31] Similarly more refined conjectures, such as the catalyst not actually being liquid, but rather just appearing to be mobile due to solid-solid interactions above the Tammann temperature (approx. 0.3 - 0.5·T_{melt})[56] are not plausible causes. All of those do either not provide enough energy for the reaction or fail to explain the liquid state of particles with diameters of up to 500 nm.[29-30]

The video shows the liquid state of the eutectic better, but also stills taken from the graphitisation process display the high degree of mobility that the particles possess (**Figure 12**).

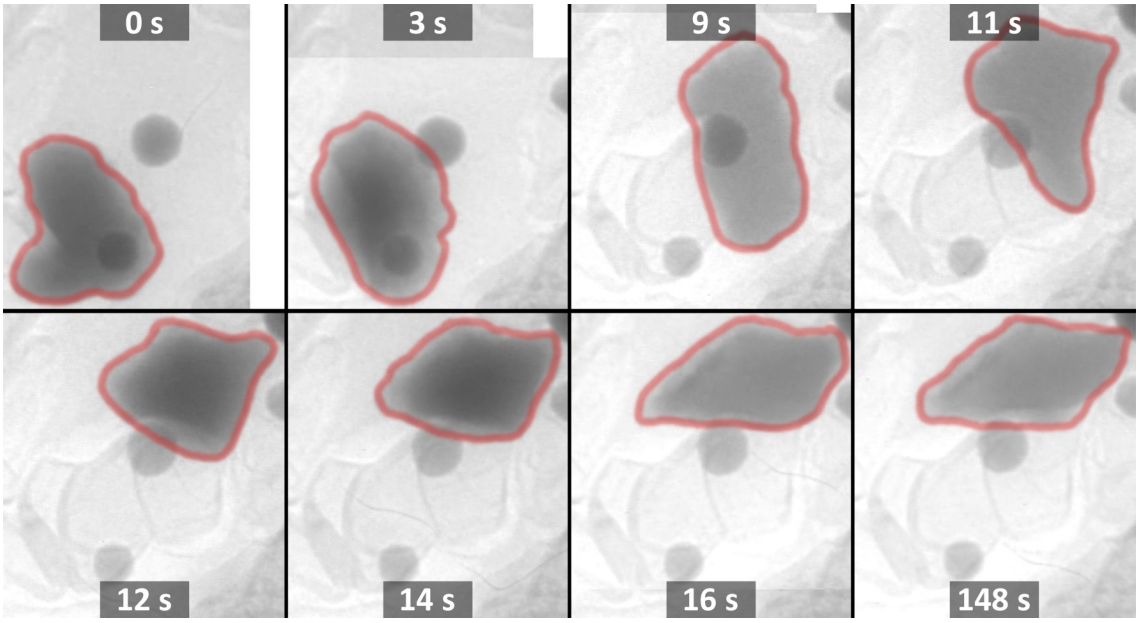

Figure 12: Stills taken from the *in-situ* TEM video depicting a particles movement on the carbon grid during graphitisation. Once the particle is surrounded by graphitised carbon it immediately ceases to move.

The fact that the iron(II,III) oxide phase is followed by a liquid super saturated iron-carbon solution and that the graphite layers a sequestered by said liquid eutectic concludes the analyses. The following section will summarize the catalytic graphitisation mechanism, which was distilled from all of the analyses.

MECHANISM

This whole mechanistic study of the system iron/carbon can be summarised in the following. First the iron salts are converted to form iron oxide, which then, at elevated temperatures exceeding 600 °C, is carbothermally reduced to metallic, iron containing nanoparticles, the exact composition of which is still subject of intense debate.[31] These then dissolve the amorphous carbon from cellulose and recrystallize it in the form of well-ordered graphene nanostructures. The fact that the reaction indeed runs *via* a liquid eutectic metal droplet (approximately 50:50 mixture of iron and carbon) is morphologically also seen from some of the final Fe_3C nanostructures. During crystallisation of the iron carbide, which occurs along with the cooling of the sample, several layers of ordered carbon are formed around the particles. These arise from the sequestration of surplus carbon from the eutectic in order to get from an iron to carbon atom ratio of approximately 1 to 1 in the eutectic to a ratio of 3 to 1 in the cementite. Lastly the aforementioned was compiled into a scheme (**Figure 13**).

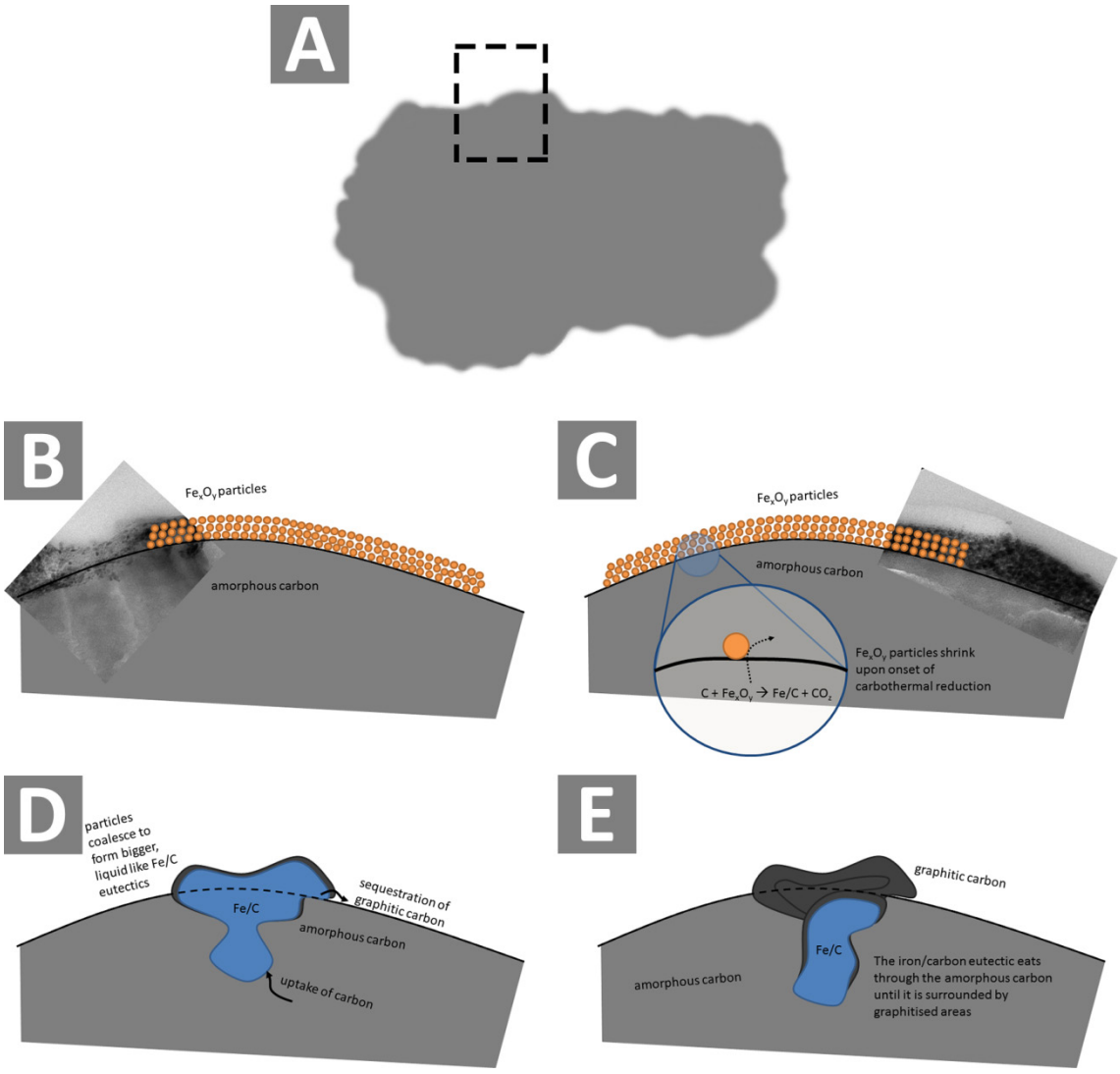

Figure 13: **A**: Cross section of the still amorphous carbon fibre. **B**: Close-up on marked area from panel A. The surface of the amorphous carbon fibre is covered in Fe_3O_4 nanoparticles. **C**: Onset of carbothermal reduction; Fe_3O_4 nanoparticles shrink in size as they are reduced by the carbon. **D**: An iron / carbon eutectic is formed that dissolved amorphous carbon and leaves a trail of graphitised carbon behind. **E**: The eutectic droplets keep dissolving amorphous carbon and sequestering graphitic carbon until they are surrounded by graphitic carbon or thermal fluctuation causes them to crystallise.

CONCLUSIONS

This chapter has provided an analysis of the iron carbide – graphitic carbon nano-composites utilising various techniques. Furthermore the processes governing the formation of the composite and the related catalytic graphitisation reactions have been investigated in depth.

Upon calcination under inert atmosphere the molecular iron precursors decompose and coalesce to 5 nm Fe_3O_4 nanoparticles, which then are carbothermally reduced to carbon monoxide and a liquid iron-carbon eutectic, which consumes the former cellulose. This consumption results in large porous networks of tubular carbons while the micrometre and larger morphology of the cellulose precursor is fully

retained. All of the observed reactions bear great similarities with studies in the literature that focussed only on a well-defined, small part of this.

Lastly this chapter has shown that even though the carbon source is provided in a less defined, bulk form and the iron moieties are formed *in-situ* rather than being well-defined preformed species, the reactions take similar paths as to what was described with highly defined systems in the literature. With this it laid a foundation for the understanding of processes shown in the following chapters.

IV. Ternary Carbides

Introduction

The synthesis of iron carbide has been studied in great depth before[15] and it has proven to be a versatile catalyst, most notably for the *Fischer-Tropsch*-process.[57-58] Similarly tungsten carbide was reported to be the first non-noble metal catalyst to catalyse the oxygen reduction reaction (ORR).[16, 59] Interestingly, even though the single metal carbides are materials of high significance, iron-containing ternary carbides (M_xFe_yC) have received little to no attention outside the steel/metallurgy community.[60] The reason why ternary carbides containing iron have not spurred more interest can only be speculated upon. This is more so the case when one considers that their combination could potentially lead to synergistic effects between the materials, causing unprecedented catalytic performance or even new catalytic properties. This chapter will demonstrate a very easy synthesis pathway to defined iron based ternary carbides, namely Fe_3W_3C, $W_2Fe_{21}C_6$ and $Fe_{2.25}Mn_{0.75}C$. Here for the first time these materials are produced in the form of nanoparticles, thereby broadening their prospected applicability. Previous work dealing with iron-tungsten-carbides looked into phase formation when alloying industrial steels and thus covered only the high temperature regime and it dealt with bulk metals – as is common in the steel industry – and not with the *de novo* formation of particles.[20, 61] As with tungsten, previous work encompassing iron, manganese and carbon was solely conducted by the steel and metallurgy community. Consequently this work as well had different objectives than the formation of phase-pure nanoparticles.

In this chapter the temperature dependent phase transitions undergone by the two systems tungsten-iron-carbon and manganese-iron-carbon will be investigated, similarly to the initial study of the pure Fe/C system.

Synthesis

All synthesis performed in this and the next chapter follow the same synthesis parameters that were derived from the previous chapter. Each multi-metal study probes three molar ratios, namely iron to metal ratios of 0:1, 1:1 and 3:1 in the temperature regime from 500 °C to 1000 °C. The heat treatment for the syntheses is in every case performed under inert atmosphere (nitrogen unless otherwise noted) with a 10 $K \cdot min^{-1}$ heating ramp to the denoted temperature, followed by the immediate shut-off of the chamber furnace. One of two cellulose precursors is used, either lab-grade cellulose filter paper (CFP) is used to obtain large monolithic samples or microcrystalline cellulose (MMC) is used to perform gram-scale syntheses and yields powdered samples. The iron precursor utilized in all of the experiments is iron(III)

nitrate unless otherwise noted. Ammonium metatungstate is the tungsten source, as the polyoxometalates of tungsten are the only salts that are soluble in pure water, and manganese(II) nitrate serves as manganese precursor.

The metal to cellulose ratio was taken from the syntheses described in the previous chapter. In brief 2.54 g of MCC are mixed with 5 mL of 0.57 M metal salt solution, where the molarity corresponds to the sum of the metal ions. For example a Fe:Mn 3:1 precursor is prepared by dissolving 869.6 mg of $Fe(NO_3)_3 \cdot 9\ H_2O$ (2.15 mmol) together with 180.1 mg of $Mn(NO_3)_2 \cdot 4\ H_2O$ (0.72 mmol) in 5 mL of deionised H_2O to form a 0.57 M solution. Similarly a Fe:W 0:1 precursor is prepared by dissolving 2.87 mmol of ammonium metatungstate in 5 mL of deionised water.

TUNGSTEN-IRON-SYSTEM

The system investigated in the work at hand yields a variety of phases and – within the conditions probed – usually several at the same time. For tungsten and cellulose alone XRD analysis can be used to follow the gradual reduction of the initially formed tungsten oxide, from tungsten(VI), *via* tungsten(IV) to elemental tungsten. With increasing temperature (**Figure 14**) each of the oxides is present in different crystal structures. The fact that this can be seen in XRD patterns of quenched samples shows well that the carbon matrix is even able to stabilise and maintain these intermediate stages when cooling the samples down to room temperature.

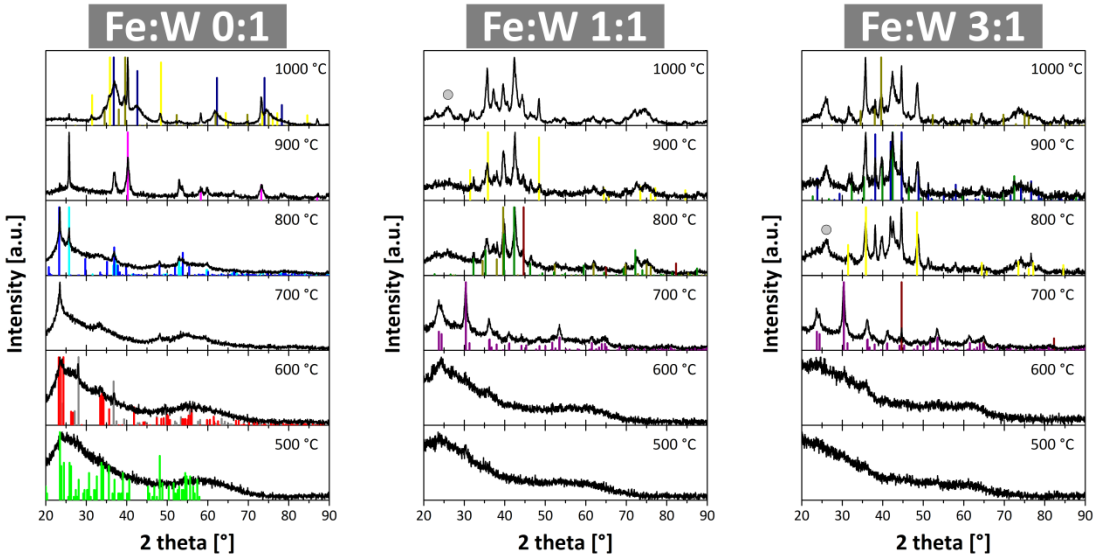

Figure 14: Summarised XRD patterns of the temperature and ratio dependent analysis of the tungsten-iron system. The reference patterns marked are: Green: $W_{18}O_{49}$ (ICDD 00-005-0392), Red: WO_3, triclinic (ICDD 01-073-6498), Grey: WO_3, hexagonal (ICDD 04-007-2322), Blue: WO_2, orthorhombic (ICDD 04-007-0872), Cyan: WO_2, monoclinic (ICDD 04-005-5105), Magenta: W^0 (ICDD 00-004-0806), Yellow: WC (ICDD 01-077-4389), Dark Yellow: W_2C (ICDD 04-014-5679), Navy: $W_2(C,O)$ (ICDD 00-022-0959), Purple: $FeWO_4$ (ICDD 04-007-5882), Wine: Fe^0 (ICDD 04-014-0360), Olive: Fe_3W_3C (ICDD 01-078-1990), Dark Cyan: $Fe_{0.94}W_{0.06}$ (ICDD 04-003-5513), Royal Blue: $W_2Fe_{21}C_6$ (ICDD 04-010-7445) and the grey circle at 26° 2 theta is attributed to graphitic carbon (ICDD 04-015-2407). Larger prints of the patterns can be found in the appendix.

When calcining the tungsten precursor and cellulose alone, initially polyoxotungstates ($W_{18}O_{49}$) are still present, but they gradually decompose to WO_3 and $WO_{3-\delta}$ (present up to 900 °C). At lower temperatures the various known oxygen deficient ($1 > \delta \geq 0$) tungsten oxides could not be distinguished from the XRD patterns due to their insufficient crystallinity.[62-64] To maintain clarity and comprehensibility, only selected tungsten oxide patterns have been depicted in summary figure above. It illustrates that the tungsten(VI) oxides are subsequently reduced to different tungsten(IV) oxides in between 800 and 900 °C. Those are then further reduced to W^0. At the last stage elemental tungsten is present along with several tungsten carbides and tungsten oxycarbide. Tungsten does not catalyse graphitisation in the probed temperature region.[27] Consequently there is no trace of ordered carbon structures visible in the corresponding XRD patterns.

The addition of iron has a substantial impact on the phase development, as the presence of iron causes phase coalescence at 700 °C. Here only *Ferberite*, $FeWO_4$, an also naturally occurring mineral, is formed. $FeWO_4$ is itself a very interesting compound as it has successfully been applied as a photocatalyst.[65] When stoichiometric amounts of Fe and W are used *Feberite* is formed phase pure; in the case of 3:1 ratio samples the excess iron is present in the form of Fe^0. The decomposing *Ferberite* is transformed to several tungsten and iron-tungsten carbides above 700 °C, but, in contrast to tungsten alone, no traces of any tungsten oxides are visible. Furthermore, with 3:1 ratio samples the excess iron causes graphitisation from this temperature on, for the 1:1 ratio samples graphitisation does not set in until 1000 °C, where iron is released from the decomposing ternary carbides.

SEM micrographs show little to no porosity present in the resulting products, which is confirmed by nitrogen sorption measurements that yield a moderate apparent BET surface area of 260 $m^2 \cdot g^{-1}$ for a Fe:W ratio 1:1 sample prepared at 1000 °C (**Figure 15**).

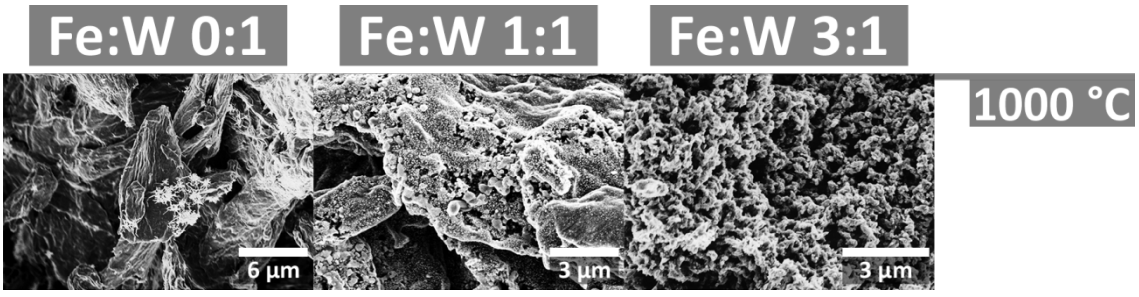

Figure 15: SEM images comparing samples of different tungsten-iron ratio prepared at 1000 °C.

The processes observed in XRD are clearly represented in the SEM micrographs. On the one hand the increasing iron content, due to irons graphitising nature, gives rise to larger degrees of porosity. On the other the samples prepared without any iron

are the only to display any remnants of tungsten oxide needles on the surface of the fibres.

It comes as little surprise that the remarkable shape retention is also observed with the tungsten-iron system, since tungsten does not graphitise the matrix in any way within the probed temperature range, and the previous chapter already showed that the graphitisation processes do not alter the micrometre and larger shape of the samples.

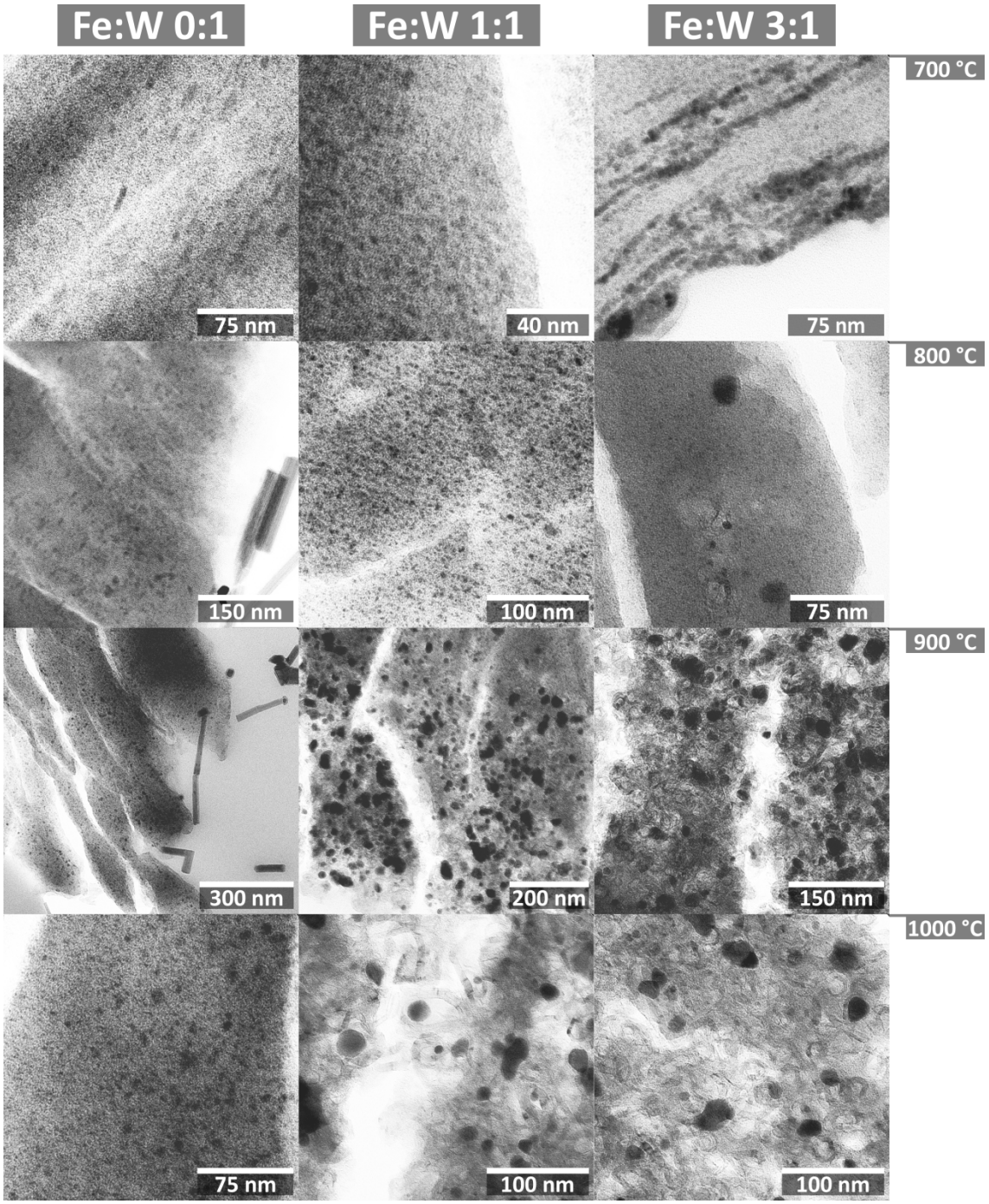

Figure 16: TEM study of the tungsten and tungsten-iron samples.

To conduct a more thorough investigation of the developing structures, TEM images of microtomed samples were taken. The study covers samples prepared from 700 to 1000 °C at all three ratios (**Figure 16**). The purely tungsten based samples show two intriguing features. One feature is tungsten oxide rods with average diameters of 10 – 50 nm that are up to 1 µm in length (**Figure 17**). The diagonal fractures seen here are again a result of the microtoming and not a feature of sample. Despite their well-defined shape they appear to be rich in defects since they cause striped selected area electron diffraction (SAED) patterns.

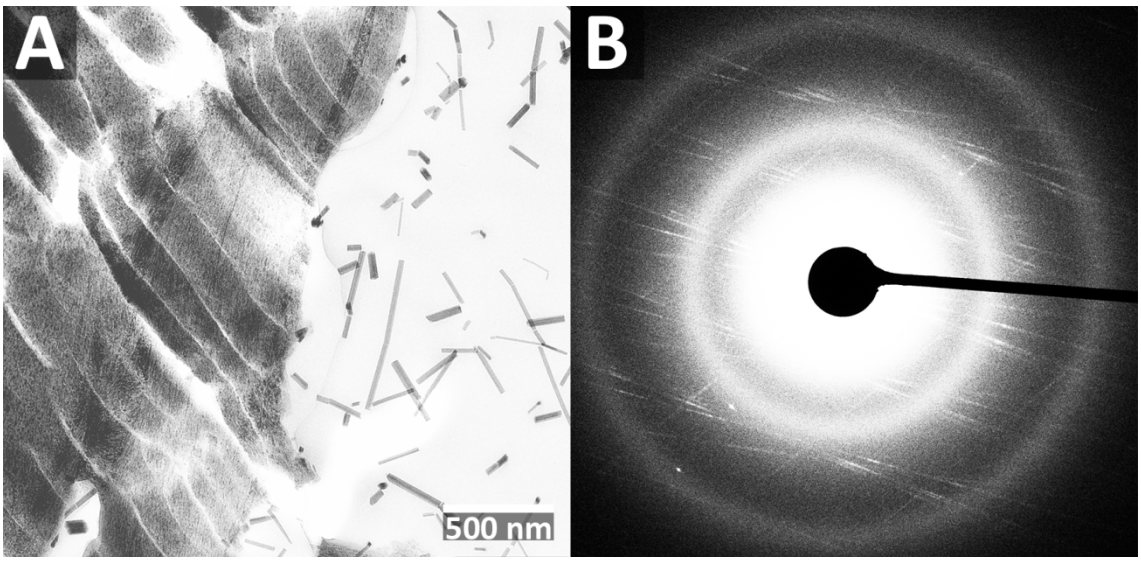

Figure 17: **A**: TEM of rod shaped tungsten oxides and **B**: the resulting striped SAED patterns of them found in samples prepared at 800 °C.

The other characteristic feature is that the cellulose fibres themselves seem structured, which is likely due to tungsten oxides forming within the carbon framework. The matrix imposes special limits on their growth and, due to compression of the surrounding carbon by the growing crystals, causes some short range order between the different crystals, which then causes the intricate patterns observed in TEM. Increasing the temperature visibly lowers the observed short range order within the fibres as well as the amount of tungsten oxide rods. The latter is to be expected, since XRD already showed the decomposition of the polyoxotungstates that are typically associated with rod shaped crystals.[66] Lastly at the highest temperature investigated the entire cellulose matrix is filled with nano crystallites, the largest ones reaching 3 nm in diameter.

Regardless of the entirely different phases that are formed upon addition of iron, the samples prepared at 700 °C with iron and tungsten appear very similar to the aforementioned samples prepared with tungsten alone. The only difference is that the iron containing samples completely lack the tungsten oxide rods and instead display a

higher concentration of particles towards the surface of the fibres, much like the dense shell of iron oxide particles observed in the previous chapter (see page 19).

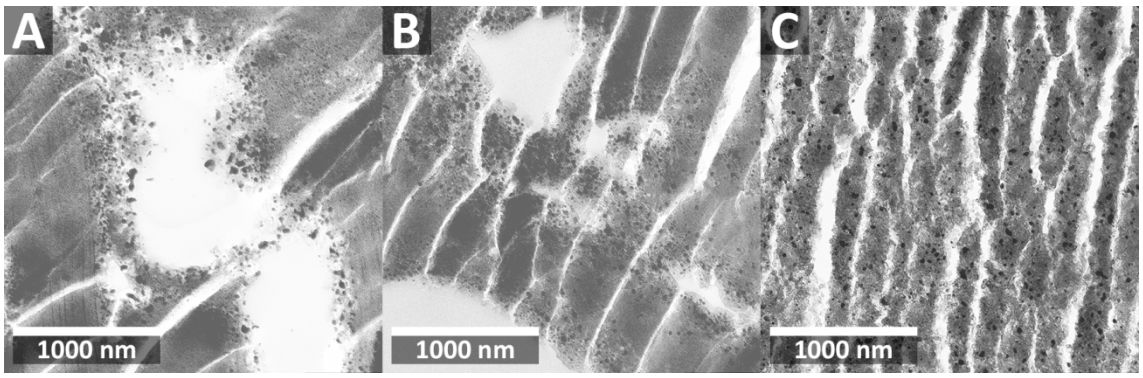

Figure 18: TEM micrographs studying the gradual etching during graphitisation. All samples prepared with tungsten to iron ratios of 1:1 at various temperatures. **A**: 800 °C. **B**: 900 °C. **C**: 1000 °C.

Increasing the reaction temperature further causes graphitisation to set in, which is accompanied by a curious effect (**Figure 18**). XRD patterns only indicate the presence of a single crystalline phase and TEM shows that at 700 °C particles are present throughout the carbon framework. Despite this, the graphitisation does appear to progress from the outside towards the centre of the fibres with increasing temperature. There are two possible explanations for this behaviour. One explanation is that the particles observed on the surface of the fibres are an amorphous iron oxide species that is not visible in XRD and graphitises the carbon according to the mechanism discussed in the previous chapter. The other reason could be that the *Ferberite* decomposes differently on the surface of the fibres. The latter could be caused by locally different $FeWO_4$ to carbon ratios. Within the fibres copious amounts carbon might quickly and fully reduce the *Ferberite*. On the surface instead higher mobility and concentration of $FeWO_4$ crystallites might cause intermediate reduction products (such as elemental iron or iron oxides) to be present long enough to form a eutectic with the carbon matrix and hence begin to graphitise the cellulose matrix. This effect is also observed with other metals and will be discussed in more depth in the section “Nickel-Iron-System” (see page 50).

Summary

The combination of water soluble iron and tungsten salts with cellulose and subsequent heat treatment under inert atmosphere will – within the reaction parameters that were probed in the work at hand – only yield *Ferberite* ($FeWO_4$) as a pure phase. Various mixed phase iron-tungsten-carbides have however successfully been synthesised by this route. Other work by our group, utilising alginate and gelatine as biopolymers and otherwise the same precursors, has shown that this system is somewhat difficult to control, but, with the right temperature treatment, pure Fe_3W_3C and nitride phases can be obtained from biopolymer precursors.[67] This strongly

indicates that it would only be a matter of finding the correct reaction conditions to yield pure phases with cellulose.

In contrast to previously mentioned work by our group employing cellulose, rather than dissolved biopolymer precursors, causes considerable porosity to be formed with overall surface areas exceeding 250 $m^2 \cdot g^{-1}$. Neither alginate nor gelatine yielded graphitised and hence porous products. The presumable reason for this is the interplay between cellulose and the iron. It allows for the formation of small iron oxide nanoparticles on the fibres surface, rather than the binding of singular ions to chelating moieties of the matrix. This seems to be essential for the graphitisation to happen and thus the porosity to be formed. This is supported by the observed consumption of the fibres from the outside inwards when comparing the samples prepared at different temperatures with iron present.

Even though the phase purity leaves room for improvement the presented synthesis is a general easy one-pot route to ternary oxides and carbides and it is only a matter of varying the reaction conditions to achieve the desired single phase systems. Optimisation of the reaction parameters is a very time consuming process and at the point of the writing of this work the corresponding experiments were still in progress.

MANGANESE-IRON-SYSTEM

In order to assess the transferability of the knowledge gained in the previous section a second system was probed for its ability to form ternary carbides containing iron. Manganese, a metal that is structurally closer to iron, was chosen since tungsten proved to be a somewhat difficult partner for iron in terms of phase purity and size homogeneity of the resulting product. Nevertheless, the combination with manganese promises to yield equally interesting ternary compounds, since manganese is also known to be a versatile catalyst.[68-70]

The formation of phase-pure ternary carbides turned out to be a lesser challenge, and the synthesis of pure $Mn_{0.75}Fe_{2.25}C$ was achieved with the samples containing corresponding iron to manganese precursor ratio. The syntheses were accompanied by the formation of considerable surface areas (**Table 2**) with micrometre sized pores and a hierarchical pore system, which is essential for the applicability of a material in catalysis.[71]

Table 2: Summary of the apparent BET surface areas ($SA_{BET, app.}$) obtained from the Mn-Fe system.

Mn:Fe Ratio \ Temperature	800 °C $SA_{BET, app.}$ [m^2/g]
1 : 0	280
1 : 1	380
1 : 3	340

In addition to the large micrometre pores, fractions of macro and micro-pores are also formed. Having such hierarchical systems at ones disposal is very interesting in itself. However, since the aim of this section is assessing the temperature dependent formation of the various phases achievable with the ternary system probed, only some initial discussion of the micrometre sized pores formed by this system will be made. The bulk of the discussion is found in the next chapter in the section "Cobalt-Iron-System". There the passage "Controlling the Porosity" will deal with the prospect of tuning the ratio of the different pore-size fractions.

Akin to the investigation in the previous section the phase evolution was monitored with the help of XRD spectroscopy (**Figure 19**). A reference study using only manganese and cellulose was conducted to enable better judgment of the effects observed and to make it possible to attribute them to the contribution of one metal or the other, or to identify them as possibly synergistic effects.

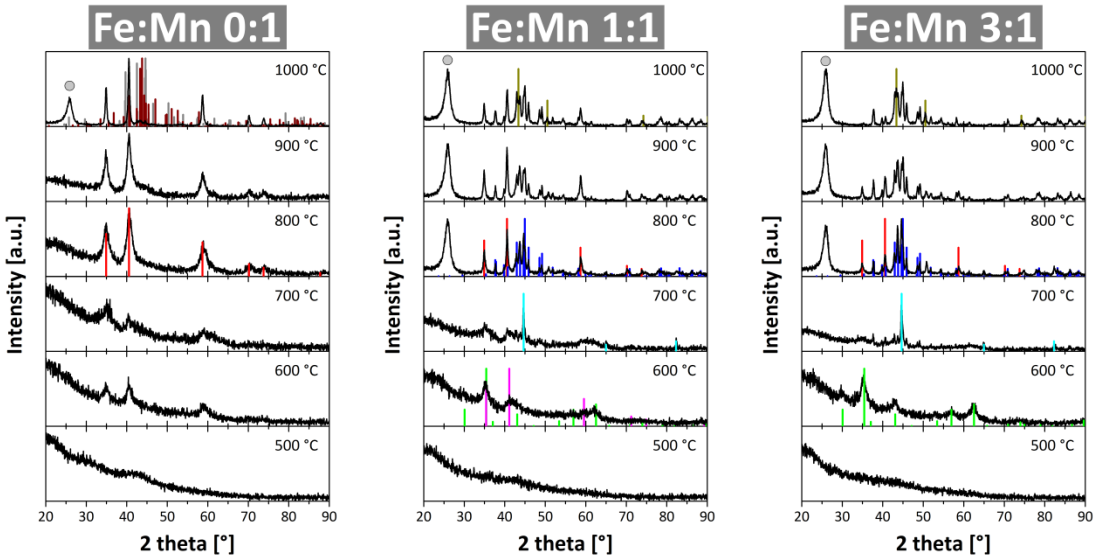

Figure 19: XRD summary of the phase developments in the manganese-iron-system. The reference patterns marked are: Blue: $Mn_{0.75}Fe_{2.25}C$ (ICDD 04-002-8999), Red: MnO (ICDD 04-005-4310), Magenta: $Mn_{0.5}Fe_{0.5}O$ (ICDD 04-005-9719), Grey: Mn_7C_3 (ICDD 04-007-1048), Wine: Mn_5C_2 (ICDD 04-007-1125), Green: Fe_3O_4 (ICDD 04-015-3102), Dark Yellow: $FeN_{0.0589}$ (ICDD 01-075-2130), Cyan: Fe^0 (ICDD 04-014-0360) and the grey circle at 26° 2 theta is attributed to graphitic carbon (ICDD 04-015-2407). Larger prints of the patterns can be found in the appendix.

Manganese could hardly be reduced by carbon alone, as was expected. Only at 1000 °C were first reduction products visible, namely traces of two manganese carbides Mn_5C_2 and Mn_7C_3, along with substantial amounts of graphitic carbon. Manganese and cellulose solely forms manganese(II) oxide, however, the formed nanoparticles are very small (< 4 nm). The first crystalline MnO nanoparticles emerge already at 600 °C. Also, according to XRD, the manganese oxide nanoparticles formed at 600 °C do not grow significantly up to 900 °C. The first major change in the phase composition takes place at 1000 °C. A steep increase in the MnO particle size from 5 nm to 21 nm (both values obtained from the *Scherrer* equation) can be observed there. This is accompanied by the emergence of a pronounced peak stemming from graphitised carbon and traces of crystalline Mn_7C_3 and Mn^0 as minor phases. As opposed to tungsten, manganese catalyses the graphitisation of cellulose in the absence of iron. The fact that graphitised carbon appears along with manganese carbides hints at a similar graphitisation mechanism as observed with iron.

The addition of iron causes a significant drop in graphitisation temperature from 1000 °C to 800 °C and gives rise to a multitude of Fe/Mn phases. At 600 °C, only Fe_3O_4 and $Fe_{0.5}Mn_{0.5}O$ can be found in the XRD patterns. So in this case the formation of iron oxide and the mixed metal oxide $Fe_{0.5}Mn_{0.5}O$ precedes the formation of crystalline manganese(II) oxide. At 800 °C and above MnO becomes visible along with an increase in Fe^0 and $Mn_{0.75}Fe_{2.25}C$ as additional phases. From 900 °C on there are traces of a nitrogen depleted iron nitride phase ($FeN_{0.0589}$). The formation of this phase is likely due to the use of nitrate precursors. By replacing them with the corresponding acetates $Fe(CH_3CO_2)_2$ and $Mn(CH_3CO_2)_2$, the formation of the nitride is suppressed without any other change to composition. This was confirmed for several selected temperatures and compositions; an example of this will be shown in the following analyses. Nonetheless this work will present the nitrates to give a more comparable picture among all investigated systems, since all other metal precursors employed were nitrates.

Increasing the iron content from 1:1 to 3:1 only gives rise changes in the relative amounts of the phases observed before. Most notable is that this causes the complete disappearance of MnO at 1000 °C leaving only the ternary carbide $Mn_{0.75}F_{2.25}C$ and again traces of a nitrogen depleted iron nitride phase ($FeN_{0.0589}$). In this case the use of the corresponding acetate precursor prevents the formation of the iron nitride phase and leaves pure $Mn_{0.75}F_{2.25}C$ along with graphitic carbon (**Figure 20**).

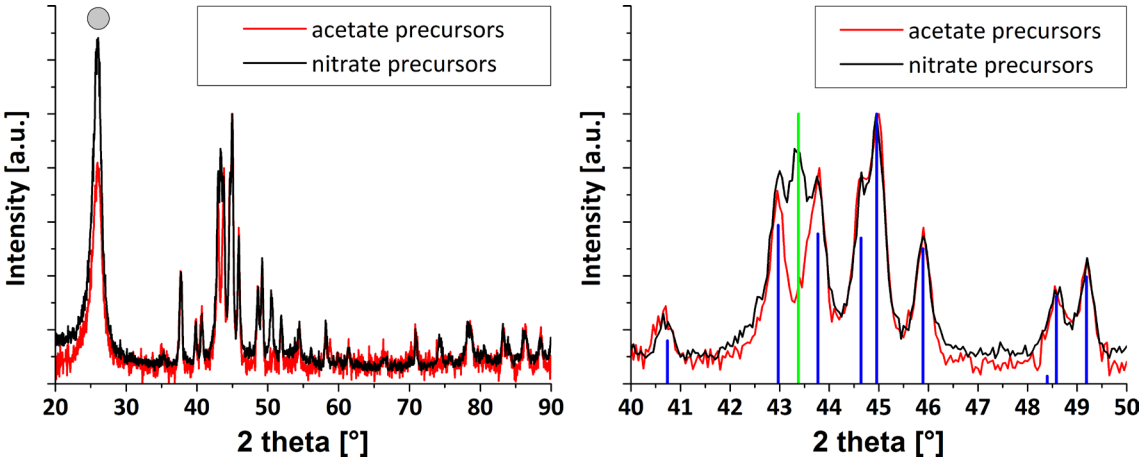

Figure 20: Comparison of the XRD patterns resulting from nitrate and acetate precursors reacted with cellulose at 1000 °C. The reference patterns marked are: Blue: $Mn_{0.75}Fe_{2.25}C$ (ICDD 04-002-8999), Green $FeN_{0.0589}$ (ICDD 01-075-2130) and the grey circle at 26° 2 theta is attributed to graphitic carbon (ICDD 04-015-2407).

The morphological developments of the system were followed with the help of SEM imaging (**Figure 21**). The SEM micrographs show that the cellulose matrix is again intact and the initial shape is retained well.

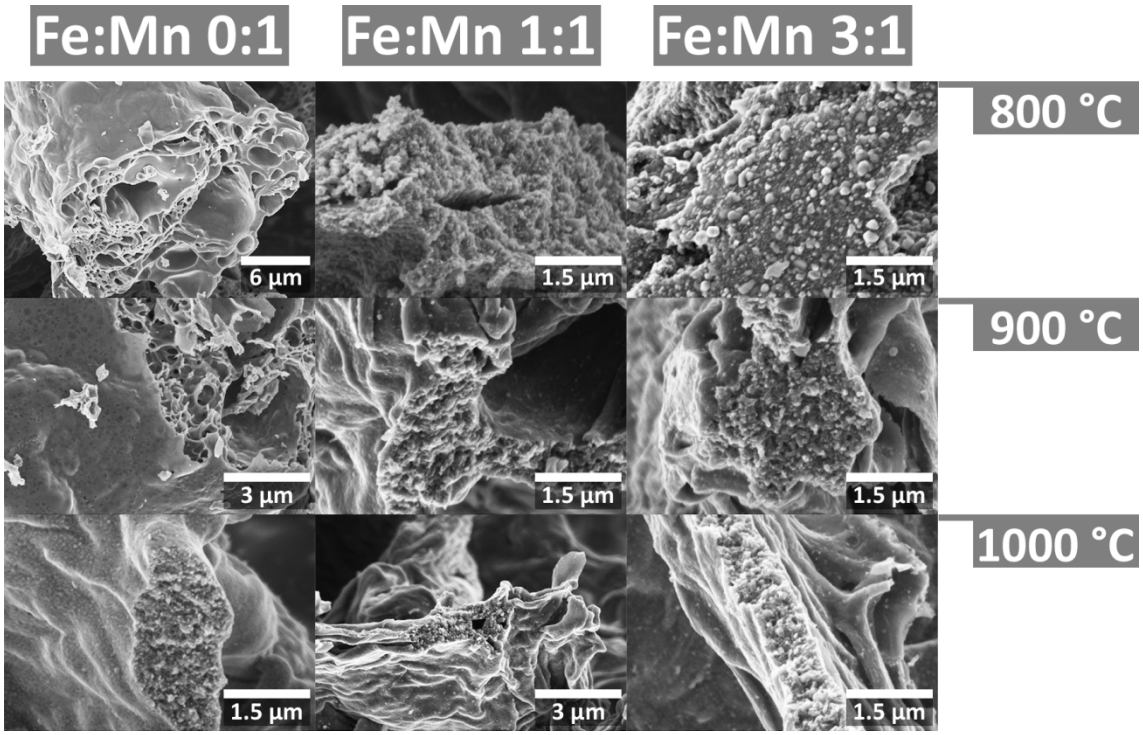

Figure 21: SEM study covering all Fe:Mn ratios probed at temperatures from 800 to 1000 °C.

With increasing amount of iron present it becomes more difficult to distinguish the samples prepared with iron and manganese from the iron/carbon system discussed in the previous chapter. Manganese by itself however can cause significant damage to the morphology. The observed changes reach up to the point of full-fledged alteration on the µm scale (**Figure 22**).

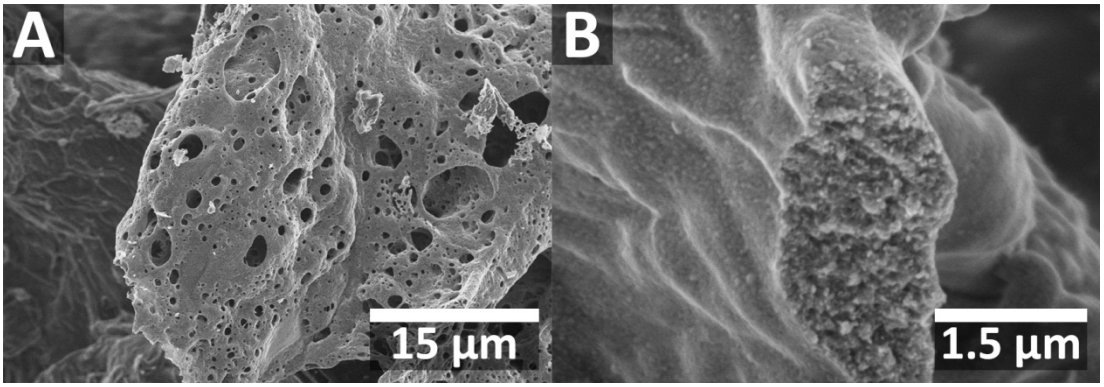

Figure 22: Example of a strongly altered region (**A**) and a non-altered region (**B**) in a Fe:Mn 0:1 sample prepared at 1000 °C.

The alterations on the micrometre scale are of a localised nature, meaning that only some parts of the samples undergo these stark changes. For applications, such as catalysis, not only high surface areas are of importance, but also the accessibility of these surfaces. This accessibility needs to be facilitated by large pores suitable for mass transport, such as the ones observed here.[72]

Not all fibres lose their morphology, some remain – at least from the outside – unchanged (**Figure 21**). A conclusive reason for this eluded analysis and is still open for speculation. Inhomogeneity in the starting material can be ruled out due to the way that the precursors are prepared. One of the two most likely reasons is that the parts of the sample that are in direct contact with the crucible or the top layer of the sample that interfaces with the atmosphere – even though the crucibles are lidded – behave somewhat differently. One compelling argument against this is the fact that the ratio of unaltered to changed fibres should be constant with temperature, since the amount of sample at the interfaces remains constant. Also, the fraction of fibres with small pores should greatly outnumber the other, since a much larger fraction of the material is "within" the sample, but neither is the case. The other argument that speaks against this hypothesis is that exactly this test has been performed with the Fe-C samples to ensure homogeneity and absolutely no difference between samples taken from the surface, the edge, the walls, and the bottom of the crucible or the centre of the powder was found. The other reason causing the observed inhomogeneity could be that the fibres which bear significant changes in appearance may simply have lost their outer shell. The material appears highly porous but it is also brittle. Due to the large pores it could lose significant parts of the outer most carbon layer, which resembles the cellulose morphology and remain otherwise intact. Against this speaks that a few samples seem to only possess very small pores akin to the ones formed by iron. Since theses fibres always have retained the morphology of the cellulose, this could mean that their outer shell simply did not break off, but that raises the question why these fibres did not form micrometre porosity in the first place. This general effect will be

observed with other metal combinations as well and hence receive a more thorough analysis in the upcoming chapters (see page 61).

Lastly, in agreement with the small crystallite sizes derived from XRD patterns, manganese oxides only become visible on the surface and cleaving edges of broken cellulose fibres at very high temperatures, after their size has increased significantly.

To gain a closer look at the nm changes that take place during the heat treatment of the samples all experimental conditions probed in the SEM study above were also investigated with the help of TEM (**Figure 23**).

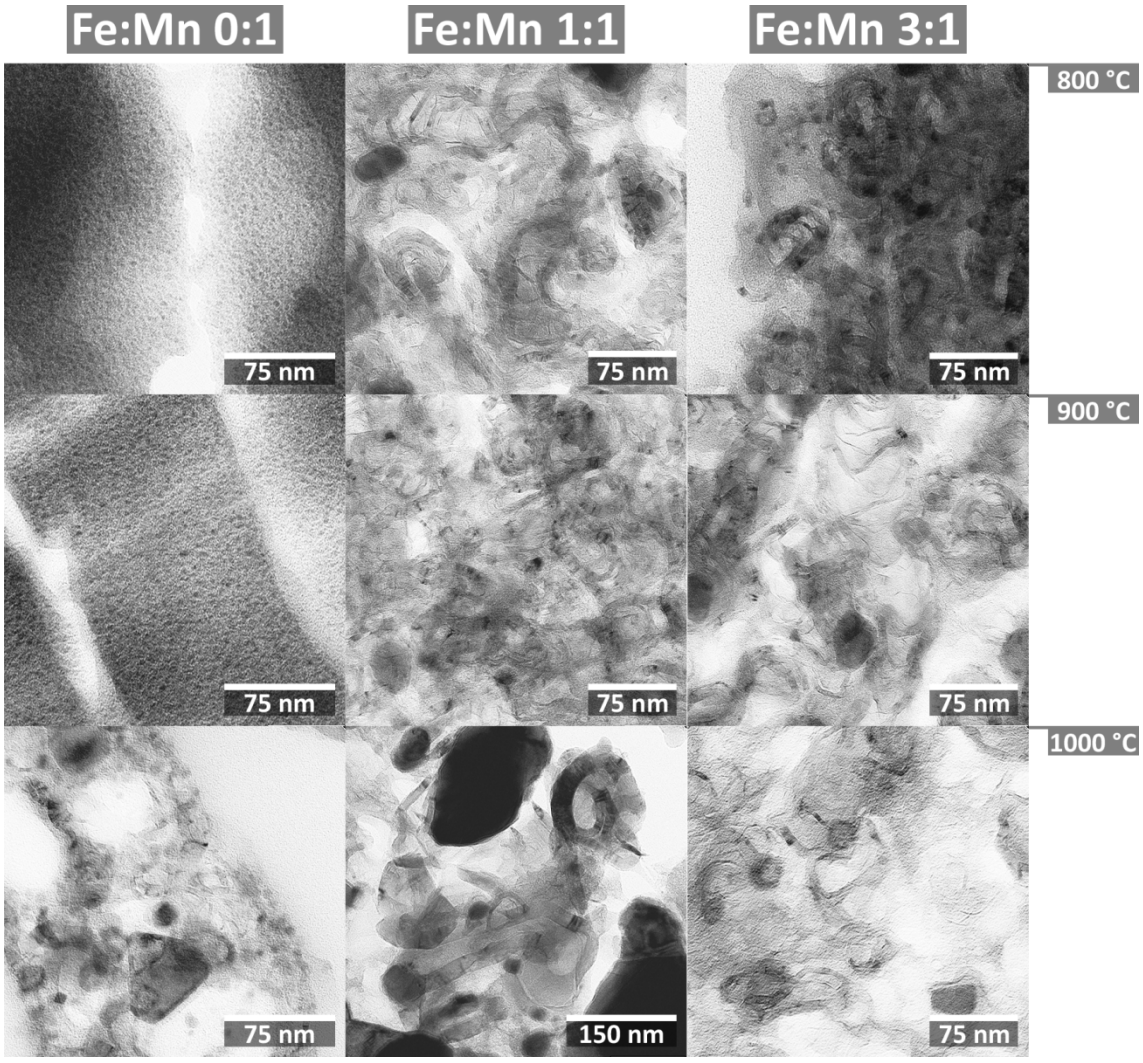

Figure 23: TEM images of all Mn-Fe metal ratios probed at temperatures from 800 to 1000 °C.

As suggested by peak broadening observed in XRD patterns TEM micrographs of manganese-only samples reveal very small (< 1.5 nm) manganese oxide nano particles, which are finely and homogeneously dispersed in the carbon matrix. Despite their small size they remain morphologically unchanged even at 900 °C.

The observed drastic change in phase composition, when increasing the reaction temperature to 1000 °C, comes about with similarly drastic changes in morphology. TEM shows now many types of nanoparticles that differ greatly in size and shape, from small spherical particles with diameters of 5 to 10 nm, to a larger 25 nm fraction of mostly spherical particles, to facetted particles of up to more than 100 nm. Moreover, TEM shows that parts of the samples completely lose their structural integrity, which is the same result that was already observed in SEM micrographs (**Figure 24**).

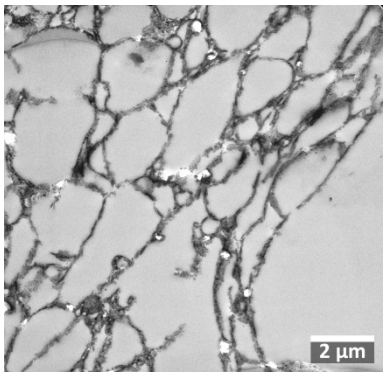

Figure 24: TEM image depicting the loss of structural integrity when heating cellulose in the presence of manganese to 1000 °C.

As could be expected from SEM and XRD, the addition of iron governs the morphological appearance of the composite causing them to strongly resemble the samples prepared with an iron precursor alone. In fact the only striking difference is that there are two fractions of nanoparticles observed in the manganese-iron system. Aside from the larger nanoparticles (about 50 nm in diameter), all of which have a carbon shell, there is a second type with diameters of 5 to 10 nm that seem to be bare of any carbon. Due to their small size and the phase development observed in XRD, they can be identified to be remnants of the oxide phases that are formed initially. Additionally the carbon appears to be highly ordered and comprises tubular structures and ordered bands that span several hundred nanometres. Interestingly, the amount of added iron has little bearing on the observed changes making the 1:1 and 3:1 samples virtually indistinguishable. Only actual particle counting shows that the amount of large, shelled particles increases in the 3:1 samples. An increased reaction temperature of 900 °C results in practically no change in morphology with either of the metal ratios. The only observable difference between the two is slight coalescence of the smaller nanoparticle fraction resulting in average diameters of 20 to 25 nm. Where the 100 K temperature increase caused little change in morphology upon heating from 800 °C to 900 °C, the temperature increase to 1000 °C results in distinct changes in the structures and is clearly visible in TEM micrographs. While in both cases the carbon framework has experienced structural damages due to the formation of the larger nanoparticle fraction growing even further, with some particles reaching almost

500 nm in diameter. The smaller particle fraction has grown slightly and, more importantly in the 3:1 case, all the smaller spherical particles now possess a carbonaceous shell suggesting they also have undergone a phase change to manganese-iron-carbide (**Figure 25**).

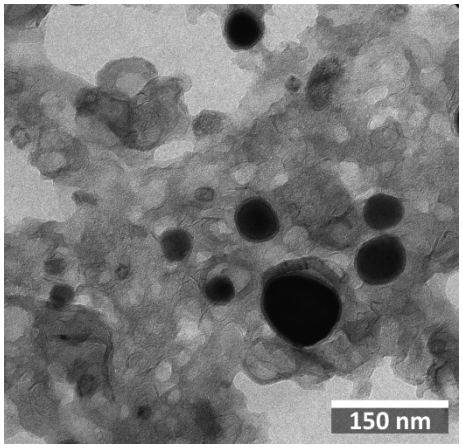

Figure 25: TEM image of a Fe:Mn 3:1 sample prepared at 1000 °C showing that all particles possess a carbon shell.

In the case of a metal ratio of 1:1 not all particles possess a shell, and additionally an entirely new type of particles appears: cubic or rod shaped particles (**Figure 26**).

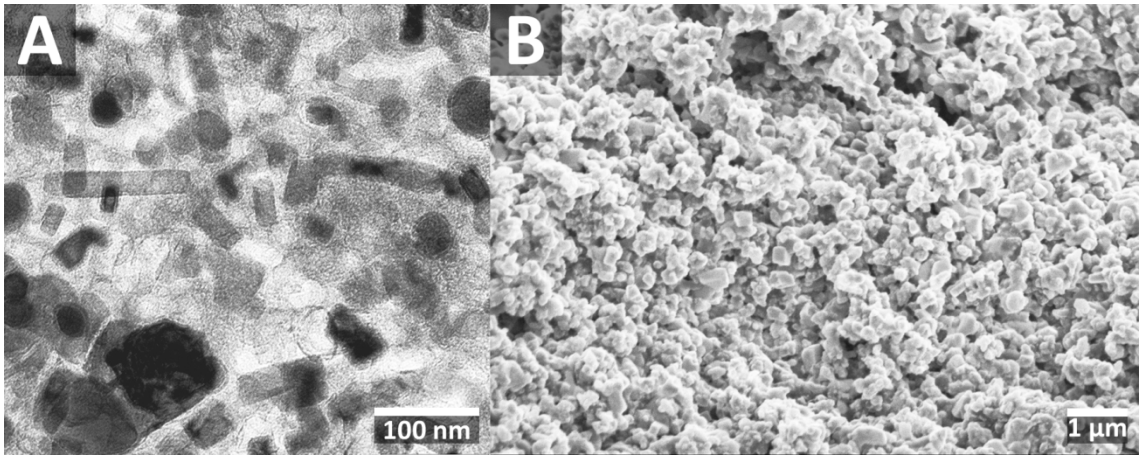

Figure 26: **A**: TEM image and **B**: SEM image of a Fe:Mn 1:1 sample prepared at 1000 °C showing the rod-shaped particles that have emerged.

Rods of various manganese oxides have been reported in the literature,[73-76] among those the synthesis of manganese(II) oxide is extremely rare and a high temperature synthesis has not been described at all. In fact the cubes and rods are so prominent that, upon closer inspection, they can even be seen in SEM micrographs where the fibres have fractured.

Summary

A study of the phase transitions undergone by reacting aqueous solutions of iron and manganese salts with cellulose in the high temperature regime from 500 °C to

1000 °C has been conducted. The reactions always progress *via* the corresponding oxides and yield mixed phases while transitioning from one state to the other. However, by carefully tuning the reaction conditions, several interesting products can be obtained in pure form.

Manganese and cellulose alone yield homogenous ultra-small MnO nanoparticles dispersed in carbon at temperatures as low as 600 °C. This is significant, since all other manganese oxides should be easily available *via* controlled further oxidation of these manganese(II) oxides.

Furthermore the synthesis of $Mn_{0.75}Fe_{2.25}C$ nanoparticles is demonstrated for the first time in a nanoparticulate form. This is achieved simply by combining aqueous solutions of manganese and iron acetate, in a ratio of one to three, with cellulose and calcining the resulting slurry under inert atmosphere at 1000 °C. The possibility to produce the ternary carbide in an easy and large scale one-pot synthesis allows for the material to now be tested for its catalytic properties. Future work will also encompass a search for applications outside the field of catalysis.

V. METAL(0) NANOPARTICLES

INTRODUCTION

The synthesis of metal(0) nanoparticles is arguably one of the most studied phenomena in the realm of materials science. Tens of thousands of publications have been devoted to said matter.[77] The reason for this enormous attention is the diverse applicability of these structures. The most important of which is catalysis,[78] but also applications ranging from medicine to spectroscopy and sensors and many more have been implemented.[79] In addition to metal(0) nanoparticles bimetallic alloy nanoparticles have lately received much attention due to their enhanced properties and additional tunability.[80-81]

The main concern with the preparation of metal(0) nanoparticles that a materials scientist is faced with is the stabilisation of these nanoparticles. This typically addresses a twofold issue: one is the stabilisation of the particles against aggregation or coalescence, the other is their stabilisation against chemical changes, most notably oxidation. A common solution to both problems is the use of stabilising agents such as surfactants.[82]

In the previous chapter, samples containing homogenously distributed, very small MnO nanoparticles dispersed in the carbon framework have been presented. Since manganese(II) oxide, in the form of nanoparticles, is prone to further oxidation, this suggested that the carbon matrix is a potent stabilising agent. Also, no coalescence of particles was observed in a wide temperature regime suggesting that the carbon structure is a good separating agent as well.

Non-noble metal(0) particles are especially prone to undergo chemical changes along with the usual ripening processes, and consequently are harder to stabilise, yet they are very important catalysts.[82] From the findings of the last chapter cellulose appeared to be an ideal choice for dispersing and stabilising them and several metals of recent interest such as cobalt, nickel, palladium and copper, were selected as examples.

This chapter presents a very general synthesis path to well defined, stable nanoparticles. The synthesis will be exemplified by the preparation of metal(0) and metal alloy particles composed of Cu, Ni, NiFe, $Ni_{0.32}Fe_{0.68}$, NiPd, CoFe and Co_3Fe_7. All syntheses described in this chapter will be based on CFP and MCC as the cellulose precursors and bivalent nitrates of the respective metals as the metal source, all other reaction parameters (including the probed metal ratios) are the same as in the syntheses in the previous chapters (see page 27).

COPPER-IRON-SYSTEM

The combination of iron and copper produced foremost well dispersed stable Cu^0 nanoparticles. During the course of the analyses it turned out that, despite their small size of approximately 9 nm, the particles are in fact found to be aggregates of very small, crystalline copper clusters of only a few atoms. The next discovery was that copper is able to direct the graphitising power of iron. This is a twofold property, on the one hand copper seems to direct the formed tubular carbons to align themselves and to grow in straight lines. On the other hand the fcc structure of copper appears to promote the formation of diamond-like carbons (that have a fcc structure themselves) at very low temperatures. None of the ratios or temperatures probed did however yield any sort of combination of the metals, neither ternary oxides nor ternary carbides nor was any form of alloying observed. A summary of the observed crystalline phases, as determined by XRD spectroscopy, can be seen in **Figure 27**.

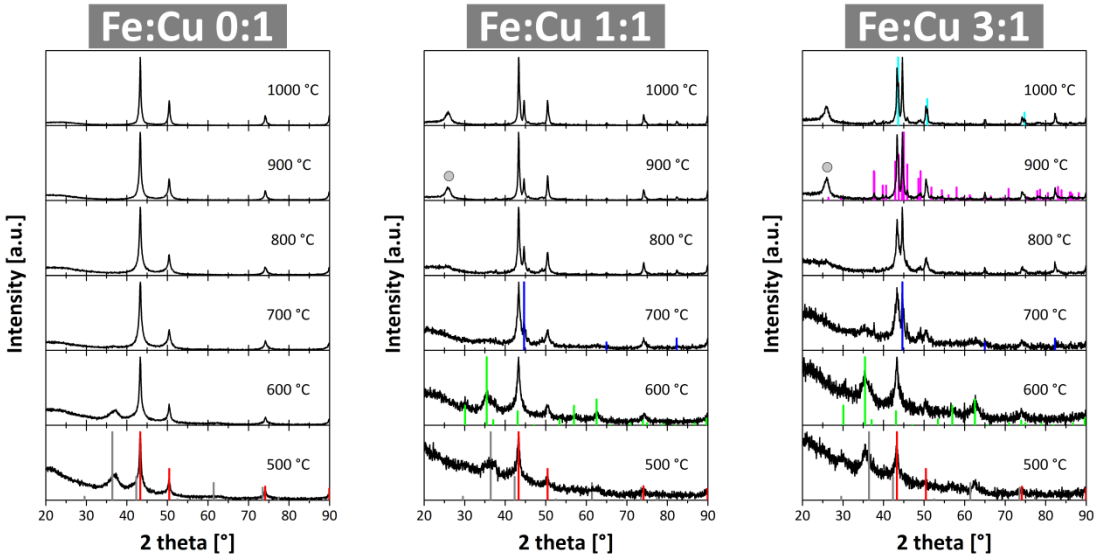

Figure 27: Summarised XRD patterns of the temperature and ratio dependent analysis of the copper-iron system. The reference patterns marked are: Grey: Cu_2O (ICDD 04-007-9767), Red: Cu^0 (ICDD 00-004-0836), Green: Fe_3O_4 (ICDD 04-015-3102), Blue: Fe^0 (ICDD 04-014-0360), Magenta: Fe_3C (ICDD 00-035-0772), Cyan: Diamond-Like Carbon (ICDD 00-060-0053) and the grey circle at 26° 2 theta is attributed to graphitic carbon (ICDD 04-015-2407). Larger prints of the patterns can be found in the appendix.

Copper alone will even form crystalline copper nanoparticles at temperatures as low as 500 °C. At low temperatures those particles are still accompanied by copper(I) oxide particles, which disappear above 600 °C. The crystallinity of the copper particles appears virtually invariant with temperature; the *Scherrer* equation yields a crystallite size of 20 nm.

The addition of iron to the system initially does not show any unexpected alterations. Upon heating Fe_3O_4 is observed as an additional phase and moderate amounts of iron will transform directly into Fe^0, larger will additionally produce small amounts of Fe_3C. No form of combination of the two metals is observed. One puzzling

change that can be seen though is an additional set of peaks corresponding to an fcc lattice that is smaller than the one of copper (**Figure 28**).

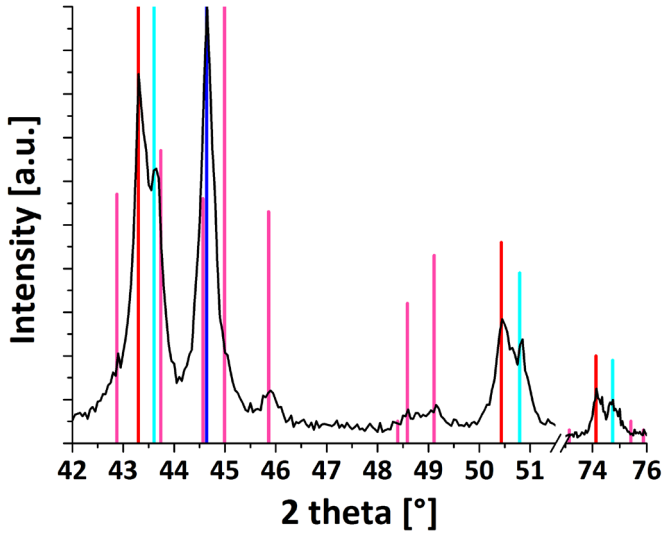

Figure 28: XRD pattern of a ratio 3:1 Fe:Cu sample prepared at 1000 °C. Red: Cu^0 (ICDD 00-004-0836), Blue: Fe^0 (ICDD 04-014-0360), Magenta: Fe_3C (ICDD 00-035-0772), Cyan: Diamond-Like Carbon (ICDD 00-060-0053)

This phase has with reasonable certainty been identified as a diamond-like carbon (DLC) phase that is produced as a result of the presence of the fcc copper during the graphitisation process. The fact that DLC can be obtained from the catalytic conversion of carbon black with iron has been reported previously.[83] Infrared Raman spectroscopy supported these findings well.[51, 84-86]

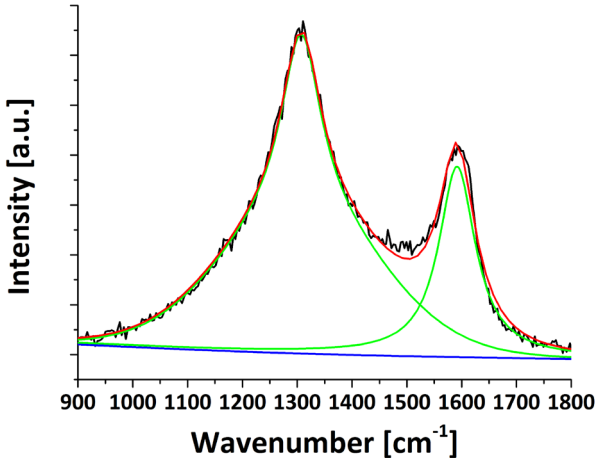

Figure 29: Raman spectrum of a ratio 3:1 Fe:Cu sample prepared at 1000 °C. Black: measured spectrum, Green: fitted peaks, Blue: fitted baseline and Red: cumulative fitted curve.

When interpreting infrared Raman spectra, much care has to be taken to judge the different dispersion effects properly. *Ferrari* and co-workers have done extensive work in this area and delivered several good reviews of the matter discussing critical as well as disputed points.[51, 86] In summary, considering the employed laser wavelength

of 785 nm, the peak positions of 1307 cm^{-1} and 1591 cm^{-1}, shape and relative intensity as well as relative signal areas suggest the presence of diamond-like carbons.

The structural developments on the micrometer scale were followed *via* SEM measurements. At every stage of the reaction nanoparticles could be seen to grow on the surface of the carbon fibres. They were of several ten up to a few hundred nanometres in diameter and preferentially accumulated between ridges of the surface texture of the fibres (**Figure 30**).

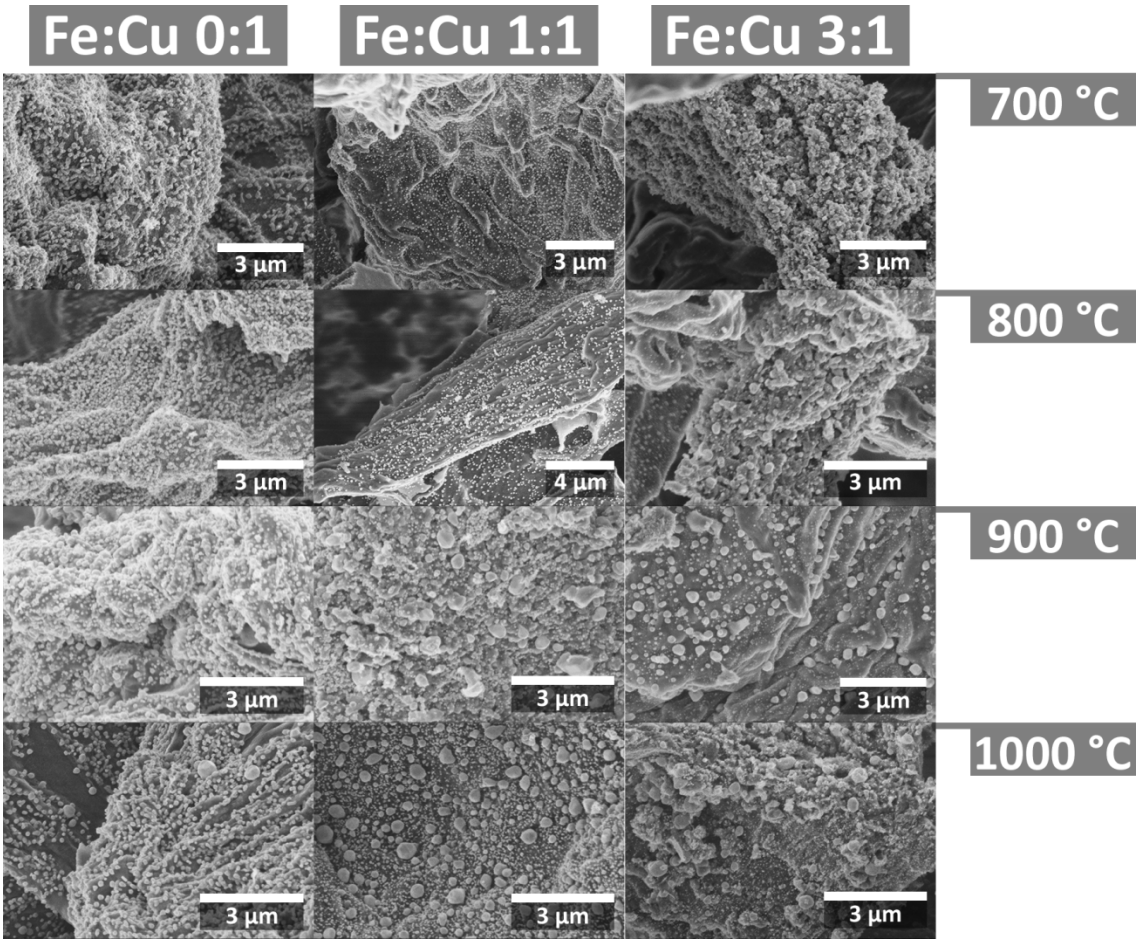

Figure 30: SEM micrographs of all metal ratios probed at temperatures from 700 to 1000 °C.

The SEM micrographs strongly suggest that there is, at least size wise, a large fraction of copper nanoparticles present. The addition of iron had apparently little impact on the size and density of the nanoparticles, but this was expected as there was no change in dependence of the iron content observed in XRD patterns. In TEM images however the combination of the two metals did prove to have an impact on the overall morphology of the product. Copper alone yielded well controlled nanoparticles of an apparent average diameter of 9 nm as determined from TEM micrographs (**Figure 31**).

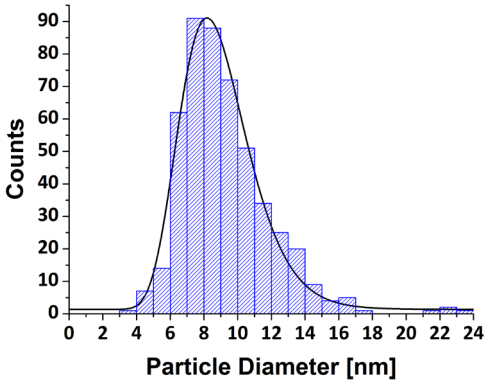

Figure 31: Particle diameter histogram of Cu nanoparticles prepared at 800 °C as determined from TEM images.

Initially the samples appear to be mere physical mixtures of the two reactions and their respective products, since it has been found that iron develops separately from the copper phase. Large amounts of iron and temperatures above 800 °C, however, show that the addition of copper alters the graphitisation process in such a way that the tubular carbons preferentially grow in bundles and within common planes. This causes the bundles to appear as straight lines of several µm length in the UM cuts. Those common planes however appear to be randomly tilted throughout the material (**Figure 33**). Since, aside from this, the two reactions happen separately, the reader is referred to the third chapter for a discussion of the phase developments of pure iron. Intriguing about the behaviour of copper is that it appears to coalesce primarily on the surface of the fibres or in cavities where the iron has opened up the structure through graphitisation. This gives rise to two structural effects. One is that the surface of the fibres is populated with large copper nanoparticles. The other is that this coalescence causes a depletion zone, which appears void of any particles, close to the surface of the fibres. This feature is observable with and without the presence of iron in both SEM and TEM (**Figure 32**).

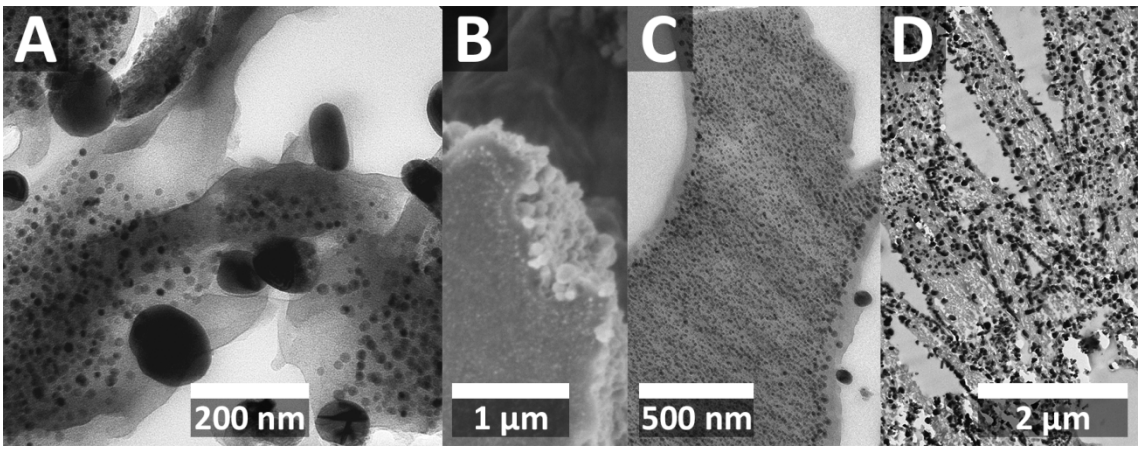

Figure 32: Surface depletion effect. **A-B**: TEM and SEM of a pure copper sample prepared at 1000 °C. **C-D**: TEM of Fe:Cu 3:1 samples prepared at 900 °C.

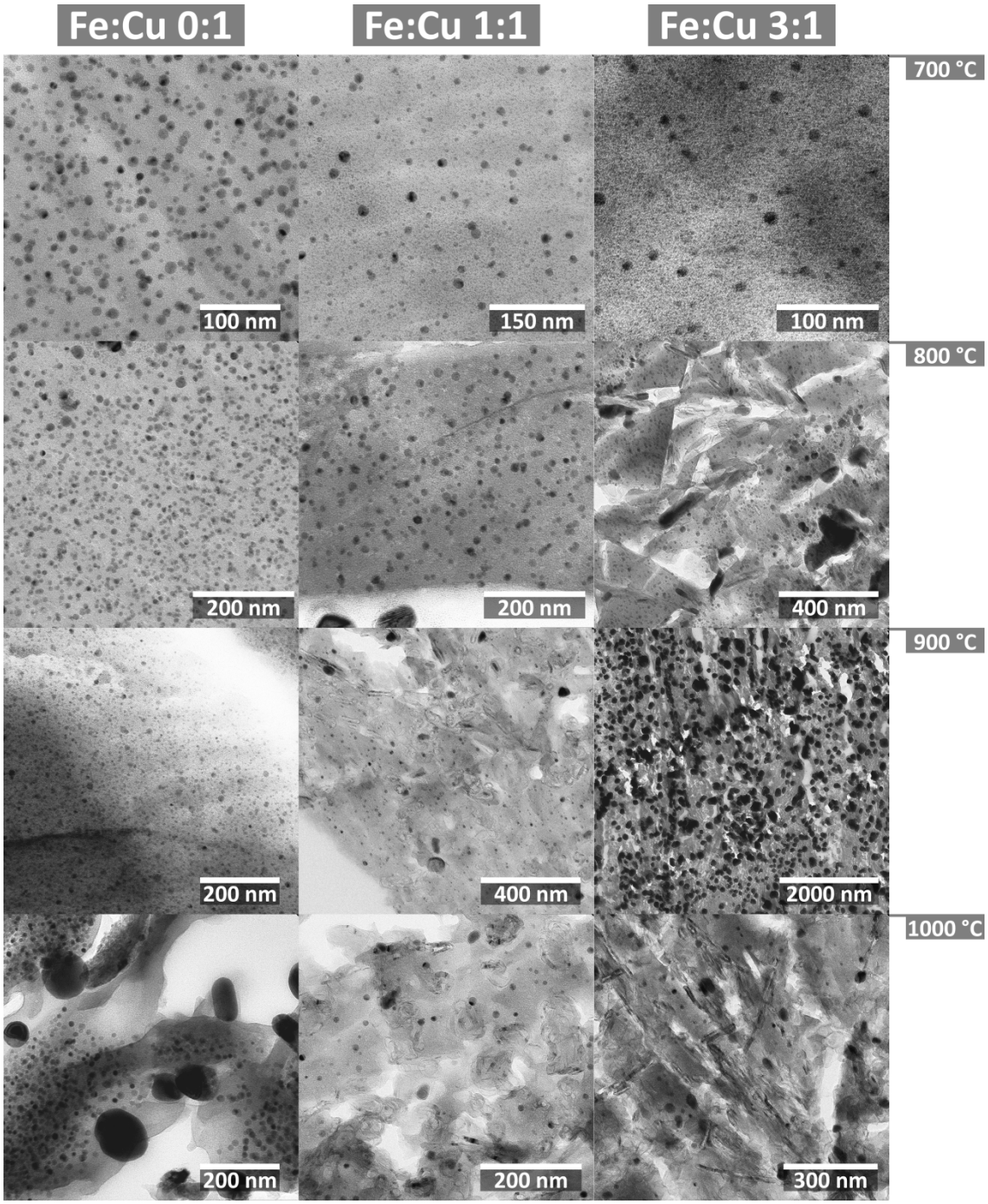

Figure 33: TEM images of all metal ratios probed at temperatures from 700 to 1000 °C.

A closer look at the copper nanoparticles reveals another surprising feature: they actually consist of few-atom copper clusters, rather than being comprised of larger crystallites or even single crystals as XRD initially suggested (**Figure 34**).

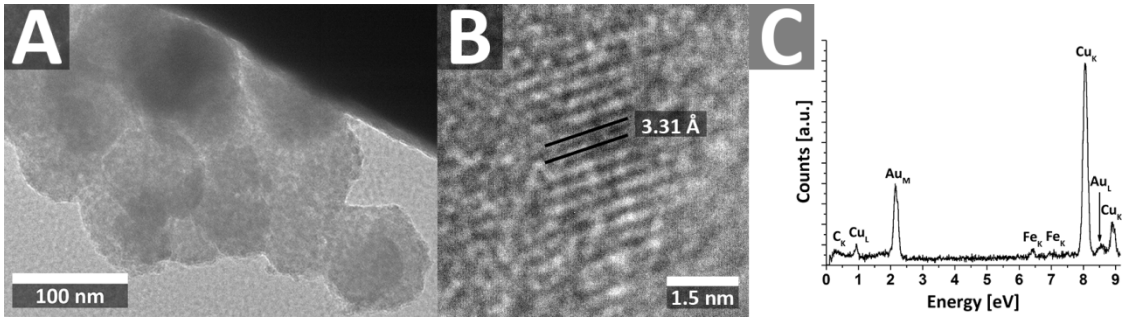

Figure 34: **A** TEM image of the copper nanoparticles. **B**: HR TEM of a crystalline copper cluster within the particles. **C**: corresponding EDX spectrum.

The fact that the lattice fringes observed in high resolution images do not to coincide with the copper lattice is an effect that has been reported previously. There copper clusters of high quality also showed fringes corresponding to double reflections within the cluster.[87] The fact that XRD shows comparably sharp peaks is most likely due to the fact that the particles on the fibre surface are in fact comprised of larger crystallites. The signal caused by the larger fraction would be much stronger and superimposed on the broad peaks caused by the copper clusters.

Attempts to release the copper clusters from the carbon framework and obtain dispersed nanoparticles have been made despite their small size. Releasing the nanoparticles from the carbon framework was achieved through prolonged ultrasonic treatment in toluene in the presence of oleic acid. Even though releasing the particles was possible, they could not be held in solution, since they were simply too instable due to their small size and dissolved quickly. A full study of possible dispersing agents has, however, not be conducted and would be a very interesting point for further research. Also, a study involving UV Raman spectroscopy to directly evaluate the sp^3 fraction within the DLC would be of high significance.

Summary

Copper nanoparticles have been produced and stabilised in a carbon framework. The particles were actually copper clusters of sizes below one nanometre with an approximate atom count of less than 200 atoms per copper cluster. The combination of copper and iron enabled the formation of a diamond-like carbon phase that was catalytically produced by the iron and stabilised by the fcc lattice of the copper.

The presented approach makes it possible to produce stabilised copper nanoparticles and DLCs in very large amounts – preliminary tests yielding several grams have been made.

NICKEL-IRON-SYSTEM

Nickel yielded, much like copper, well dispersed and highly stable metal(0) nanoparticles. They were of well controlled size with diameters of (5.5 ± 0.5) nm as determined from TEM and crystallised at temperatures as low as 600 °C. Increased temperature treatment, at and above 900 °C, caused catalytic graphitisation to occur, similar to the processes observed with iron. However, the graphitised structures were of somewhat different morphology as will be discussed in the course of this section. The use of nickel precursors furthermore gave rise to micrometre sized pores in addition to the pores caused by graphitisation.

As opposed to copper, nickel will form various alloys in the presence of iron due to their similar size and chemical nature. In particular the alloys NiFe and $Ni_{0.32}Fe_{0.68}$ were obtained. A peculiar behaviour observed with this was that iron and nickel formed at different locations within the cellulose framework and only upon graphitisation and the thus caused omnipresence of iron throughout the carbon matrix were pure alloys obtained.

This section will present the synthesis of nanoparticles of extraordinary quality consisting of nickel and binary alloys of nickel and iron as well as nickel and palladium. It will moreover cover promising results regarding the dispersability of said nickel nanoparticles.

The crystalline phases observed in XRD patterns at the various temperatures and ratios are summarised in **Figure 35**.

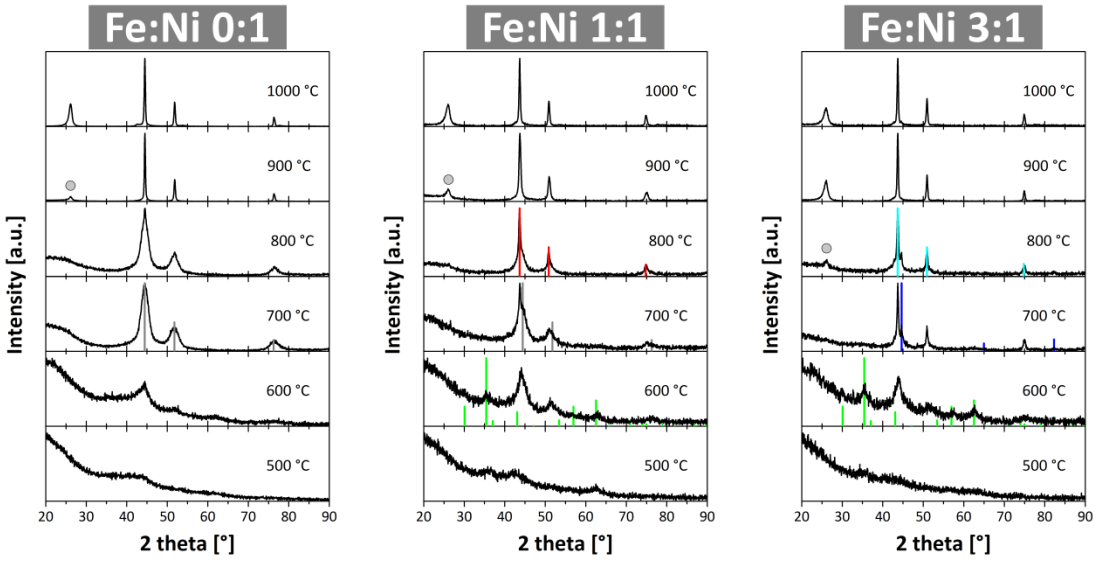

Figure 35: Summary of the temperature and ratio dependent XRD patterns for the nickel-iron system. The reference patterns marked are: Grey: Ni^0 (ICDD 04-010-6148), Red: $Ni_{0.5}Fe_{0.5}$ (ICDD 04-003-3531), Green: Fe_3O_4: (ICDD 04-015-3102), Blue: Fe^0 (ICDD 04-014-0360), Cyan: $Ni_{0.32}Fe_{0.68}$ (ICDD 04-002-1863) and the grey circle at 26° 2 theta is attributed to graphitic carbon (ICDD 04-015-2407). Larger prints of the patterns can be found in the appendix.

From the point of crystallisation at 700 °C and up to the onset of graphitisation at 900 °C the size of the Ni^0 nanoparticles is virtually invariant with temperature. For samples prepared at 800 °C the *Scherrer* equation yields particle sizes of (4.7 ± 0.3) nm. Upon graphitisation however the particle sizes increase dramatically; the cause of this are mechanisms similar to the ones that were observed with iron, as will be shown in the course this section.

The addition of moderate amounts of iron first causes the formation of a Fe_3O_4 phase at temperatures of 500 and 600 °C additionally from 600 °C on the alloy NiFe is formed alongside Ni^0. The alloy particles have a size of (4.4 ± 0.5) nm according to the *Scherrer* equation. With the onset of graphitisation at 900 °C the Ni^0 phase disappears completely and only graphitic carbon and the alloy remain. Adding a threefold excess of iron causes a similar reaction path, just that now Fe^0 is the excess phase and the alloy is the 3:1 alloy $Ni_{0.32}Fe_{0.68}$.

Interestingly nickel causes the formation of micrometre pores akin to the ones seen with manganese in the previous chapter. The addition of iron however immediately suppresses those larger pores, as was observed with manganese. The overall structural evolution was monitored using SEM and is summarised from 800 °C on in **Figure 36**.

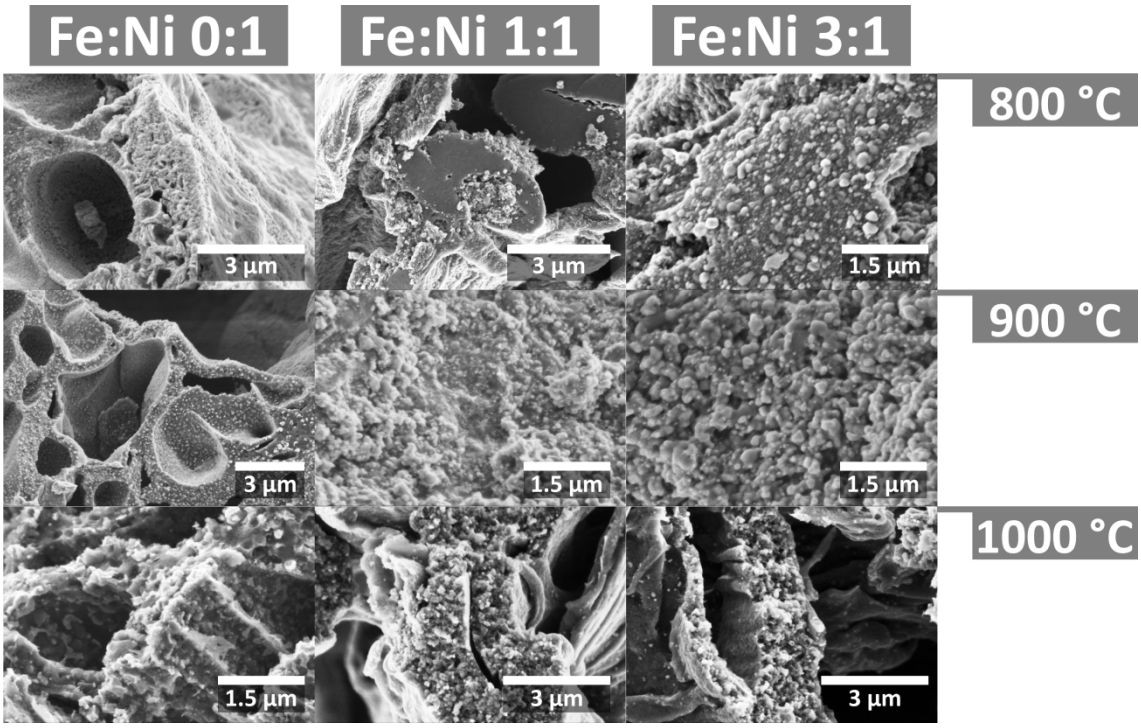

Figure 36: SEM summary figure covering all Fe:Ni ratios probed at temperatures from 800 to 1000 °C.

The large pores caused by nickel are observed over the full temperature range. With the onset of graphitisation the walls of the large pores become porous

themselves thereby effectively creating well-defined hierarchical pore structures ideal for applications in catalysis.[72] Samples prepared with iron and nickel do not show porosity until graphitisation sets in; the then formed pores are very similar to the structures presented in chapter three. The presence of iron does however cause the formation of a layer of nanoparticles on the surface of the fibres.

Table 3: Comparison of the apparent BET surface areas of samples prepared with different metal ratios at 800 °C.

Ni:Fe Ratio \ Temperature	800 °C $SA_{BET, app.}$ [m^2/g]
1 : 0	281
1 : 1	378
1 : 3	341

At the early stages of the reaction, this even appears to outweigh the micrometre pores in the formation of overall surface area as was determined by nitrogen sorption measurements (**Table 3**).

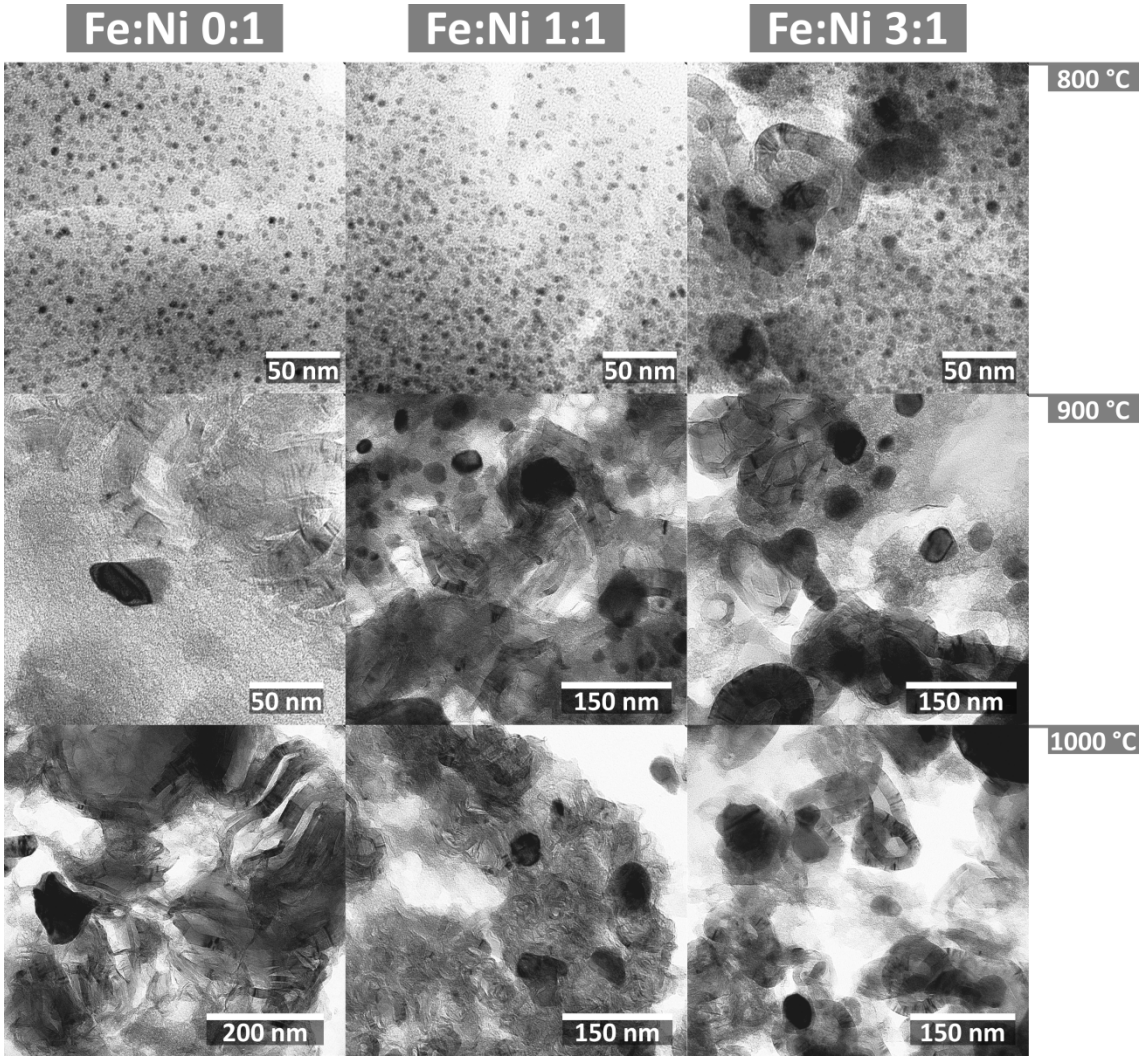

Figure 37: TEM micrographs covering the temperature range of 800 to 1000 °C for all three iron nickel ratios.

To further investigate the composites on the nm scale TEM micrographs of ultramicrotomed samples were taken. They depicted nickel and iron-nickel alloy nanoparticles of extraordinary quality (**Figure 37** and **Figure 38**). From the TEM images at 800 °C histograms of the Ni^0 and FeNi nanoparticles were derived and yielded particle sizes of (5.5 ± 0.5) nm and (5.3 ± 0.5) nm respectively (**Figure 38**).

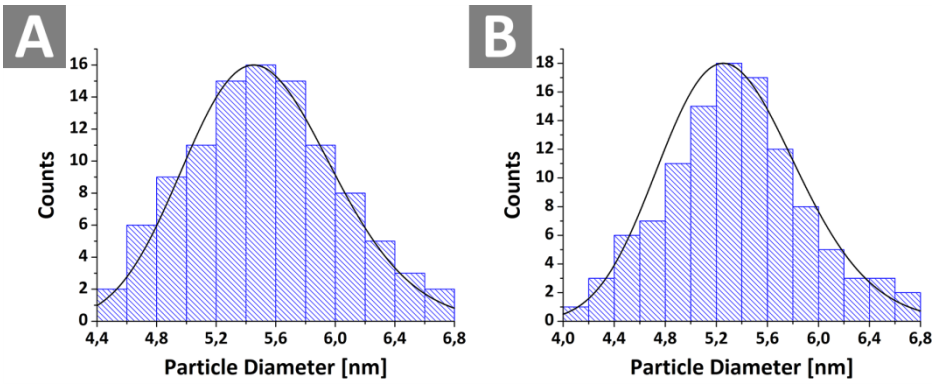

Figure 38: Histograms derived from TEM micrographs from samples prepared at 800 °C. Black curves represent lognormal fits to the histograms. **A**: Fe:Ni 0:1. **B**: Fe:Ni 1:1.

Either of the results goes well with the crystallite sizes determined *via* the *Scherrer* equation suggesting that they are in fact single crystalline particles.

Also at 1000 °C it becomes apparent that the graphitised carbon structures derived from nickel are of a more layered nature, meaning that they form flat aligned bundles as opposed to the rather tubular structures derived from iron. The transition from one structure to the other can be followed with increasing iron to nickel ratio.

TEM images depicted another process that lends a hand in explaining the phase behaviour observed in XRD patterns. Micrographs of samples prepared at 800 °C with an iron to nickel ratio of 3 to 1 show that the iron still forms on the surface of the fibres and only upon etching into the fibres does it come in contact with the nickel (**Figure 39**).

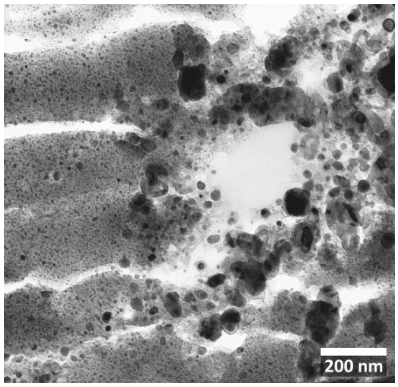

Figure 39: TEM image depicting the iron etching into the nickel containing carbon framework. The sample was prepared at 800 °C.

This explains why the alloy does not become phase pure until the graphitisation has fully set in. Iron behaves differently from all the other metals, in that regard that it forms oxides solely on the fibres surface and does not enter into the carbon matrix, until it forms the iron-carbon eutectic. An explanation for this observation could not be found. The most probable reason for this behaviour is a coordination effect where iron does not bind strongly enough to the cellulose matrix; there is, however, no prove for this. This effect appears to be similar to what was found with tungsten (see page 28).

Since the nickel nanoparticles are of very high quality preliminary tests were performed to answer the question whether or not they could easily be removed from the stabilising matrix and be obtained in the form of a stable dispersion. For this the as-prepared samples were put into glass vials containing a solution of oleic acid in toluene and submersed in an ultrasonic bath for 24 h (**Figure 40**).

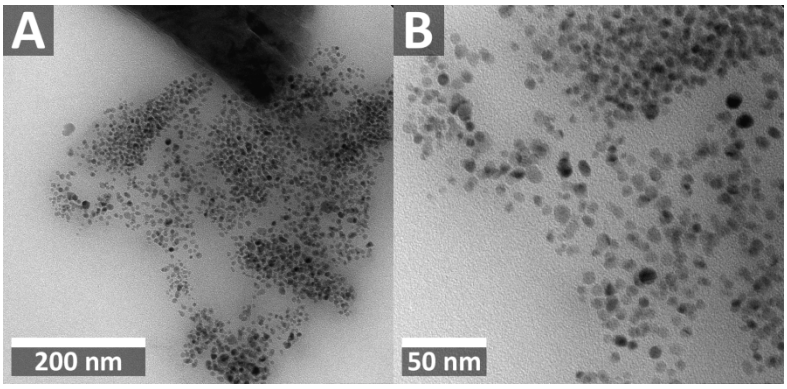

Figure 40: Nickel nanoparticles prepared at 700 °C and dispersed in toluene with the help of oleic acid.

Dispersing the nanoparticles by this method worked and is a promising starting point for further optimisation of the procedure. Even though this first attempt produced dispersed Ni^0 particles in substantial amounts, it has a few shortcomings. For one, still not all of the particles are dispersed as TEM also shows carbon fragments of a few µm full of nanoparticles. There furthermore appears to be some coalescence during the process, likely due to the harsh conditions in a 24 h ultrasonic treatment. Further improvements, namely in the form of more suitable solvents and dispersing agents, will likely enable the use of shorter dispersing times and thus help keeping coalescence to a minimum if not suppress it fully.

Spurred by these encouraging results first test to prepare another high value catalyst was performed and showed that the system can well be expanded beyond iron and its alloys to more noble metals. For this NiPd particles have successfully been prepared (**Figure 41**).

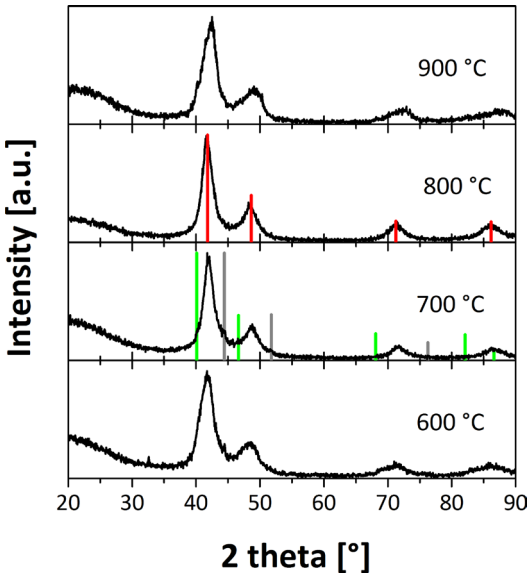

Figure 41: Temperature dependent XRD patterns of Ni Pd 1:1 prepared at temperatures form 600 to 900 °C. The reference patterns marked are: Black: Ni^0 (ICDD 04-010-6148), Green: Pd^0 (ICDD 00-005-0681) and Red: $Ni_{0.5}Pd_{0.5}$ (ICDD 04-001-3174).

The resulting alloy nanoparticles are, within the reaction parameters probed, practically unaffected by temperature (**Table 4**).

Table 4: Crystallite sizes derived from *Scherrer* equation for NiPd alloy particles.

Temperature	Crystallite Size from *Scherrer* equation [nm]
600 °C	(2.0 ± 0.2) nm
700 °C	(3.2 ± 0.5) nm
800 °C	(3.3 ± 0.2) nm
900 °C	(2.0 ± 0.2) nm

There is furthermore no trace of graphitisation visible, which is likely due to the apparently very stable nature of the alloy.

Summary

Pure nickel and alloyed iron-nickel and palladium-nickel nanoparticles of high quality have been produced. The cellulose matrix stabilised well separated monodisperse 5 nm nanoparticles of each metal or alloy, thereby again proving to be a very versatile stabilisation matrix. The particle size is virtually invariant to temperature below the graphitisation threshold, increasing the temperature above it (slightly above 800 °C) caused the particles to coalesce and graphitise the carbon matrix.

This investigation furthermore gave the intriguing result that nickel and iron seem to interact differently with cellulose. While iron forms particles on the surface of

the fibres, nickel does so directly within the fibres. In TEM this was especially observed when an excess of iron was employed. Also, XRD supports this, as at temperatures of 700 °C and 800 °C two crystalline fractions are visible, that merge to one when heating further. Interestingly samples prepared with a 1:1 metal ratio produced Ni as the excess phase and samples prepared with a 3:1 ratio produced Fe.

Lastly, attempts to separate the nickel nanoparticles from the carbon matrix and stabilise them in solution through ultra-sonic treatment have been made; the first results of this are promising.

COBALT-IRON-SYSTEM

This section will cover the last multi-metal system investigated in the work at hand and provide a synthetic strategy to the production of small Co^0 and CoFe nanoparticles with a narrow size distribution and high stability against oxidation. Further increase in iron content will yield equally stable larger nanoparticles comprised of the alloy Co_3Fe_7. Lastly, the formation mechanism of the previously observed µm pores will be discussed and moderate means of pore size control will be established.

Cobalt and iron presented a unique opportunity insofar that – as opposed to the previously investigated systems – here the alloy is formed immediately and no phase changes are observed with any of the systems as soon as the preceding oxide phases are reduced to elemental metals. The lack of phase changes allows for the investigation of different aspects of the product formation while ruling out phase transitions as a cause for them. This enabled for example to study the origins of the µm pores observed when a cobalt precursor salt was used. Furthermore was this the only system were the µm pores did not cease to form upon the addition of iron.

Firstly the observed phases a summarised again in a collective XRD patterns plot (**Figure 42**).

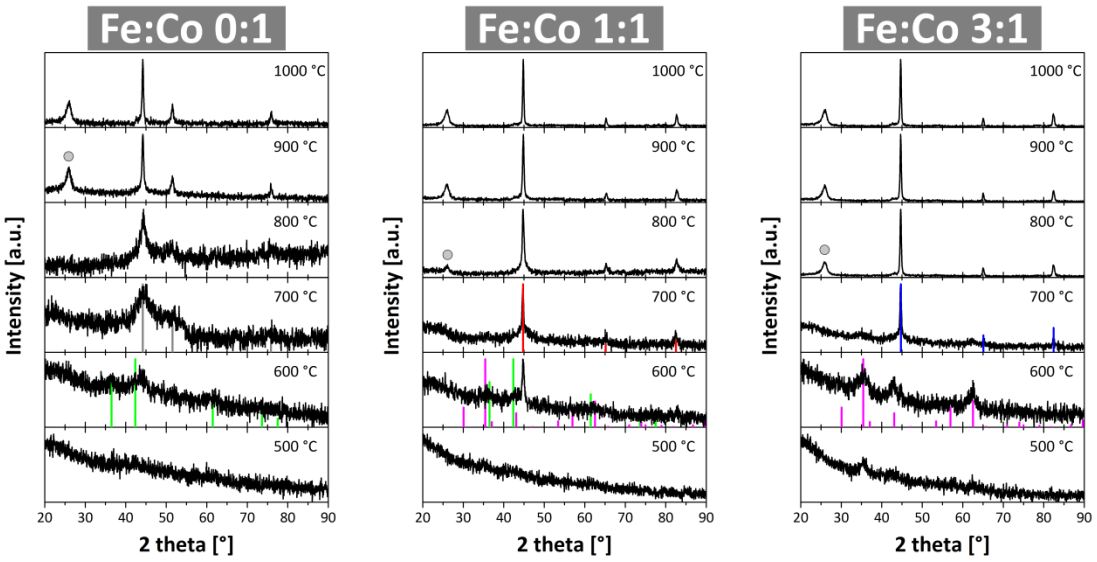

Figure 42: XRD patterns summary for the cobalt-iron system. The reference patterns marked are: Grey: Co^0 (ICDD 00-015-0806), Green: CoO (ICDD 01-071-1178), Red: CoFe (ICDD 04-014-0310), Magenta: Fe_3O_4 (ICDD 04-015-3102), Blue: Co_3Fe_7 (ICDD 00-048-1817) and the grey circle at 26° 2 theta is attributed to graphitic carbon (ICDD 04-015-2407). Larger prints of the patterns can be found in the appendix.

Each metal is first present in the form of its respective oxide until reductive processes set in at 600 °C. Cobalt appears to be reduced to elemental metal at slightly lower temperatures than iron as Co^0 and FeCo are seen at 600 °C, but at this temperature for the sample with a 3:1 ratio there are mere hints to an elemental alloy phase. Additionally for this ratio traces of the oxide phase persist up to 700 °C. Cobalt will cause graphitisation of the carbon matrix at 900 °C. In combination with iron, it does, however, not appear to greatly hinder the formation of graphitic carbon as it now is produced at 800 °C – the same temperature that was observed with purely iron based samples.

Morphologically, the cobalt-iron system is very similar to the nickel based system, since cobalt alone also gives rise to large amounts of µm sized pores. The porous matrix also becomes a hierarchical structure at high temperatures when graphitisation processes add a second mesopore fraction effectively yielding pores whose walls are porous. Nevertheless it also does present an important novelty as here the presence of the large pores is impeded but not fully supressed by the addition of iron; a detail that will be of importance towards the end of this section where mechanisms governing the porosity are discussed (page 61). The structural changes that the composites undergo can be followed *via* SEM imagery (**Figure 43**).

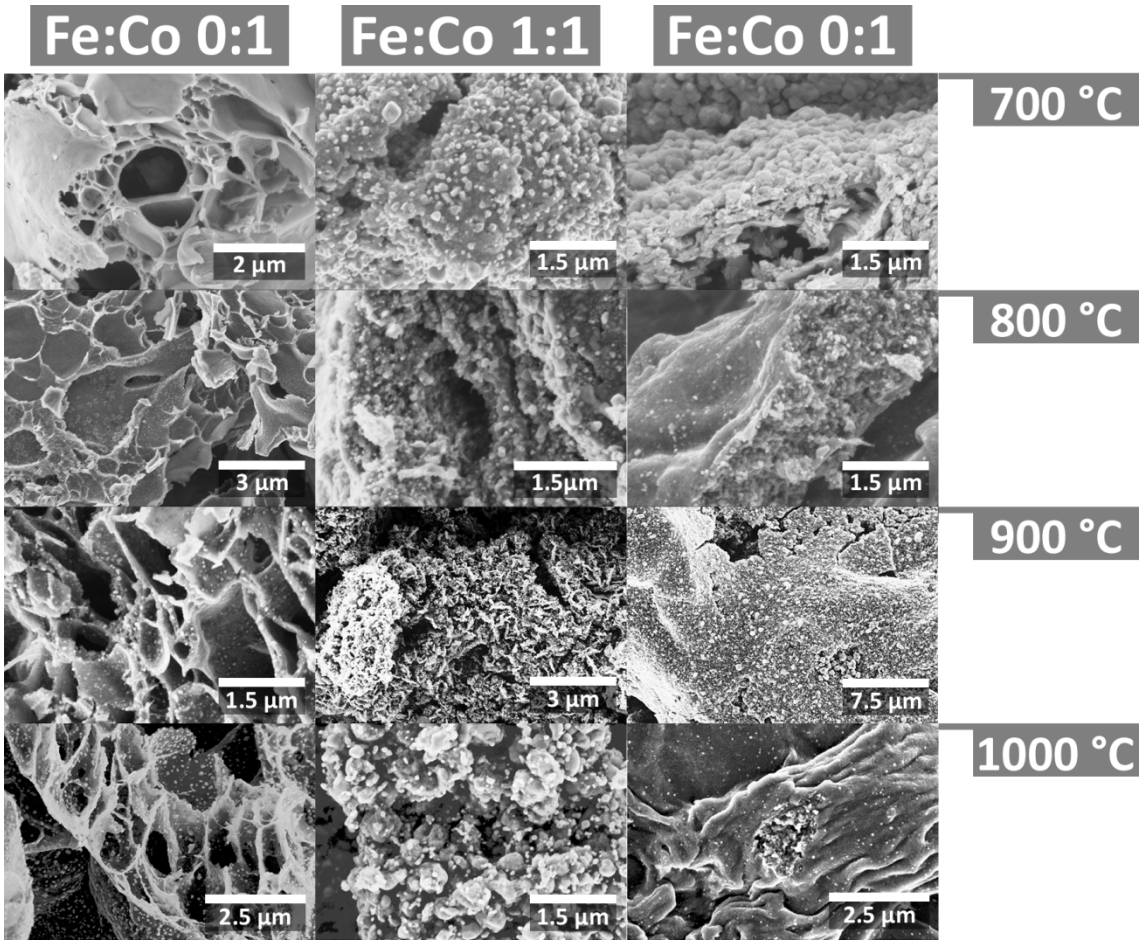

Figure 43: Structural developments of the cobalt-iron systems monitored with SEM.

The mixed metal samples present mesopores, caused by the graphitisation of the cellulose, from 800 °C onward. The surface of the carbon becomes covered with cobalt nanoparticles that are detectable in SEM once graphitisation and hence coalescence of the particles sets in. In the binary systems, particles are visible throughout the full temperature range, a result of the surface coalescence already discussed in the copper section (page 44). This observation is supported by XRD patterns, which suggest larger crystallites from 700 °C on. To image the smaller crystallites that form at lower temperatures, TEM micrographs of the Co^0 nanoparticles produced at 700 °C were taken (**Figure 44**) and a full TEM investigation for all samples at higher temperatures was performed as well (**Figure 46**).

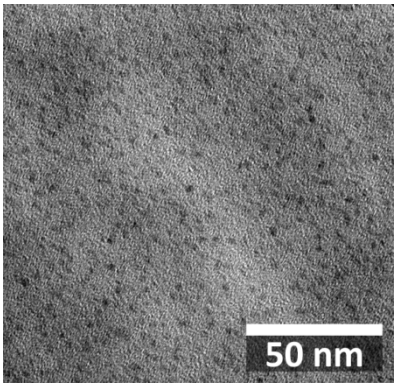

Figure 44: TEM micrograph of Co^0 nanoparticles produced at 700 °C.

The Co^0 clusters obtained from samples heated to 700 °C are very small, as XRD already suggested. They are in fact so small that a size evaluation from TEM with reasonable accuracy is not possible. They are however well separated, dispersed throughout the carbon framework and appear to be of sizes smaller than 2 nm. This would be in full agreement with the 2 nm crystallite sizes derived from the *Scherrer* equation. Heating the cobalt samples further causes some degree of coalescence, so that the particle sizes can properly be evaluated from TEM micrographs (**Figure 45**).

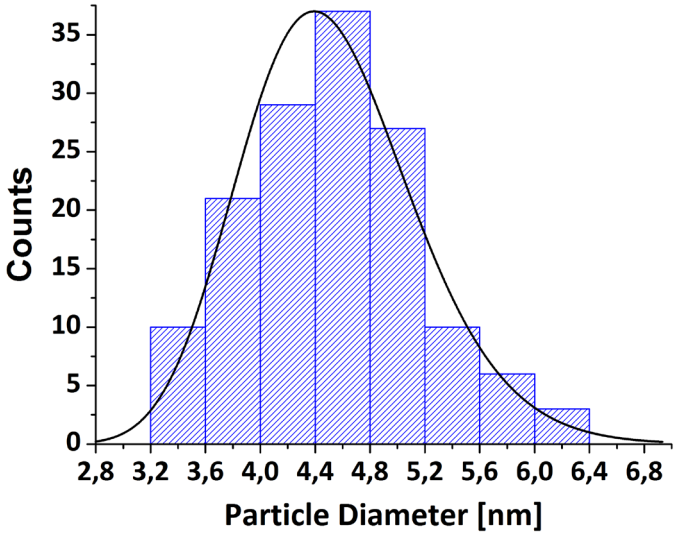

Figure 45: Histogram derived from TEM micrographs of Co^0 particles prepared at 800 °C. The black curve represents a lognormal fit to the histogram.

This evaluation yielded a mean size of (4.5 ± 0.6) nm and coincides well with the value that results from the *Scherrer* equation (4.4 nm), which indicates that the particles are mostly single crystalline and have little to no defects.

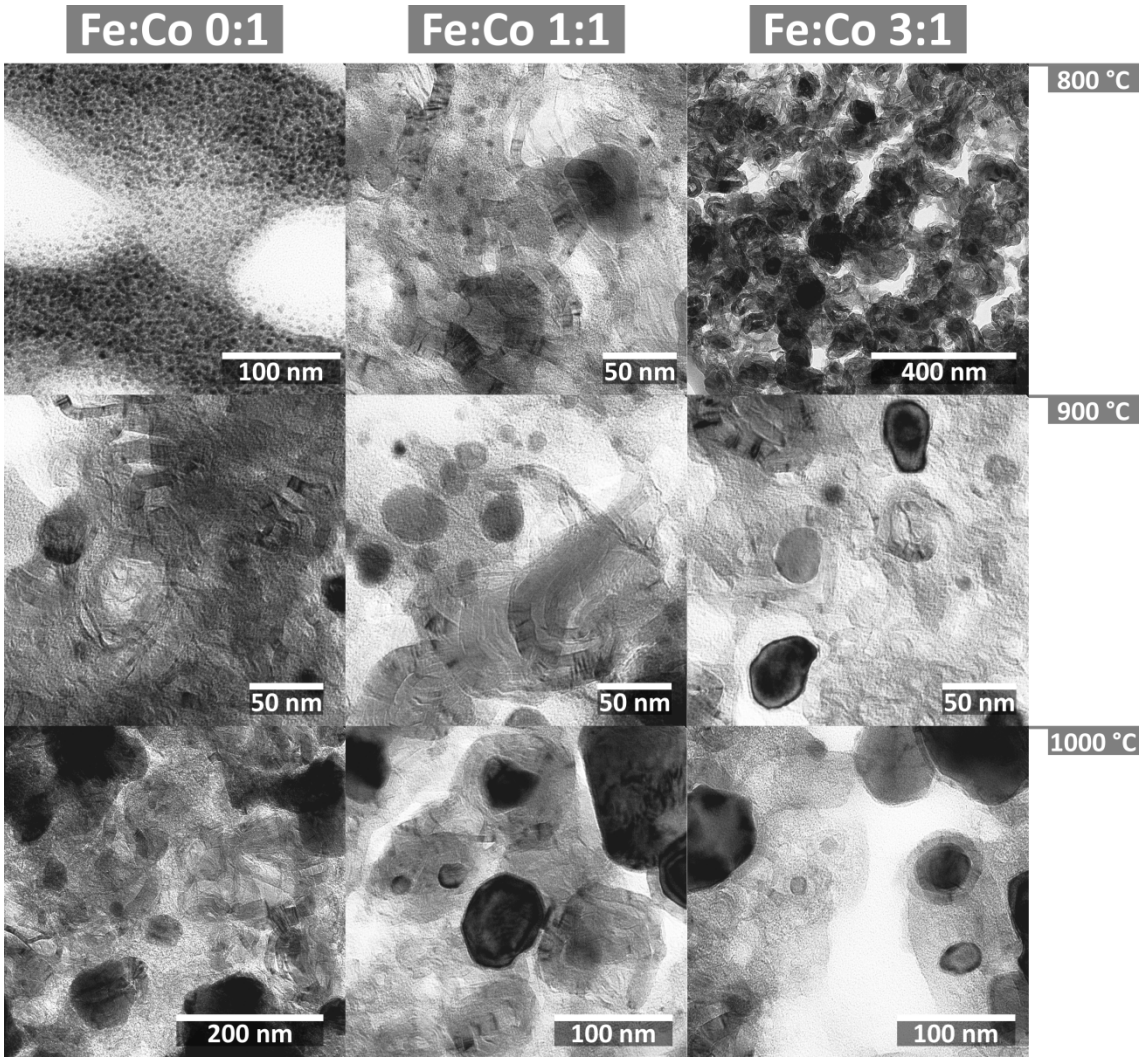

Figure 46: TEM study of the cobalt and cobalt-iron samples.

Once graphitisation sets in, the resulting composites become, on first glance, indistinguishable from products obtained with iron. There is however one noticeable difference: where iron carbide nanoparticles always possess a thick carbon shell it is never seen with cobalt and remains a rare exception with the 3:1 mixed metal samples. This suggests that with cobalt the intermediate state is not a liquid eutectic, but graphitisation happens rather *via* surface catalysis on the cobalt or cobalt-iron alloy nanoparticles. In the literature this effect has, at least for pure cobalt, been attributed to the initially larger crystallites of cobalt and its oxides, which do not fully transform into a liquid state.[30] This is however not supported by the observations in the work at hand where the cobalt oxides are of the same size if not smaller than the iron oxides. The lager crystal size can hence not be the cause for this, but the conclusion of a purely surface driven catalysis step is still a valid assumption. This also explains well why elemental cobalt and its alloys are formed rather than the corresponding carbides.

Controlling the Porosity

Nanohybrids resulting from the high temperature treatment of cellulose and cobalt possessed very large mass transport pores, not unlike the ones already seen with manganese or the ones that will be shown to result from nickel treated samples later in this chapter. Initially the stark variation in pore sizes between different metals was attributed to different –possibly multistep – graphitisation mechanisms. This was based on the fact that with increasing temperature the porosity shifted to smaller pores and the surface area decreased (see **Table 5** for an overview).

Table 5: Summary of the apparent BET surface areas ($SA_{BET, app.}$) obtained from the various Co/Fe systems.

Temperature / Co:Fe Ratio	700 °C $SA_{BET, app.}$ [m^2/g]	800 °C $SA_{BET, app.}$ [m^2/g]	900 °C $SA_{BET, app.}$ [m^2/g]	1000 °C $SA_{BET, app.}$ [m^2/g]
1 : 0	--	359	225	180
1 : 1	459	369	205	172
1 : 3	--	228	224	212

However, when attempts to control the porosity *via* mixing of different metals failed, the search for the cause of this revealed that drying the samples prior to carbonisation will fully suppress the formation of large pores. Then only the meso- and small macropores stemming from the graphitisation and subsequent formation of tubular pores are observed (**Figure 47**).

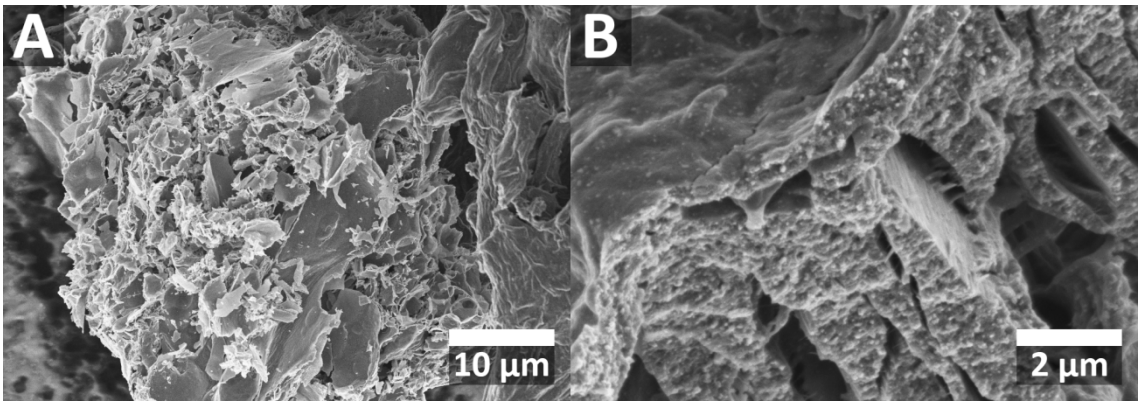

Figure 47: **A**: When the samples are calcined while still wet it produces large µm pores. **B**: If the samples are dried before calcination only small pores due to the tubular carbons that form upon graphitisation are visible.

Due to this observation the attempts to control the large porosity were shifted to pre-drying the samples for various durations to yield different porosities. The first question to be answered was whether the transition from the large to the small porosity happens *via* shrinkage of the large pores or if the number of pores decreases while their size stays the same.

Pre-drying of the samples at 50 °C in air showed that the larger pores do not shrink significantly; they merely become less and less common within the samples until no trace of them can be found anymore (**Figure 48**).

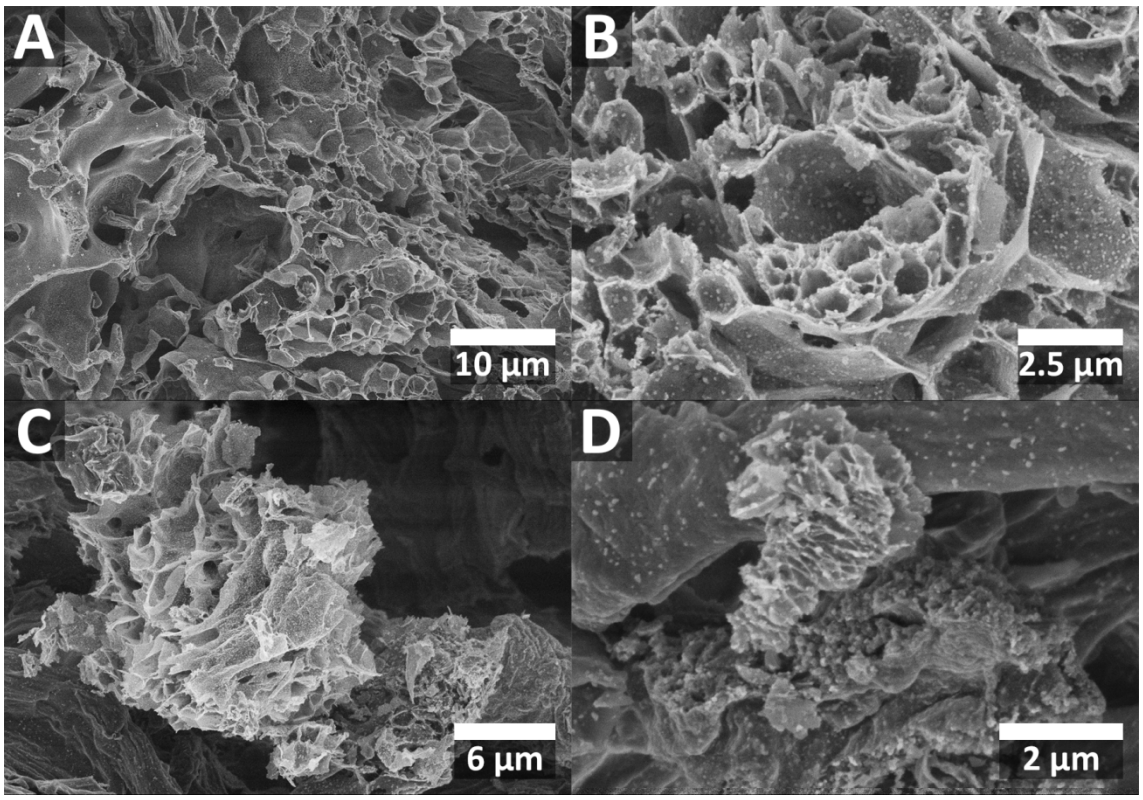

Figure 48: **A**: Drying time 0 min. **B**: Drying time 15 min. **C**: Drying time 30 min. **D**: Drying time 45 min

Repeating this experiment several times showed, nevertheless, that this mean of control is very sensitive to any type of perturbation and careful control of environmental parameters, especially of the humidity, has to be exerted. In some cases the samples would show no micrometre pores after 45 min of drying and other times they would. Similarly the micrometre porosity was not homogeneously distributed within the samples, there were areas trenched densely with large pores while others would have none at all.

This raises of course the question as to what is causing this behaviour. With iron, copper and tungsten – alone or in combination – micrometre pores were never observed, no matter if they were calcined with all the water still in the samples of fully dried. For iron alone this was even confirmed with several different counter ions and oxidation states of the iron. In contrast manganese, cobalt and nickel are very prone to form them when not pre-dried. The most probable reason is that the pores are formed as the result of a gas expansion reaction that takes place at higher temperatures where the carbon framework already starts to fixate so that the pores do not simply collapse again. In order to illuminate this question further TGA/MS was conducted on a pre-dried and a fresh (still wet) sample of cobalt nitrate with cellulose.

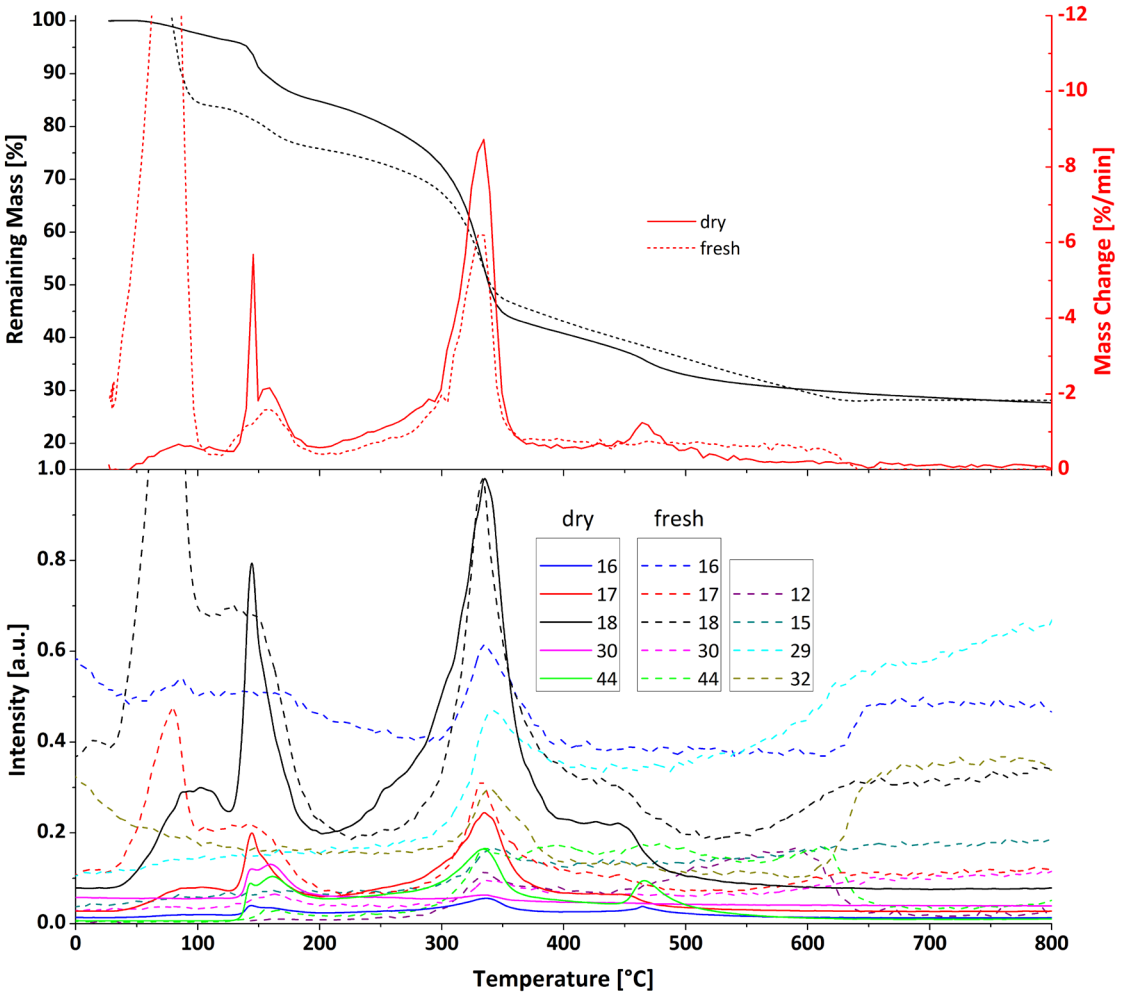

Figure 49: TGA MS Measurements of micro crystalline cellulose soaked with an aqueous $Co(NO_3)_2$ solution. The pre-dried sample is represented by solid lines and the fresh on by dashed lines. **Top**: TGA traces for both samples. **Bottom**: MS traces for both samples. The masses m/z 14 and 28 have been ommitted since the carrier gas is nitrogen.

The TGA/MS spectra were normalized to account for the great difference in measured sample mass and water content (60 wt%). The main thermal decomposition of cellulose is apparently not effected by the pre-drying of the samples. Aside from this the two samples behave astonishingly different. The dry sample shows 4 distinct signals (excluding a small initial loss of water) in TGA that are all well mirrored in the MS spectra. The first is an overlapped signal with a very sharp one at 146 °C and a broader one between 133 and 187 °C. Here the broad one is attributed to a loss of water bound more strongly in the cellulose framework and the sharp signal is attributed to the first decomposition of the cobalt nitrate. The large drop at 334 °C is the decomposition of the cellulose. The last signal at 465 °C is caused by the reduction of the cobalt to form the cobalt nanoparticles – this matter will be discussed in the remainder of this chapter. After this signal the sample does not seem to change anymore. In contrast to this the sample still containing the water shows quite a

different picture. The broad peaks at approximately 160 °C and 334 °C – both attributed to cellulose – are present and are of similar intensity, whereas the sharp peak at 146 °C is lacking completely. Instead there is a constant mass loss after the initial cellulose decomposition that lasts until about 650 °C at around which the release of gaseous components is even increased according to the MS spectra. The reason for this is very likely the tendency of nitrates to form hydrate melts that behave quite unpredictable.[88-89] Research into this has been conducted by several groups, none of which have succeeded in explaining the behaviour observed with metal nitrate hydrates.[88, 90] The explanation as to why this is not observed when iron precursors are used is likely due to the fact that iron – as opposed to the other metal precursors – does not seem to enter the cellulose and thus, even if it behaves differently, it would not affect the morphology of the cellulose.

In conclusion the porosity can be controlled by pre-drying the samples for some time. This is however a very tricky task and would likely work better in an environment with a fully controlled atmosphere – especially the humidity – to ensure reproducible drying behaviour every time. This would however defy the purpose of having an easy way of controlling the porosity.

It was already suggested at the beginning of this section that there is also a way of controlling the porosity *via* the mixing of two metals, namely iron and cobalt (**Figure 50**).

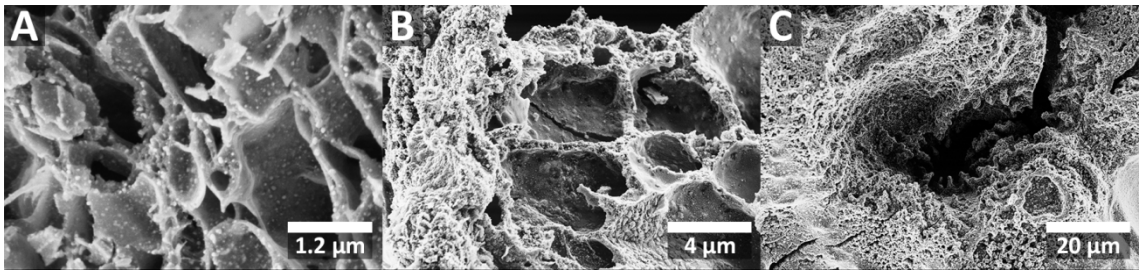

Figure 50: Porosity control via the addition of iron. All samples were prepared at 900 °C. **A**: pure Co. **B**: Co:Fe 1:1. **C**: Co:Fe 1:3.

By using fresh, wet samples the ratio of cobalt to iron will alter the ratio of large to small pores, as iron will always only form mesopores. This approach may prove to be an easier way of controlling the porosity, but this remains open to further investigation.

Summary

In conclusion the use of cobalt salts and cellulose can yield cobalt nanoparticles of < 2 to 5 nm dispersed in amorphous carbon. Increasing the reaction temperature above 900 °C brings about larger cobalt nanoparticles and broadens the size distribution but also graphitises the matrix and thus embedding them in a fully

conductive, self-standing framework. The addition of iron results in particles of the same morphology, but, depending on the metal ratio CoFe or Co_3Fe_7 alloys are obtained. Each of the probed reactions resulted in phase pure, stable materials. Lastly some preliminary tests to control the porosity obtained with these systems have been made. Control *via* a pre-drying step as well via the alloying ratio appears to be possible with reasonable accuracy. But especially the reasons and mechanisms for the formation of large mass transport pores in the carbon scaffold are not yet fully understood and should be investigated further to enable prediction of the porosities obtained.

In general an easy and fast one-pot synthesis for obtaining cobalt and cobalt-iron alloy nanoparticles has been presented allowing for the tailoring of the alloy ratio as well as control of the substrate – conductive graphitised carbon or amorphous carbon as a separating agent.

VI. Structuring and Patterning

Introduction

The ability to exert control over the structure of a product is in many cases most crucial to making a compound applicable at all. A good example for this is that some materials, such as gold, will only show catalytic activity when present in the form of nanoparticles. Structuring is in itself a very broad term, that can mean anything from full 3D shape determination on the centimetre scale to ordering on a nanoparticle level.

Analogous to the bottom-up and top-down approaches that are known from nanotechnology, structuring methods are either additive, meaning that components are added together until the desired structure is attained, or subtractive, in the sense that parts are taken away until the desired shaped is reached. Aside from those two shape-determining purports, structuring is also often associated with any form of patterning. Meaning that not the actual shape of a product is altered but rather parts – or all of it – are altered on a compositional level, much like a paper does not change its shape when it is printed upon but rather it is patterned in a desired fashion.

One of the outstanding features of cellulose is that it is well suited for several ways of structuring. From ancient casting and pressing methods such as the ones used to make paper, to folding techniques such as the traditional Japanese paper folding art Origami, to the only recently developed rapid prototyping methods employed to create virtually any 3D shape. Lastly starting out from solid pieces of wood rather than pure cellulose fibres computer numerical control (CNC) milling is a well-established technique for structuring work-pieces with high precision. Aside from these shaping techniques there is of course also any form of printing or writing that enables patterning of cellulose based structures.

In this chapter structuring and straight forward patterning methods will be shown to yield very promising results and highly functional products. To exemplify the three dimensional shape retention capabilities of iron cellulose composites the art of Origami has been chosen as it is not just aesthetically pleasing, but arguably also comprises some of the most complex structures obtainable from flat paper. Furthermore ink-jet printing has been chosen as a patterning technique because it is very precise, well established, and cheap and it simply presented a logical choice for processing liquid precursors in combination with paper.

In addition to patterning the functional nature of the nano-composites will be underlined by the use of cellulose paper as free standing electrodes – patterned and un-patterned – and the subsequent selective electro-deposition of a copper coating

onto the printed areas of a specimen as well as the presentation of the synthesis of electrodes that are not only patterned but also remain fully flexible after high temperature treatment.

FREESTANDING ORIGAMI ELECTRODES

That the composites exhibit a very high degree of shape retention on the micrometer (and larger) scale has already been shown in the previous chapters. To establish whether this is also true for more complex shapes Origami figures, such as the well-known crane, were prepared. The risk here was that folding the paper prior to the high temperature treatment may result in breakage of the samples due to the shrinkage of the specimens. For this the folded cranes were submersed in the iron precursor solution and calcined under inert atmosphere (**Figure 51**).

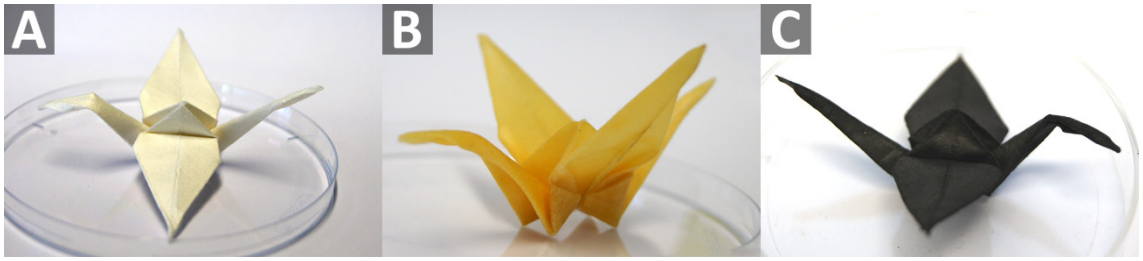

Figure 51: Steps leading to the magnetic cranes: folding (**A**), soaking with the precursor solution (**B**) and after calcination (**C**).

The resulting cranes were not only very well preserved in shape they were also highly magnetic and stable enough to be picked up by the wings or the beak (**Figure 52**).

Figure 52: The magnetic cranes are easily lifted up and kept afloat by a permanent magnet.

Once the remarkable shape retention was confirmed the applicability as an electrode needed to be confirmed. Hence, in a first proof of principle study, it was shown that the nano-composite of iron carbide resulting from the infusion of paper with an aqueous iron precursor solution and subsequent calcination could be used as a free-standing electrode. To show this, a piece of the composite was cut out, connected

to a 1.5 V battery and dipped into an aqueous 1 M copper(II) sulfate solution with a solid copper counter electrode (**Figure 53**).

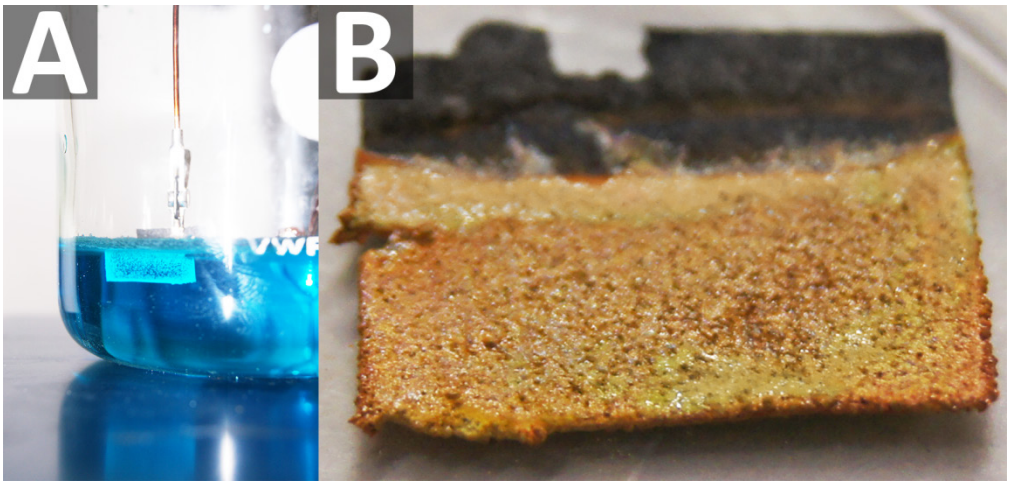

Figure 53: **A**: Photograph of the coating procedure. **B**: Fully copper coated electrode.

Combining those two ideas resulted in the successful attempt to coat more complex structures with copper (**Figure 54**).

Figure 54: Copper coated Origami crane.

This exemplifies that by this technique virtually any three dimensional shape can be turned into an electrode and even be post-processed to yield a further variety of highly functional materials.

All the aforementioned results have in common that they always functionalise the whole specimen, whether that be a flat piece of filter paper or an intricate Origami structure. The next logical step was to attempt to selectively functionalise the materials. Subsequently, experiments showing that the aqueous precursor solution could be filled into the cartridge of a fountain pen with the help of a syringe and that the cellulose could then be patterned by drawing onto it were successfully conducted (**Figure 55**).

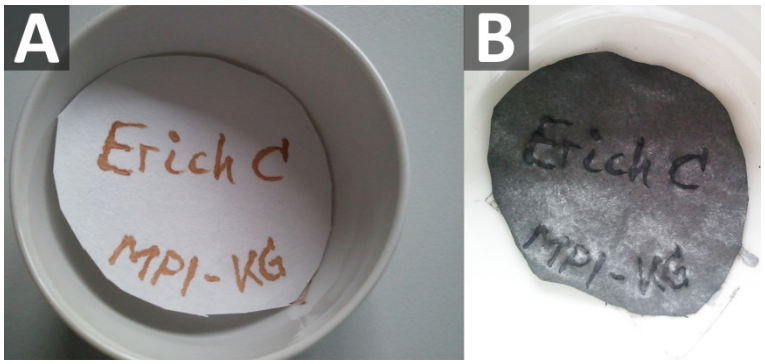

Figure 55: Filter paper that was patterned with a fountain pen before (**A**) and after calcination (**B**).

This, together with the finding that quartz plates can be employed to prevent wrinkling of the filter paper upon calcination, enabled the final step of the patterning experiments: the use of a commercial ink-jet printer to produce structured substrates.

INK-JET PRINTING

To keep the simplistic nature that is inherent to all the synthesis procedures presented in this work the only option for a printing device was a low-cost commercial printer that needed very little or preferably no modification in order to work with the aqueous precursor solutions. Initially several commercial printer models were tested, but since all of them worked well the least expensive and least complicated printer was picked for all the patterning experiments. This printer was an Epson™ Stylus S22, costing only 25 € (**Figure 56**).

Figure 56: The employed Epson™ Stylus S22with a refillable cartridge.

Initial tests were performed with the original cartridges that were delivered with the printers. For this they were emptied and cleaned thoroughly before being refilled with the metal salt solution. Once a printer was picked though a set of special refill-cartridges was used, the reason for this was ease of use; these cartridges have well lidded openings to quickly refill and empty them.

Synthesis

No alteration of the before used aqueous precursor solutions was needed to use them with the printers. However for faster visual assessment the concentration of the iron nitrate was increased fourfold to make it clearly visible directly after printing. Since the carbon is always present in large surplus the change in concentration had no impact on the overall product. A pattern was printed onto lab filter paper (the same that was used previously), which was mounted onto an A4 sheet with adhesive tape. The likeness of the roman goddess of wisdom Minerva was used as an example, since it fulfils several important prerequisites. Most importantly it is made from completely connected lines; secondly it features different line-thicknesses and straight as well as curved lines. Also, since it is a face, changes that might occur during calcination, such as uneven size changes, are easier perceived by the human eye and lastly it is of course the insignia of the Max Planck Society. After printing the paper was calcined under nitrogen atmosphere. During this it was placed between two quartz plates to keep it from wrinkling (**Figure 57**).

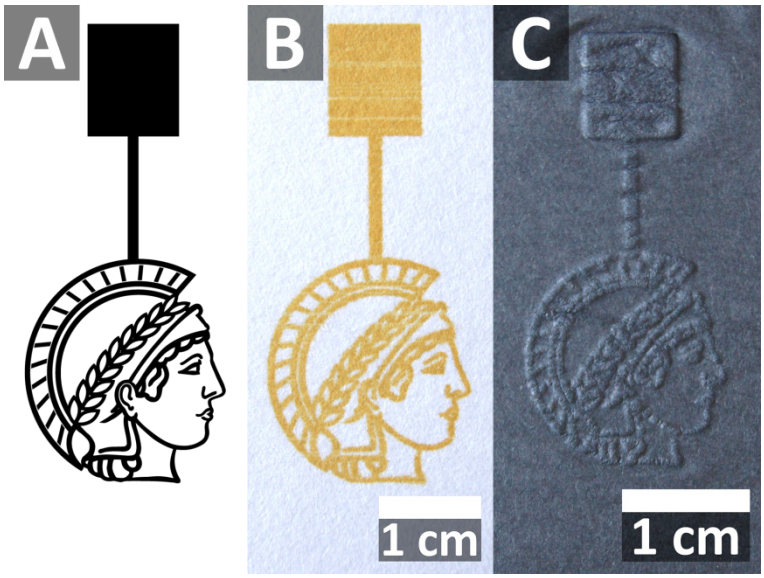

Figure 57: **A**: The design made with a computer program. **B**: The result of the printing. **C**: The resulting calcined structure.

Depending on the employed metal this usually yields graphitised carbon with embedded nano-particles in the printed areas surrounded by the non-printed areas consisting of amorphous carbon.

Synthesis in Confined Spaces

An experiment to verify that the use of quartz plates, which were employed to prevent wrinkling of the cellulose paper, did not change the products formed during calcination yielded the interesting result, that, by merely placing a quartz plate on top of the fibre mat, the degree of graphitisation is improved (**Figure 58**).

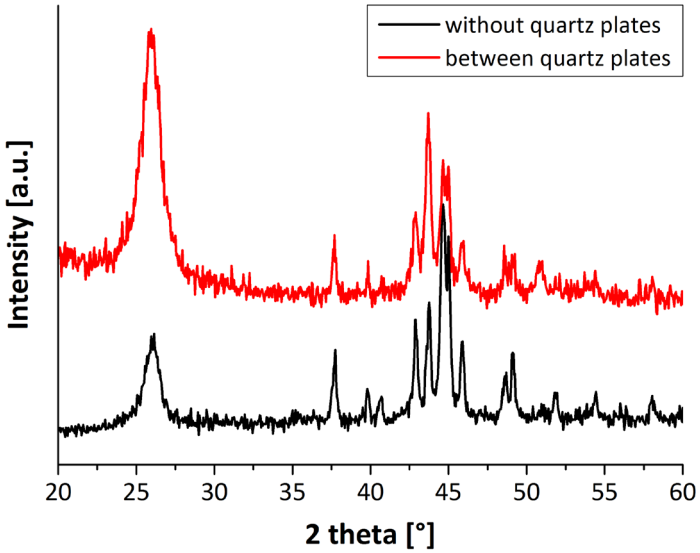

Figure 58: X-ray diffractograms comparing a sample that was calcined between quartz plates and one that was calcined without quartz plates.

The most reasonable explanation of this is that the confined space between the quartz plates virtually creates a mini-reactor, which reduces the local nitrogen flow and thereby hinders the removal of volatile products which are released during calcination.

Printing Quality

Due to the liquid intermediate state of the iron carbon eutectic the quality of the edges of the printed structures needed to be assessed. For this a typical reference pattern used to evaluate lens qualities in photography was printed out. As a first step the quality of the actual printed lines was evaluated via optical inspection (photography) and optical microscopy (**Figure 59**).

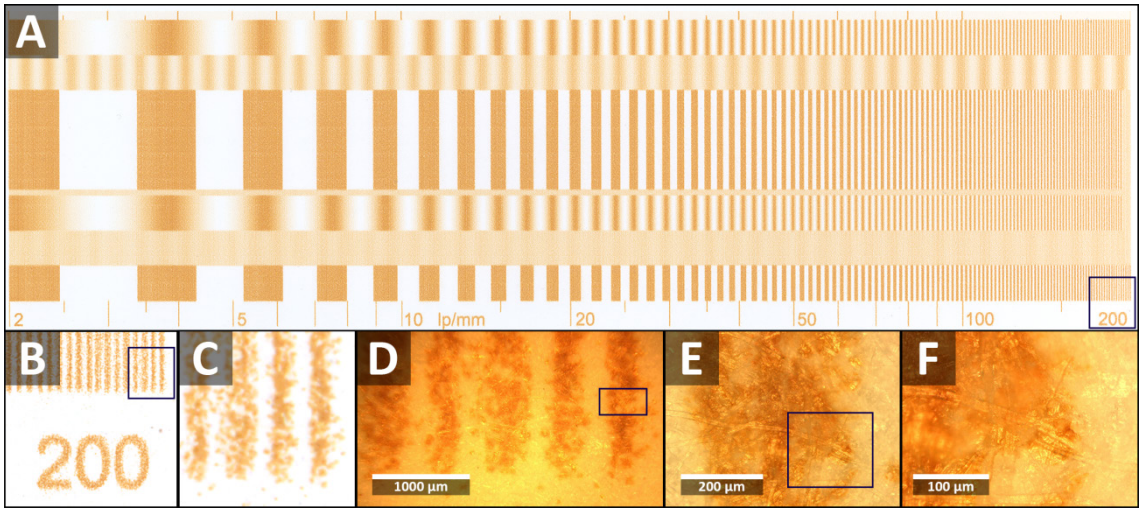

Figure 59: Visual assessment of the printing quality (**A-C**) and with the help of an optical microscope (**D-F**). The initial print was printed to the width of an A4 sheet. The blue boxes mark the areas enhanced in the next panel.

Despite the fact that no optimizations of ink or printing system were made the ink separate lines with thicknesses and spacing in the 100 µm range can readily be printed. Once calcined the quality does not change at all as can be seen from line EDX and elemental mapping of a printed line (**Figure 60**).

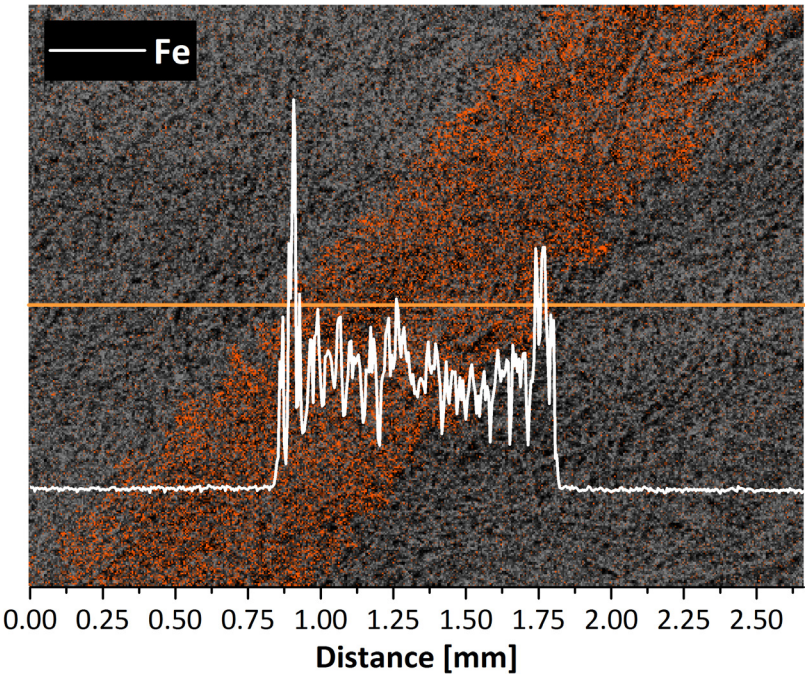

Figure 60: Line EDX for iron (white graph, taken along orange line) and elemental mapping for iron (orange).

Since EDX showed well defined edges of the printed lines UM was performed on a printed and calcined line in order to obtain TEM micrographs. Despite the high mobility of the iron-carbon eutectic droplets that was found in the *in-situ* TEM investigation the edges are also defined quite well in TEM. Outlying single particles have not been found further than a few hundred nanometres away from the edge of the printed pattern (**Figure 61**).

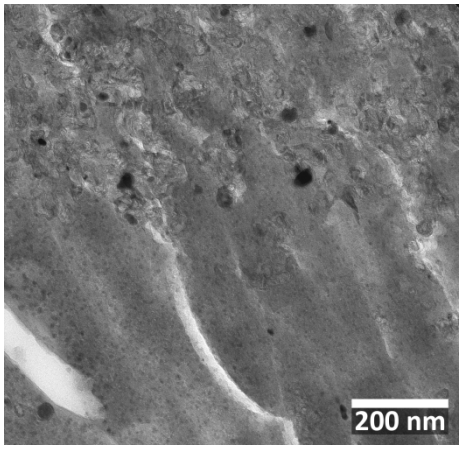

Figure 61: Ultramicrotomed sample of the edge of a printed and calcined line.

After the in-plane spread of the printed patterns was assessed the printing depth needed to be investigated as well. For this a printed area was cut in half and set up right onto a SEM sample holder. This showed that the ink actually does only enter the top most layers of the cellulose, usually no deeper than approximately 30 µm, equalling three layers of fibres (**Figure 62**).

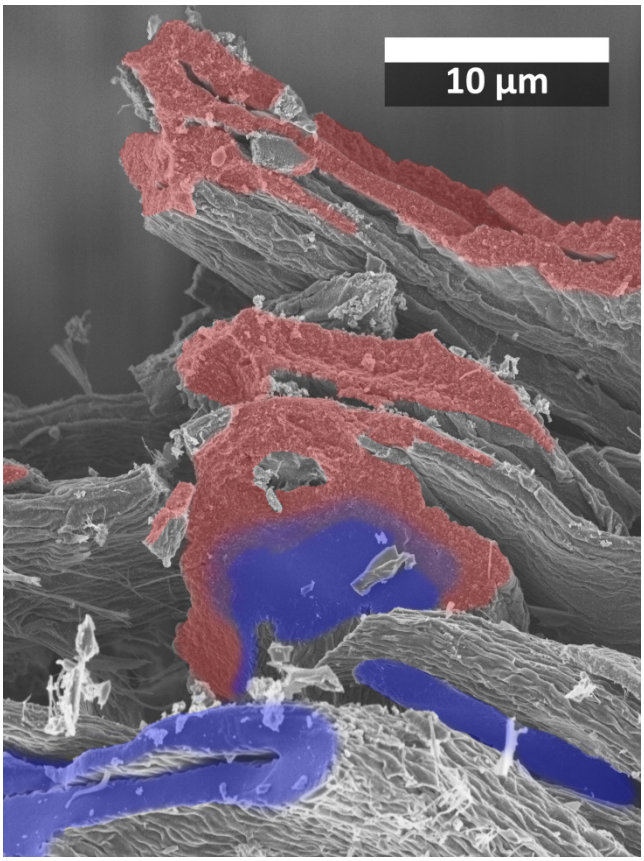

Figure 62: Cross-section of a printed filter paper after calcination. The left edge is the printed side. It is visible, that the graphitisation due to the presence of the iron ink only took place in the few upper layers of the paper (coloured in red), leaving the backside of the paper amorphous (coloured in blue) and none-conductive.

Patterned Electrodes

Once the printing was understood, it could be combined with the idea of applying a copper coating to further functionalize the products. To combine the two ideas the fact that the areas printed on with iron ink will graphitise, whereas the surrounding carbon stays mostly amorphous was exploited. The difference in carbon morphology causes a significant difference in conductivity between the two areas. This was used to selectively coat copper onto the more conductive (printed) areas. Since electro-deposition is a delicate art in itself, the copper deposition was performed at well controlled conditions using a potentiostat with a constant voltage of 0.3 V and a glass slide to provide a flat support for the printed electrode to ensure a fix distance between the two electrodes. The resulting coated electrodes (**Figure 63**) clearly show that copper deposition first and foremost happens where the iron ink was printed.

There is no stray deposition visible, only outgrowth from already deposited copper. This leaves other areas with only very thin lines of copper, since the copper then preferentially deposits where some copper is already present.

Figure 63: Photo of deposited copper on the printed Minerva structure. The resulting deposition is not flawless but can none the less serve as a proof-of-concept.

The issue of a somewhat uneven deposition can likely be overcome by finely tuning the deposition conditions as it is practiced in industrial applications. This process however is very time consuming and should be performed by specialists in the field of electro deposition.

Multi-Metal Printing

Utilizing the inherent capability of printers to print more than one ink – typically a printer is equipped with four cartridges, one for each shade of the CMYK colour system. This immediately brings about the idea to use the mixing possibilities that this system possess. Depending on make and model a commercial ink-jet printer can easily deliver several thousand different colours *via* high precision mixing of the four inks. Consequently this can be used to produce extremely fine metal gradients or very well defined fixed metal-metal ratios simply by picking a colour. As a preliminary test iron and cobalt inks have been deployed in a gradient covering the full phase diagram (on the ratio axis) of the two components (**Figure 64**).

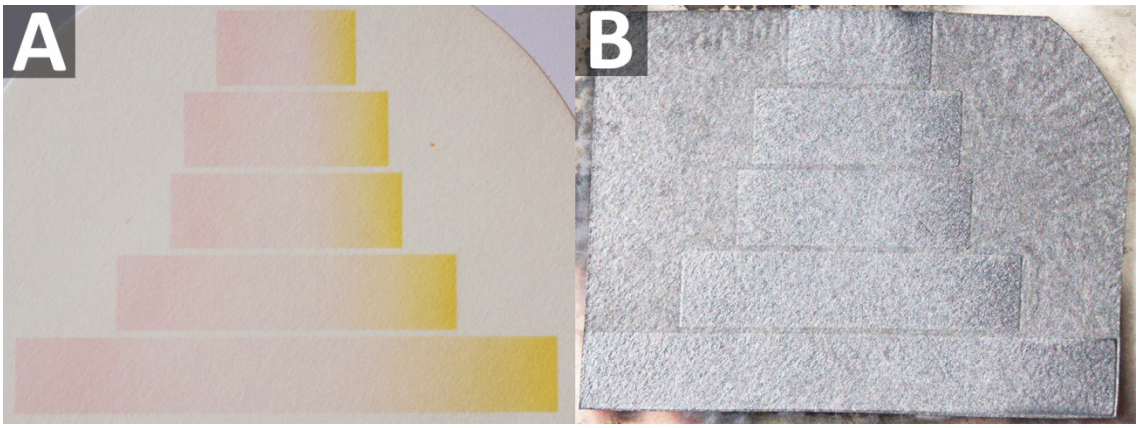

Figure 64: **A**: Printed gradients from a cobalt nitrate solution (pink) to an iron nitrate solution (yellow). **B**: The structure after calcination at 800 °C.

Repeating the experiment shown above at various temperatures could easily yield an actual phase diagram of the two components. But since these results thus far are only of a preliminary nature, the vast possibilities of this approach will be discussed at the end of this section.

Ultra-Thin Flexible Electrodes

By employing a different cellulose precursor, namely ultra-thin paper from single tissue layers, the resulting composite retained the very good flexibility of paper after the calcination step yet it could still be patterned with the help of an ink-jet printer (**Figure 65**).

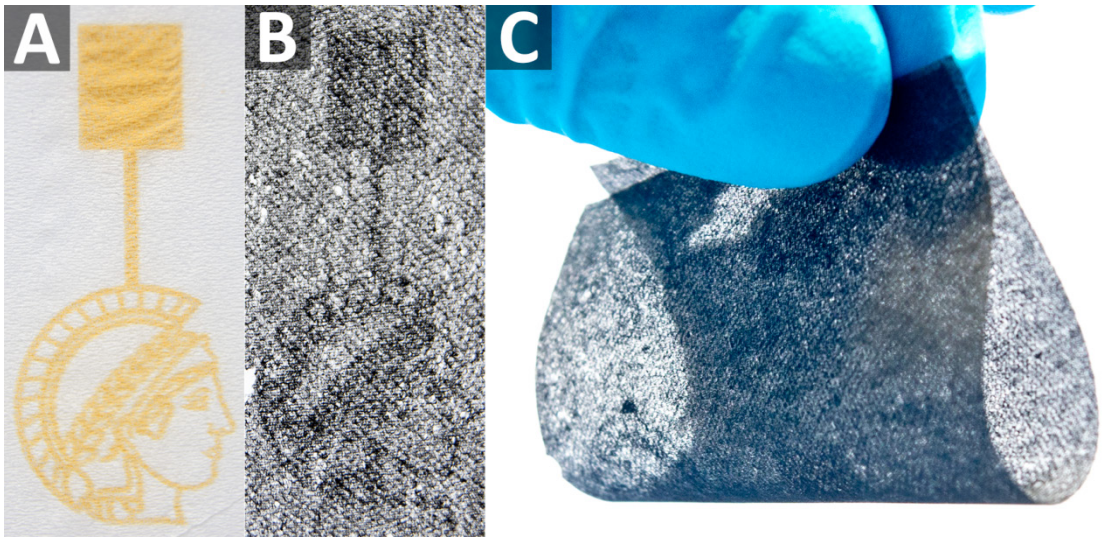

Figure 65: Example of the flexible electrodes. **A**: After printing – note that the quality of the print is not reduced by using the ultra-thin cloth. **B**: After calcination, the Minerva is again flawless. Due to the thin nature of the cloth the material is translucent. **C**: The flexibility of the calcined cloth is high enough to grab it and fold it without breaking.

This makes it possible, through simple choice of paper, to fabricate two types of self-sustaining electrodes: either sturdy, but more brittle electrodes or highly flexible

cloth-like electrodes that in turn are a more prone to ripping. It has to be stressed that retaining such a high degree of flexibility through a high temperature treatment is by no means trivial. Processing temperatures of 800 °C and more usually yield crystalline materials or simply burn any present organic matter that could facilitate flexibility.

Printing of Prefabricated Nanoparticles

In cooperation with Dr. Xiaofeng Liu experiments to explore the limits of the presented ink-jet printing approach were performed. For this a different ink, containing prefabricated silicon carbide nano-particles dispersed in water with the help of poly(ionic liquids) (PILs), was used. The ink and all parts of it are courtesy of Dr. Liu's work and were only used to probe the possibilities of this technique.

The procedure remained the same: a dispersion of the nano-particles was filled into an ink-cartridge and the cartridge was directly installed into the printer. After a single print no structures were visible on the paper, however printing several times onto the same paper showed that indeed the silicon carbide particles could be printed (**Figure 66**).

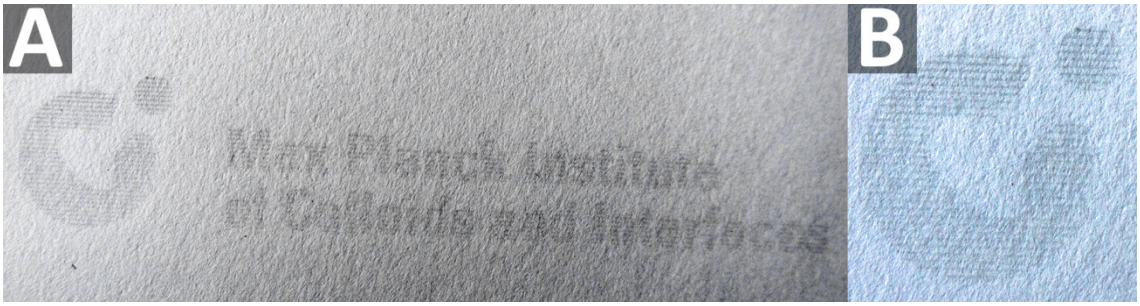

Figure 66: Result of the printed PILs@SiC nano-particles. **A**: The MPI CI logo. **B**: Closeup of the "C" visualising the lining in the print.

The quality of the print is not as high as with the aqueous solutions presented before, but it most certainly works and thus proves that even pre-fabricated and dispersed materials can be processed by this approach. *Öhlund* and co-workers have discussed the quality issue and concluded that for the printing of silver nanoparticles the roughness and porosity of the paper substrate are the most crucial factors for the morphology of the resulting structure.[91] In the here presented case, the lack in quality may also be due to the fact that the paper was printed on repeatedly in order to make agglomerates of the dispersed particles visible to the human eye.

CONCLUSION AND PROSPECT

Cellulose has been shown to be an exceptional substrate for many structuring and patterning techniques from origami folding to ink-jet printing. It has furthermore been shown that by choosing an appropriate paper, products ranging from stiff, fully

self-sustaining monoliths to ultra-thin and highly flexible cloths can be obtained after high temperature treatment.

The resulting products have been employed as electrodes, which was exemplified by electrodepositing copper onto them. *Via* ink-jet printing they have furthermore been patterned and the resulting electrodes have also been post functionalised by electro-deposition of copper onto the graphitised (printed) parts of the samples. Lastly in a preliminary test the possibility of printing several metals simultaneously and thereby producing finely tuneable gradients from one metal to another have successfully been made.

This concept could easily be utilised to obtain full phase diagrams of any printable metal (and combinations thereof), and it might also have large implications in the field of catalysis.

Another potential use of the printing approach is the finding that the printed ink actually only travels approximately 30 µm deep into the filter paper. This leaves the backside of the paper amorphous and none-conductive. This means that by printing something on the other side of the paper one automatically has access to lateral structuring and could e.g. produce a simple fuel cell *via* this approach by printing catalysts for ORR and OER on either side along with a graphitising agent to make the paper conductive on the surface.

VII. Green Synthesis and Applications

Introduction

Societal concerns about the impact that everyone's actions have on our planet have grown immensely. This has, for example, lead to the twelve principles of green chemistry as formulated by *Anastas* and *Warner*, which are widely recognised as the cornerstone and standard for any chemical processes that wish to be considered environmentally benign today.[92]

With this in mind a scientist nowadays cannot and should not ignore her/his moral obligations to consider the impact of his/her work on the environment. Indeed, all resources that were employed in this work are highly abundant and either come from renewable resources (namely cellulose) or are already part of well-established recycling procedures (namely metals). In this spirit the only synthesis step in the reactions presented here that could be considered questionable is the heating procedure under inert atmosphere. Even though it seems to be the more obvious problem, the high temperature is not necessarily an issue. The reason for this is that in the chemical industry high temperature processes are often highly integrated with other reactions. For example the hot atmosphere coming from one reaction fuels the next reaction that needs slightly lower temperatures; through couplings of this kind every single reaction in a larger set becomes energy and resource efficient. This comes of course with the drawback that this efficiency can only be reached in specialised chemical plants; once a reaction is detached from such a cycle the high temperature immediately becomes an issue again. The other problem is the inert atmosphere; any kind of inert gas is only obtained at great energetic cost, let alone storage and transport of it.

In this chapter preliminary results will be presented that address some of the above issues. The synthesis will be done fully detached from any form of high-end equipment only performed in a home-built apparatus, with a low quality vacuum, with waste and unprocessed raw materials as reactants and only fuelled by direct sunlight. This makes the production of high surface area carbons with embedded iron carbide nanoparticles possible virtually anywhere on earth where the sun shines. This chapter will furthermore show that this nano-composite is a potent wastewater filtration agent, resulting in an ideal combination. It will be possible to produce a high performance filter for wastewater – something that is dearly needed in places where the most important resources for the chemical industry are usually not present: energy and top-notch equipment.

SUNLIGHT DRIVEN SYNTHESIS

The term solar energy is often associated with “solar cells” and, in fewer cases, with the concept of “solar heating”. Combining this with the task of performing high temperature syntheses solar cells are by no means a direct method of fuelling theses syntheses, since there are at least two energy conversion steps involved (light to electrical energy and then electrical energy to thermal energy). While this is a very general way of harnessing solar energy, it is not very efficient for the task at hand. In the spirit of easy and inexpensive processes another way is needed. Depending on the distance from the sun, the incident angle and atmospheric disturbances the sun sends an energy stream of approximately 1370 $W \cdot m^{-2}$ to earth. The second concept mentioned, solar heating, is a more direct approach, where sunlight used directly to heat a carrier substance. This carrier substance is typically oil or water for small scale, i.e. single house, applications or a salt mixture in so called solar thermal power plants. There are several more approaches to using thermal energy from sunlight directly.[93] Where small scale applications employ the sunlight “as is”, which strongly limits the achievable temperatures, large scale approaches rely on some way of focussing the sunlight to reach higher temperatures. This can be done by either using mirrors or lenses.

Transferring this idea to the syntheses presented in this thesis, solar energy, instead of being used to produce electricity, can of course also be used to directly heat the reaction mixture. To achieve temperatures of 800 °C, however, is by no means trivial. While mirrors are the conceptually easier method, they are more difficult to set-up. Lenses of sufficient size and thickness, on the other hand, if made from glass, are unwieldy to the point of uselessness.

As with many other examples the solution to this comes from an old concept; in this case one that is about to celebrate its 200th birthday: the *Fresnel* lens. The French physicist *Augustin-Jean Fresnel*, who is the eponym, but not the actual inventor of the concept, refined the build of this type of lens and made it applicable in light houses. Essentially the idea is that refraction only happens at the interface of lens and air, making all the glass inside “obsolete” (**Figure 67**). Reducing a lens to its curvature, of course, greatly reduces the weight and thickness of it and more importantly it drastically increases the transmittance of the lens.

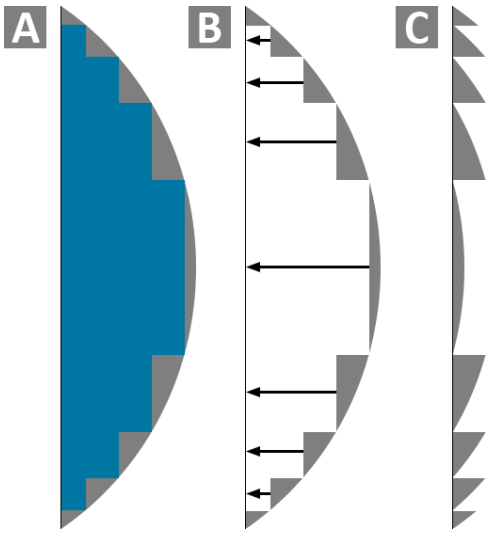

Figure 67: Scheme of a *Fresnel* lens. **A**: Original lens with surplus material in blue. **B**: Original lens without surplus material, arrows indicate repositioning of the remaining lens fragments. **C**: *Fresnel* lens derived from original lens.

Since they are typically made from plastics such as acrylates or polycarbonate they possess a high stress and wear resistance. The lens employed for the experiments in this chapter has a diameter of approximately 46 cm, a thickness of 3 mm and weighs only a few hundred grams.

Results

In a proof-of-principle approach an old desiccator – equipped with a valve connector on the side – was chosen as the reaction vessel. A crucible was mounted with metal wire on the ceramic plate that used to elevate the samples over the drying agent. The lid was replaced with a flat piece of glass; here deliberately a low quality regular window glass was chosen to ensure that no high-end optical parts are needed. The exact same reaction mixture as prepared in chapter III was pre-dried in air and then put into the crucible. The desiccator was sealed with the flat glass lid and a vacuum pump connected to the valve was used to produce a vacuum within the desiccator. Here the at best decent vacuum quality became apparent as immediately upon applying the vacuum the formation of bubbles at the interface of the flat glass with the desiccator body could be observed. Lastly the ready reaction vessel was placed in parallel to the *Fresnel* lens and pointed towards the sun (**Figure 68**).

Figure 68: Full reaction setup with *Fresnel* lens and the modified desiccator.

Here a warning is in order, even though the experiments were conducted under absolutely non-optimal sun light conditions the temperature at the focal point reached several hundred degrees Celsius within a matter of seconds, setting paper and wood afire immediately. Hence it is imperative that such large lenses are always be handled with caution and that extra care is taken not to get in contact with the concentrated beam in the vicinity of the focal point – even ten centimetres of-focus paper will burn quickly.

As was just pointed out the lighting conditions were less than optimal. The experiments were conducted during winter in Germany (around the beginning of December). Note the low incident angle of the sunlight in the picture above – it was taken at quarter past noon. Despite this to product formation was a matter of few minutes and most of this time was needed to move the focal point gradually over the sample, since the focal point was only about 2 mm in diameter and the sample area was approximately 1 cm across. This is necessary due to the poor heat conductivity of cellulose. This however suggests that the selective heating of parts of a cellulose cloth should be possible; no attempts to try this were made though. In **Figure 69** the reaction can be seen directly – something that would absolutely not be possible with conventional chamber ovens.

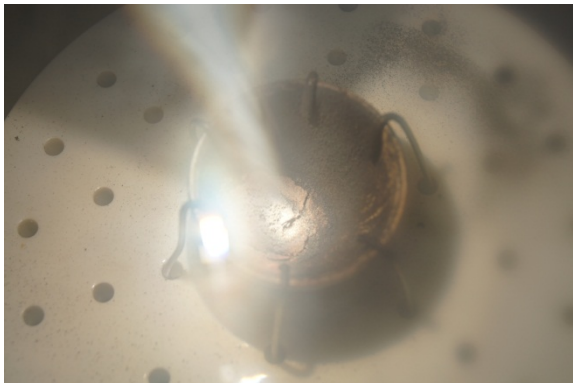

Figure 69: Example of the reaction within the desiccator. The focal point has been moved to the side to make it possible to take a picture.

The resulting product was still not phase pure, but already the first attempts brought about iron carbide as the main phase (**Figure 70**) along with some unreacted cellulose and iron oxide (Fe_3O_4) as well as some traces of elemental iron.

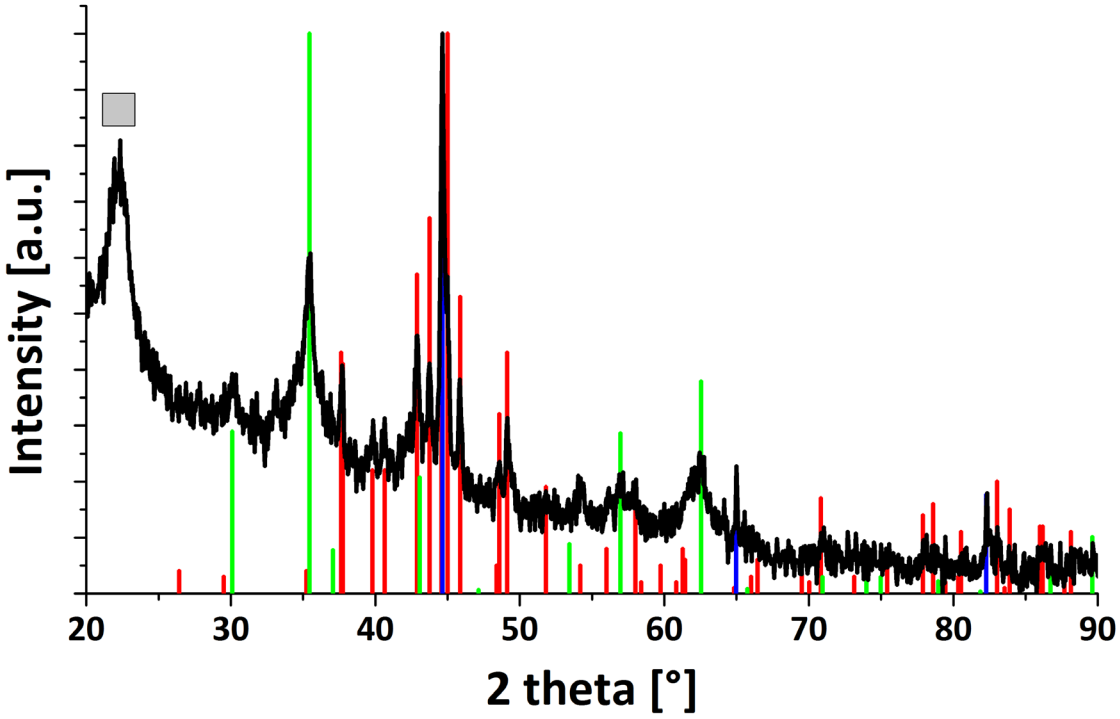

Figure 70: XRD pattern of the product obtained from the synthesis with the *Fresnel* lens. The main phase is iron carbide (red, ICDD 00-035-0772), but Fe_3O_4 (green, ICDD 01-077-1545) and Fe^0 (blue, ICDD 04-007-9453) are visible along with unreacted cellulose (marked with a grey square, ICDD 00-056-1719).

The reason for this somewhat inhomogeneous product is the ratio of sample size to focal point. It causes, in the present set-up, an uneven temperature distribution within the sample. This is however easy to overcome when the reaction is performed at better lighting conditions. Then the reaction can also be performed out of focus allowing for the irradiation spot to encircle the entire sample.

Summary

Despite the use of sub-optimal conditions, such as low quality glass (relatively high absorption) as the reaction vessel lid and non-optimal lighting conditions, the synthesis was still successful and yielded without any optimisation of the reaction conditions iron carbide as the main product.

Also the focused light setup appears to be usable similar to laser scribing techniques. By taking advantage of the bad thermal conductivity of cellulose it becomes possible to pattern the samples by "writing" on them with the beam of concentrated light.

Most importantly this proof-of-principle shows that even though all the syntheses presented in this work are done at moderately high temperatures they – in principle – could be performed away from any specialised equipment and energy source.

SCRAP METAL, COFFEE FILTERS AND SOME WOOD

The precursors employed thus far are already based on renewable resources, but both, iron salts and cellulose, still undergo some degree of processing before they are used in the syntheses presented here. Consequently there is still room for further simplification. The lab-grade filter paper was firstly replaced by coffee filter paper (**Figure 71**), which is quality wise the first step after wood pulp. It is composed of unbleached and additive free cellulose. The material resulting from this is absolutely indistinguishable from the one obtained with lab-grade cellulose.

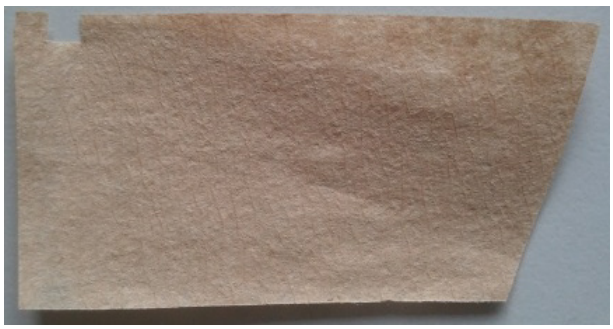

Figure 71: Example of a piece of coffee filter that was used.

The next step was to go down another processing step – and thereby add a novel way of patterning. Using unprocessed dry wood worked just as well. The wood had to be soaked for several hours, as opposed to the direct uptake observed with cellulose, but the product was again iron carbide embedded in graphitized carbons **Figure 72**.

Figure 72: Wood samples **A**: before (not soaked) and **B**: after calcination.

XRD spectroscopy could be performed directly on the monolithic specimens and showed that iron carbide was obtained along with a significant degree of graphitisation (**Figure 73**).

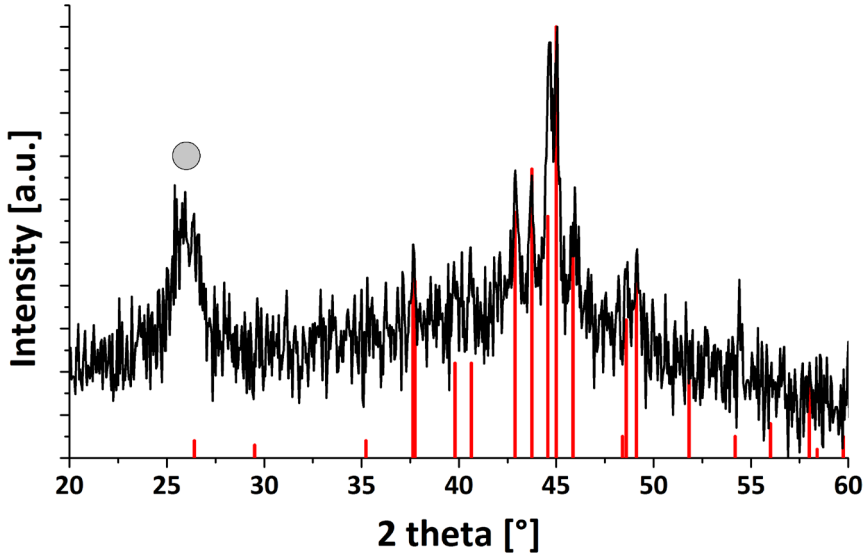

Figure 73: XRD pattern obtained from a piece of wood calcined after soaking with an iron salt solution. Reference pattern: Fe_3C (red, ICDD 00-035-0772) and the peak at 26° 2 theta marked with a grey circle is attributed to graphite (ICDD 04-015-2407).

As with cellulose the conversation to the nano-composite takes place under full retention of the wood morphology. Even small features like cell walls and membranes are still visible (**Figure 74**).

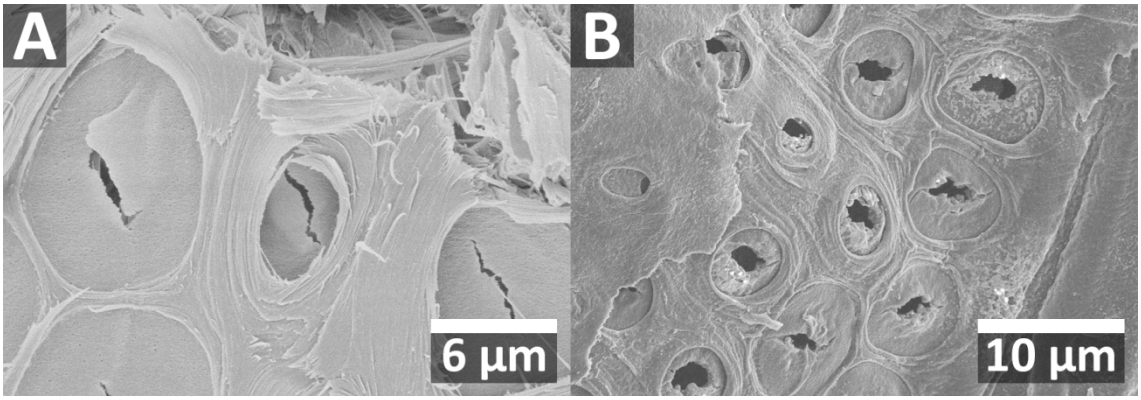

Figure 74: SEM micrographs of pure, untreated wood (**A**) and of the final product (**B**) showing the well retained wood morphology down to the cellular level.

Ultra-microtome cuts of the calcined wood samples show the shape retention down to the cellular level even more impressively. They furthermore show that wood is an ideal candidate to produce hierarchical structures (**Figure 75**).

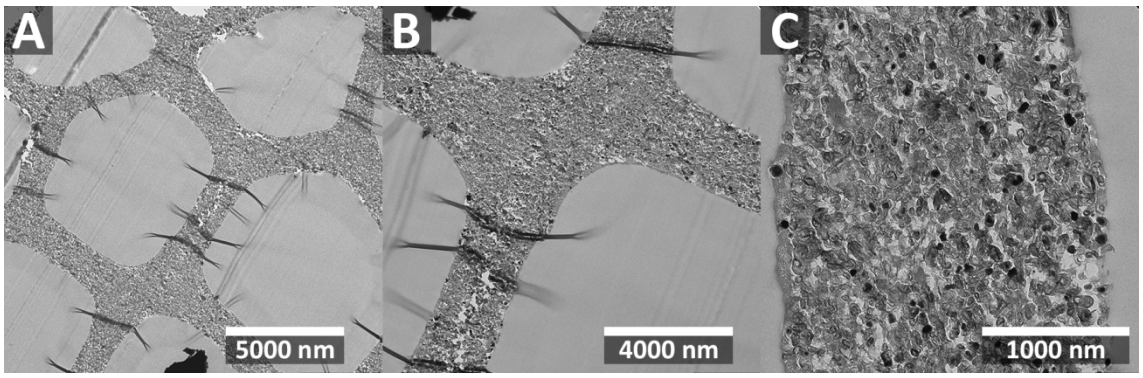

Figure 75: TEM micrographs of UM cuts of wood specimens after high temperature treatment with increasing magnification (**A-C**).

This technique can be used to replace processed cellulose by unprocessed wood. The outstanding shape retention can now exploit the different porosities inherent to every type of wood. The µm pore sized can simply be determined by the choice of wood that is used as a starting material. Furthermore, this means that the established shaping techniques available for wooden objects are accessible for product manufacture – most notably modern high precision CNC milling machines that can shape wooden objects with high accuracy.

As the cellulose precursors was tested in an as raw as possible condition the iron sources deserves some attention as well. Now mining raw iron ore would be over-doing it, but using un-cleaned scrap metal appeared to be a reasonable choice. For this at least partially bare specimens of metal were picked from a scrapyard, cut down to a size usable in a round bottom flask and otherwise used as they were (**Figure 76**).

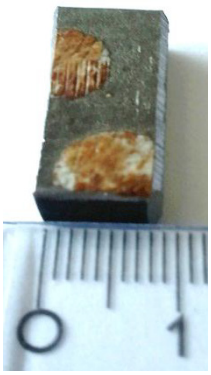

Figure 76: Example of a scrap metal specimen after cutting.

The scrap metal pieces were dissolved in acetic acid, it only takes a few hours before the solution darkens notably, complete dissolution can take up to several weeks,

depending on the size and shape of the metal piece. The solution is however usable after a few hours, to reach a sufficient iron concentration in the samples the immersion has to be repeated several times (soaking, dying, soaking, etc.), but the quality of the final product is not attenuated by this.

DYE-FILTRATION

The previous sections demonstrated crude, but effective and, more importantly, independent of any sophisticated equipment, ways to synthesise porous iron carbide hybrids. Since high surface area carbons are known to be versatile filtration agents,[94] and the magnetic nature of the products is a helpful addition the obtained composited were tested for their ability to cleanse waste water. For this methylene blue (MB) was chosen as a common organic dye that gives good optical contrast. A stock solution of 1 g methylene blue per litre of water was prepared and *via* serial dilution concentrations of 1000 mg/L down to 15.625 mg/L were obtained. To 1 mL of each of the solutions 5 mg of the nano hybrid were added and the components were mixed *via* shaking. The cleaning effect was instantaneous and did not change over time. UV-Vis spectrometry monitoring the main absorption peak at 670 nm was used to evaluate the adsorption efficiency (**Figure 77**).

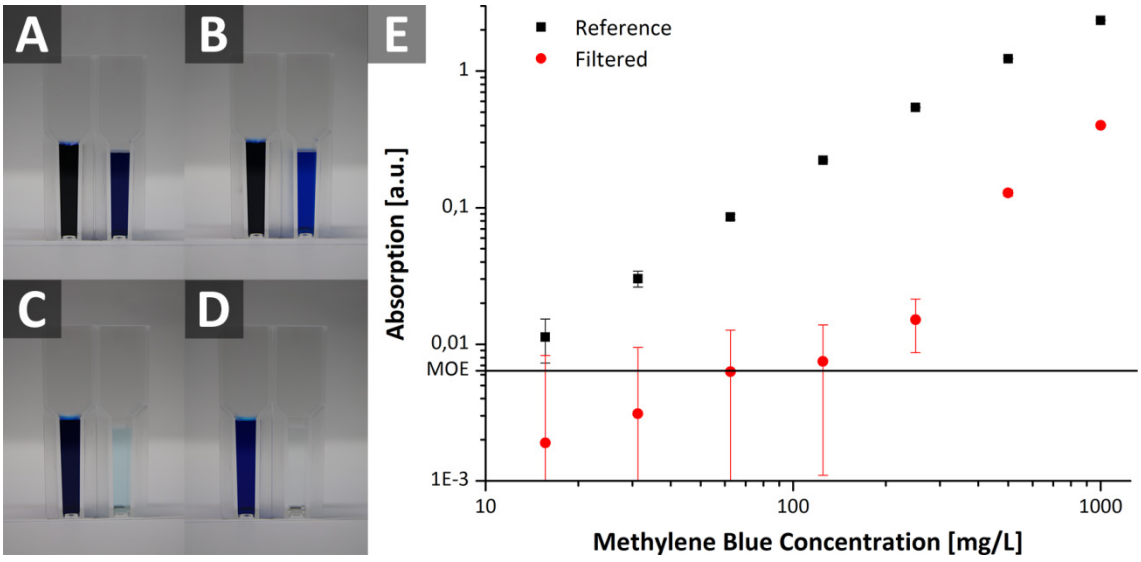

Figure 77: **A – D** Pairs of methylene blue stock solutions (left cuvette) and the corresponding solution that was filtered with 5 mg of the iron carbide @ carbon composite (right cuvette). Stock solution concentrations from left to right: 1000 mg/L, 500 mg/L, 250 mg/L, 125 mg/L methylene blue. **E**: Photo-spectrometric analysis of the same samples.

From this curve, an absorption capacity of approximately 40 mg methylene blue per g nano-composite was derived. Once cleaned the powder binds the methylene blue effectively. Solutions that were mixed with the powder have been stored now for

more than half a year without any observable change. By adding ethanol however the filter readily releases the methylene blue again (**Figure 78**).

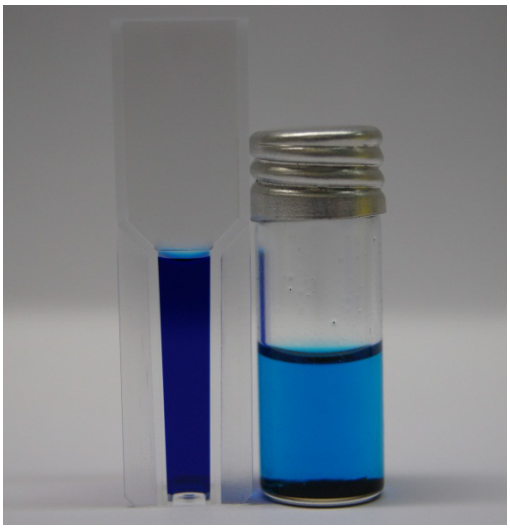

Figure 78: **Left**: original 125 mg/L methylene blue solution. **Right**: powder with the first ethanol washing solution.

This means that in principle the adsorbent can be recycled; several washing steps with ethanol are however needed to fully recover the filtering capacity. One well known property of iron compounds becomes very important here: they are highly magnetic. The filtrating agent can easily and fully be removed simply by holding a magnet up to the vessel and decanting the solution, the powder can even be separated from a flowing solution – a magnet was held below the nozzle of a beaker filled with the cleaned solution and the powder and then the contend was rapidly poured into another vessel. All of the powder was held back by doing this. In fact all the solutions for the UV-Vis spectrometry were prepared this way.

CONCLUSION

This chapter has shown just how robust the synthesis of porous carbons with embedded iron carbide nanoparticles is by performing the synthesis with partly dissolved scrap metal and pieces of raw, dry wood. This in turn brings about several advantages for further use of the general synthesis technique. For example by using wood instead of processed cellulose all the established shaping techniques available for wooden objects, such as CNC milling or 3D prototyping, become accessible for this synthesis path. By using wood, also two of its highly refined intrinsic properties can be exploited. Through choosing a task specific type of wood its inherent micrometre porosity can be converted to be the larger fraction of a hierarchical pore structure. Secondly the large monoliths, which can be pre-shaped with high precision, are obtained by this. Those two advantages enable precise tailoring of the structure and its porosity from the centimetre to the nanometre scale and thereby help expanding the prospect of using the composite as a facile catalyst in many applications.

Furthermore the fact that the reaction was performed in a crude, self-made glass vessel, fuelled – with the help of a *Fresnel* lens – by direct concentrated sunlight irradiation makes the leap from the reaction being a common laboratory synthesis to real world applicability. After all it was also demonstrated in this chapter that the resulting material can be applied waste water filtration and is even recyclable.

VIII. SUMMARY AND OUTLOOK

Cellulose is the most abundant biopolymer on earth.[95] In this work it has been used, in various forms ranging from wood to fully processed laboratory grade microcrystalline cellulose, to synthesise a variety of metal and metal carbide nanoparticles and to establish structuring and patterning methodologies that produce highly functional nano-hybrids.

To achieve this, the mechanisms governing the catalytic processes that bring about graphitised carbons in the presence of iron have been investigated. It was found that, when infusing cellulose with an aqueous iron salt solution and heating this mixture under inert atmosphere to 640 °C and above, a liquid eutectic mixture of iron and carbon with an atom ratio of approximately 1:1 forms. The eutectic droplets were monitored with *in-situ* TEM at the reaction temperature where they could be seen dissolving amorphous carbon and leaving behind a trail of graphitised carbon sheets and subsequently iron carbide nanoparticles. These transformations turned ordinary cellulose into a conductive and porous matrix that is well suited for catalytic applications. Despite these significant changes on the nanometre scale the shape of the matrix as a whole was retained with remarkable precision. This was exemplified by folding a sheet of cellulose paper into origami cranes and converting them *via* the temperature treatment in to magnetic facsimiles of those cranes. The study showed that the catalytic mechanisms derived from controlled systems and described in the literature can be transferred to synthetic concepts beyond the lab without loss of generality.

Once the processes determining the transformation of cellulose into functional materials were understood, the concept could be extended to other metals and metal-combinations. Firstly, the procedure was utilised to produce different ternary iron carbides in the form of M_xFe_yC (M = W, Mn). Iron in combination with tungsten brought about $Fe_{21}W_2C_6$ and Fe_3W_3C during the course of this work neither of those could be obtained in a phase pure form, but work within our group utilising other biopolymers showed that this is in principle possible by simply probing for the correct temperature treatment. An advantage though is that the combination of cellulose and the metal precursors yields porous products; a feat that other biopolymers, such as agar or gelatine cannot reproduce.

In a follow up synthesis to produce phase pure ternary carbides and to probe whether lessons learned from the tungsten-iron system could be conveyed to other ternary systems, manganese, a metal that is structurally closer to iron, was investigated. With this combination the phase pure ternary carbide $Mn_{0.75}Fe_{2.25}C$ was obtained. None of those ternary carbides have thus far been produced in a

nanoparticle form. All work regarding them was up until now performed by the steel industry whose interest was the assessment of the influence of metal additions and impurities on the properties of bulk materials, namely industrial high performance steels.

The next part of this work encompassed combinations of iron with cobalt, nickel, palladium and copper. All of those metals were also probed alone in combination with cellulose. This produced elemental metal and metal alloy particles of low polydispersity and high stability. Both features are something that is typically not associated with high temperature syntheses and enables to connect the good size control with a scalable process. In the case of copper, no alloying with iron was observed, but copper nanoparticles of 9 nm size embedded in the carbon matrix were obtained. Furthermore several effects of interest were found. One is that the copper nanoparticles actually consisted of minute copper clusters, with each being made from only approximately 100 copper atoms. Moreover the presence of the copper fcc lattice, during the catalytic conversion of the cellulose matrix by the iron eutectic, promoted the formation of diamond-like carbons, that themselves possess a fcc lattice. Lastly these experiments gave insight into the formation of the nanoparticles. They indicated that, in the case of copper, larger particles can be formed on the surface of the fibres due to the higher mobility of the reactants there. This was shown by the discovery of a depletion zone close to the surface of the carbon fibres, which was void of any particles. The formation of the diamond-like carbons deserves more attention, as production under such simple reaction conditions is exceptional.

Nickel generated well dispersed single crystalline nanoparticles of 5.5 nm diameter. Also nickel is a metal which is particularly prone to alloying. This, in the end, made it possible to synthesise not only Ni^0 nanoparticles of such quality, but also several alloys, namely FeNi, $Fe_{0.67}Ni_{0.32}$ and NiPd were successfully obtained. Due to their well-defined structure and applicability in catalysis attempts were made to release the nanoparticles from the stabilising matrix and disperse them in a solvent. This was achieved by submersing the crude product in toluene and ultrasonic treatment in the presence of oleic acid as a dispersing agent. The resulting dispersion was fully stable, but some coalescence of the nickel nanoparticles was observed and not all particles were released from the matrix. However, the nickel based system is now a good starting point to derive a reliable way of releasing the metal(0) nanoparticles from the carbon matrix and stabilising them in solution.

The last metal probed was cobalt, here the use of cobalt salts and cellulose can yield cobalt nanoparticles dispersed in amorphous carbon and a small degree of size control between 700 °C, which yielded particles of 1.5 nm size, and 800 °C, which gave diameters of about 5 nm, can be exerted. Increasing the reaction temperature above

900 °C brings about larger cobalt nanoparticles and broadens the size distribution but also graphitises the matrix, thus embedding the particles in a conductive, self-standing framework. The addition of iron to the cobalt precursor results in particles of the same morphology, but, depending on the metal ratio CoFe or Co_3Fe_7 alloys are obtained. Each of the probed reactions resulted in phase pure, single crystalline, stable materials. Lastly, some preliminary tests to control the porosity obtained with the cobalt-iron system have been performed. Control *via* a pre-drying step as well *via* the alloying ratio appears to be possible with reasonable accuracy, but especially the reasons and mechanisms for the formation of large micrometre pores in the carbon scaffold are not yet fully understood and should be investigated further to enable prediction of the porosities obtained.

After showing that cellulose is a good stabilising and separating agent for all the investigated types of nanoparticles, the focus of the work at hand is shifted towards probing the limits of the structuring and pattering capabilities of cellulose. Moreover possible post-processing techniques to further broaden the applicability of the materials are evaluated.

This showed that, by choosing an appropriate paper, products ranging from stiff, self-sustaining monoliths to ultra-thin and very flexible cloths can be obtained after high temperature treatment. Furthermore cellulose has been demonstrated to be a very good substrate for many structuring and patterning techniques from origami folding to ink-jet printing. The thereby resulting products have been employed as electrodes, which was exemplified by electrodepositing copper onto them. *Via* ink-jet printing they have additionally been patterned and the resulting electrodes have also been post functionalised by electro-deposition of copper onto the graphitised (printed) parts of the samples. Lastly in a preliminary test the possibility of printing several metals simultaneously and thereby producing finely tuneable gradients from one metal to another have successfully been made. Starting from these concepts future experiments were outlined.

The last chapter of this thesis concerned itself with alternative synthesis methods of the iron-carbon composite, thereby testing the robustness of the devolved reactions. By performing the synthesis with partly dissolved scrap metal and pieces of raw, dry wood, some progress for further use of the general synthesis technique were made. For example by using wood instead of processed cellulose all the established shaping techniques available for wooden objects, such as CNC milling or 3D prototyping, become accessible for the synthesis path. Also by using wood its intrinsic well defined porosity and the fact that large monoliths are obtained help expanding the prospect of using the composite. It was also demonstrated in this chapter that the resulting material can be applied for the environmentally important issue of waste

water cleansing. Additionally to being made from renewable resources and by a cheap and easy one-pot synthesis, the material is recyclable, since the pollutants can be recovered by washing with ethanol. Most importantly this chapter covered experiments where the reaction was performed in a crude, home-built glass vessel, fuelled – with the help of a *Fresnel* lens – only by direct concentrated sunlight irradiation. This concept carries the thus far presented synthetic procedures from being common laboratory syntheses to a real world application.

Based on cellulose, transition metals and simple equipment, this work enabled the easy one-pot synthesis of nano-ceramic and metal nanoparticle composites otherwise not readily accessible. Furthermore were structuring and patterning techniques and synthesis routes involving only renewable resources and environmentally benign procedures established here. Thereby it has laid the foundation for a multitude of applications and pointed towards several future projects reaching from fundamental research, to application focussed research and even and industry relevant engineering project was envisioned.

OUTLOOK

Even though the mechanism of the catalytic graphitisation derived from the results is conclusive a last experiment employing some form of *in-situ* XRD technique (e.g. an experiment at a synchrotron facility) would be interesting. The study presented suggests, but does not definitely prove, that the iron carbide is not formed until the sample is cooled back down.

Studies probing the catalytic performance of both of the synthesised tungsten-iron carbides would also be of interest, since this is the first time that $Fe_{21}W_2C_6$ has been produced in nanoparticulate form. Now a comparison of the low tungsten content ternary carbide ($Fe_{21}W_2C_6$) with other iron tungsten carbides and the respective single metal carbides is possible. This could eventually shine light on the existence of synergistic effects in catalysis and also illuminate which part either metal plays these effects.

The syntheses involving copper offers two points that could be followed up on. One is the production of DLCs. Here the separation from the other products (Cu^0, Fe^0 and graphitic carbon) is a crucial issue that needs to be addressed first. The other is the formation of few-atom, stable copper clusters. They could be the focus of further studies, especially in the field of catalysis, should it be possible to stabilise them in solution as well. Hence this challenge should be tackled first.

Similarly, dispersing the well-defined Co^0 nanoparticles, which can now be easily obtained in quantities, is worthwhile. This demands that the results regarding the

dispersability of the particles that were obtained with nickel must be transferred to the cobalt system as well. Testing of the thus obtained particles for catalytic performance and comparison with the cobalt-carbon composite might also be a fascinating study. Lastly, since the cobalt system in particular possesses a good stability against temperature changes it could be well suited to serve as a model system to further the understanding of synergistic substrate-catalyst effects.

The dispersability of all presented metal and alloy nanoparticles is interesting in general. The presented syntheses can be used to produce the particles on the gram scale and obtain them in an inert matrix, namely the former cellulose, for long term storage and transport purposes. If a way to disperse them is found, they later could be released from the carbon framework and stabilised in solution on demand in the desired quantities. This would produce good quality nanoparticles with a long shelve life. Once such a procedure is established it could easily be transferred to other systems than the ones presented in this work and subsequently offer a way of producing large quantities of well-defined nanoparticles. Thereby solving the initially stated problem that a way of pooling the advantages of solution based syntheses (high particle quality) with top-down approaches (scalability of the synthesis) is still sought after.

Regarding the sunlight driven synthesis, implementing the reaction without sophisticated equipment and without electricity opens it up to additional fields. Independent of the reaction performed, the prospect of generalising this concept is potentially important to any high temperature synthesis. Functional oxides, such as high temperature superconductors, would for example also be an interesting class of materials for this. The synthesis of iron carbide, which was used as a model system for the sunlight driven synthesis, is however very robust. In order to broaden the applicability of this concept it would be necessary to devise an apparatus that offers control over the amount of gathered sunlight, e.g. by adding an aperture to the *Fresnel* lens, since other syntheses demand much more controlled reaction conditions. The prospect of the generalisations proposed in *chapter VII* holding true would make further research into this concept very interesting.

IX. REFERENCES

[1] H. Sirringhaus, T. Kawase, R. H. Friend, T. Shimoda, M. Inbasekaran, W. Wu, E. P. Woo. "High-Resolution Inkjet Printing of All-Polymer Transistor Circuits". *Science* **290**, 2123, doi:10.1126/science.290.5499.2123 (**2000**).

[2] L. Shui, A. van den Berg, J. C. T. Eijkel. "Scalable Attoliter Monodisperse Droplet Formation Using Multiphase Nano-Microfluidics". *Microfluidics and Nanofluidics* **11**, 87, doi:10.1007/s10404-011-0776-7 (**2011**).

[3] S. R. Hall. *Biotemplating: Complex Structures from Natural Materials* (**2009**).

[4] T. Yokoyama in *Nanoparticle Technology Handbook* (Eds.: M. Hosokawa, K. Nogi, M. Naito, et al.), Elsevier, Amsterdam, (**2008**), pp. 3.

[5] P. Martino, P. Allia, A. Chiolerio. "Nanoparticles" in *Encyclopedia of Nanotechnology* (Ed.: B. Bhushan), Springer, Netherlands, (**2012**), pp. 1660.

[6] U. Leonhardt. "Optical Metamaterials: Invisibility Cup". *Nature Photonics* **1**, 207, doi:10.1038/nphoton.2007.38 (**2007**).

[7] P. Buffat, J.-P. Borel. "Size Effect on the Melting Temperature of Gold Particles". *Physical Review A* **13**, 2287, doi:10.1103/PhysRevA.13.2287 (**1976**).

[8] K. J. Klabunde, J. Stark, O. Koper, C. Mohs, D. G. Park, S. Decker, Y. Jiang, I. Lagadic, D. Zhang. "Nanocrystals as Stoichiometric Reagents with Unique Surface Chemistry". *The Journal of Physical Chemistry* **100**, 12142, doi:10.1021/jp960224x (**1996**).

[9] M. Niederberger, N. Pinna in Engineering Materials and Processes (*Vol. Metal Oxide Nanoparticles in Organic Solvents*, Springer, London, (**2009**), pp. 19.

[10] J. Park, J. Joo, S. G. Kwon, Y. Jang, T. Hyeon. "Synthesis of Monodisperse Spherical Nanocrystals". *Angewandte Chemie International Edition* **46**, 4630, doi:10.1002/anie.200603148 (**2007**).

[11] S. Krishnadasan, J. Tovilla, R. Vilar, A. J. deMello, J. C. deMello. "On-Line Analysis of CdSe Nanoparticle Formation in a Continuous Flow Chip-Based Microreactor". *Journal of Materials Chemistry* **14**, 2655, doi:Doi 10.1039/B401559b (**2004**).

[12] M. Niederberger, N. Pinna in Engineering Materials and Processes (*Vol. Metal Oxide Nanoparticles in Organic Solvents*, Springer, London, (**2009**), pp. 7.

[13] L. B. Kiss, J. Söderlund, G. A. Niklasson, C. G. Granqvist. "New Approach to the Origin of Lognormal Size Distributions of Nanoparticles". *Nanotechnology* **10**, 25, doi:10.1088/0957-4484/10/1/006 (**1999**).

[14] S. T. Oyama. "Preparation and Catalytic Properties of Transition-Metal Carbides and Nitrides". *Catalysis Today* **15**, 179, doi:10.1016/0920-5861(92)80175-M (**1992**).

[15] C. Giordano, M. Antonietti. "Synthesis of Crystalline Metal Nitride and Metal Carbide Nanostructures by Sol-Gel Chemistry". *Nano Today* **6**, 366, doi:10.1016/j.nantod.2011.06.002 (**2011**).

[16] H. Binder, A. Köhling, W. Kuhn, W. Lindner, G. Sandstede. "Tungsten Carbide Electrodes for Fuel Cells with Acid Electrolyte". *Nature* **224**, 1299, doi:10.1038/2241299b0 (**1969**).

[17] A.-M. Alexander, J. S. J. Hargreaves. "Alternative Catalytic Materials: Carbides, Nitrides, Phosphides and Amorphous Boron Alloys". *Chemical Society Reviews* **39**, 4388, doi:10.1039/B916787K (**2010**).

[18] Z. Schnepp, M. Thomas, S. Glatzel, K. Schlichte, R. Palkovits, C. Giordano. "One Pot Route to Sponge-Like Fe_3N Nanostructures". *Journal of Materials Chemistry* **21**, 17760, doi:10.1039/C1jm12842f (**2011**).

[19] D. V. Suetin, I. R. Shein, A. L. Ivanovskii. "Tungsten Carbides and Nitrides and Ternary Systems Based on Them: The Electronic Structure, Chemical Bonding and Properties". *Russian Chemical Reviews* **79**, 611, doi:10.1070/RC2010v079n07ABEH004141 (**2010**).

[20] C. B. Pollock, H. H. Stadelmaier. "The Eta Carbides in the Fe-W-C and Co-W-C Systems". *Metallurgical and Materials Transactions B* **1**, 767, doi:10.1007/BF02811752 (**1970**).

[21] R. E. Franklin. "Crystallite Growth in Graphitizing and Non-Graphitizing Carbons". *Proceedings of the Royal Society A: Mathematical, Physical and Engineering Sciences* **209**, 196, doi:10.1098/rspa.1951.0197 (**1951**).

[22] A. I. Savvatimskiy. "Measurements of the Melting Point of Graphite and the Properties of Liquid Carbon (a Review for 1963–2003)". *Carbon* **43**, 1115, doi:10.1016/j.carbon.2004.12.027 (**2005**).

[23] S. Ragan, H. Marsh. "Science and Technology of Graphite Manufacture". *Journal of Materials Science* **18**, 3161, doi:10.1007/BF00544139 (**1983**).

[24] A. Ōya, H. Marsh. "Phenomena of Catalytic Graphitization". *Journal of Materials Science* **17**, 309, doi:10.1007/BF00591464 (**1982**).

[25] Y. Gogotsi, A. Nikitin, H. Ye, W. Zhou, J. E. Fischer, B. Yi, H. C. Foley, M. W. Barsoum. "Nanoporous Carbide-Derived Carbon with Tunable Pore Size". *Nature Materials* **2**, 591, doi:10.1038/nmat957 (**2003**).

[26] M. J. Allen, V. C. Tung, R. B. Kaner. "Honeycomb Carbon: A Review of Graphene". *Chemical Reviews* **110**, 132, doi:10.1021/cr900070d (**2010**).

[27] A. Ōya, S. Ōtani. "Catalytic Graphitization of Carbons by Various Metals". *Carbon* **17**, 131, doi:10.1016/0008-6223(79)90020-4 (**1979**).

[28] W. Weisweiler, N. Subramanian, B. Terwiesch. "Catalytic Influence of Metal Melts on the Graphitization of Monolithic Glasslike Carbon". *Carbon* **9**, 755, doi:10.1016/0008-6223(71)90008-X (**1971**).

[29] K. Jiang, C. Feng, K. Liu, S. Fan. "A Vapor-Liquid-Solid Model for Chemical Vapor Deposition Growth of Carbon Nanotubes". *Journal of Nanoscience and Nanotechnology* **7**, 1494, doi:10.1166/jnn.2007.332 (**2007**).

[30] O. P. Krivoruchko, V. I. Zaikovskii. "Formation of Liquid Phase in the Carbon-Metal System at Unusually Low Temperature". *Kinetics and Catalysis* **39**, 561 (**1998**).

[31] X. Feng, S. W. Chee, R. Sharma, K. Liu, X. Xie, Q. Li, S. Fan, K. Jiang. "In Situ TEM Observation of the Gasification and Growth of Carbon Nanotubes Using Iron Catalysts". *Nano Research* **4**, 767, doi:10.1007/s12274-011-0133-x (**2011**).

[32] W. Pease. "An Automatic Machine Tool". *Scientific American* **187**, 101, doi:10.1038/scientificamerican0952-101 (**1952**).

[33] K.-L. Yiu, H.-Y. Tam. "An Alternate Approach to Free-Form Surface Fabrication". *Journal of Materials Processing Technology* **192-193**, 465, doi:10.1016/j.jmatprotec.2007.04.057 (**2007**).

[34] B. Duan, M. Wang. "Selective Laser Sintering and Its Application in Biomedical Engineering". *MRS Bulletin* **36**, 998, doi:10.1557/mrs.2011.270 (**2011**).

[35] T. Ohuchi, Y. Murase. "Milling of Wood and Wood-Based Materials with a Computerized Numerically Controlled Router IV: Development of Automatic Measurement System for Cutting Edge Profile of Throw-Away Type Straight Bit". *Journal of Wood Science* **51**, 278, doi:10.1007/s10086-004-0663-x (**2005**).

[36] W. Mueannoom, A. Srisongphan, K. M. Taylor, S. Hauschild, S. Gaisford. "Thermal Ink-Jet Spray Freeze-Drying for Preparation of Excipient-Free Salbutamol Sulphate for Inhalation". *European Journal of Pharmaceutics and Biopharmaceutics* **80**, 149, doi:10.1016/j.ejpb.2011.09.016 (**2012**).

[37] S. Hauschild, U. Lipprandt, A. Rumplecker, U. Borchert, A. Rank, R. Schubert, S. Forster. "Direct Preparation and Loading of Lipid and Polymer Vesicles Using Inkjets". *Small* **1**, 1177, doi:10.1002/smll.200500093 (**2005**).

[38] M. Lejeune, T. Chartier, C. Dossou-Yovo, R. Noguera. "Ink-Jet Printing of Ceramic Micro-Pillar Arrays". *Journal of the European Ceramic Society* **29**, 905, doi:10.1016/j.jeurceramsoc.2008.07.040 (**2009**).

[39] J. Hiller, J. D. Mendelsohn, M. F. Rubner. "Reversibly Erasable Nanoporous Anti-Reflection Coatings from Polyelectrolyte Multilayers". *Nature Materials* **1**, 59, doi:10.1038/nmat719 (**2002**).

[40] J. H. Cho, J. Lee, Y. Xia, B. Kim, Y. He, M. J. Renn, T. P. Lodge, C. D. Frisbie. "Printable Ion-Gel Gate Dielectrics for Low-Voltage Polymer Thin-Film Transistors on Plastic". *Nature Materials* **7**, 900, doi:10.1038/nmat2291 (**2008**).

[41] H. Minemawari, T. Yamada, H. Matsui, J. Tsutsumi, S. Haas, R. Chiba, R. Kumai, T. Hasegawa. "Inkjet Printing of Single-Crystal Films". *Nature* **475**, 364, doi:10.1038/nature10313 (**2011**).

[42] H. Yan, Z. Chen, Y. Zheng, C. Newman, J. R. Quinn, F. Dotz, M. Kastler, A. Facchetti. "A High-Mobility Electron-Transporting Polymer for Printed Transistors". *Nature* **457**, 679, doi:10.1038/nature07727 (**2009**).

[43] F. Torrisi, T. Hasan, W. Wu, Z. Sun, A. Lombardo, T. S. Kulmala, G. W. Hsieh, S. Jung, F. Bonaccorso, P. J. Paul, D. Chu, A. C. Ferrari. "Inkjet-Printed Graphene Electronics". *ACS Nano* **6**, 2992, doi:10.1021/nn2044609 (**2012**).

[44] A. V. Neimark, Y. Lin, P. I. Ravikovitch, M. Thommes. "Quenched Solid Density Functional Theory and Pore Size Analysis of Micro-Mesoporous Carbons". *Carbon* **47**, 1617, doi:10.1016/j.carbon.2009.01.050 (**2009**).

[45] P. I. Ravikovitch, A. V. Neimark. "Density Functional Theory Model of Adsorption on Amorphous and Microporous Silica Materials". *Langmuir* **22**, 11171, doi:10.1021/la0616146 (**2006**).

[46] P. I. Ravikovitch, A. V. Neimark. "Density Functional Theory of Adsorption in Spherical Cavities and Pore Size Characterization of Templated Nanoporous Silicas with Cubic and Three-Dimensional Hexagonal Structures". *Langmuir* **18**, 1550, doi:10.1021/la0107594 (**2002**).

[47] M. Thommes, B. Smarsly, M. Groenewolt, P. I. Ravikovitch, A. V. Neimark. "Adsorption Hysteresis of Nitrogen and Argon in Pore Networks and Characterization of Novel Micro- and Mesoporous Silicas". *Langmuir* **22**, 756, doi:10.1021/la051686h (**2006**).

[48] Y. Waseda, E. Matsubara, K. Shinoda in *X-Ray Diffraction Crystallography*, Springer, Berlin, Heidelberg, (**2011**), pp. 107.

[49] P. Scherrer. "Bestimmung Der Größe Und Der Inneren Struktur Von Kolloidteilchen Mittels Röntgenstrahlen". *Nachrichten von der Königlichen Gesellschaft der Wissenschaften zu Göttingen, Mathematisch-Physikalische Klasse* **1918**, 98 (**1918**).

[50] M. A. Pimenta, G. Dresselhaus, M. S. Dresselhaus, L. G. Cançado, A. Jorio, R. Saito. "Studying Disorder in Graphite-Based Systems by Raman Spectroscopy". *Physical Chemistry Chemical Physics* **9**, 1276, doi:10.1039/b613962k (**2007**).

[51] A. C. Ferrari, J. Robertson. "Interpretation of Raman Spectra of Disordered and Amorphous Carbon". *Physical Review B* **61**, 14095, doi: 10.1103/PhysRevB.61.14095 (**2000**).

[52] P. Lespade, R. Al-Jishi, M. S. Dresselhaus. "Model for Raman-Scattering from Incompletely Graphitized Carbons". *Carbon* **20**, 427, doi:10.1016/0008-6223(82)90043-4 (**1982**).

[53] P. Lespade, A. Marchand, M. Couzi, F. Cruege. "Caracterisation De Materiaux Carbones Par Microspectrometrie Raman". *Carbon* **22**, 375, doi:10.1016/0008-6223(84)90009-5 (**1984**).

[54] S. Glatzel, Z. Schnepp. In-situ TEM Video of Graphitisation by Fe_3C. url:www.youtube.com/watch?v=vAOAoof5I8Y.

[55] V. N. Parmon. "Fluidization of the Active Component of Catalysts in Catalytic Formation of Carbon Assisted by Iron and Nickel Carbides". *Catalysis Letters* **42**, 195, doi:10.1007/BF00810688 (**1996**).

[56] G. Tammann. "Die Temperatur Des Beginns Innerer Diffusion in Kristallen". *Zeitschrift für Anorganische und Allgemeine Chemie* **157**, 321, doi:10.1002/zaac.19261570123 (**1926**).

[57] R. W. Dorner, D. R. Hardy, F. W. Williams, H. D. Willauer. "Heterogeneous Catalytic CO_2 Conversion to Value-Added Hydrocarbons". *Energy & Environmental Science* **3**, 884, doi:10.1039/C001514H (**2010**).

[58] A. Y. Khodakov, W. Chu, P. Fongarland. "Advances in the Development of Novel Cobalt Fischer-Tropsch Catalysts for Synthesis of Long-Chain Hydrocarbons and Clean Fuels". *Chemical Reviews* **107**, 1692, doi:10.1021/cr050972v (**2007**).

[59] H. Böhm. "New Non-Noble Metal Anode Catalysts for Acid Fuel Cells". *Nature* **227**, 483, doi:10.1038/227483a0 (**1970**).

[60] A Scopus® search for „ternary carbide(s)“ and iron and manganese or tungsten yields less than 25 results for each, all of which deal with steels or the thermodynamics of the respective system.

[61] H. Kleykamp. "Zur Thermodynamik in Den Systemen Fe-W, Fe-W-O Und Fe-W-C". *Journal of the Less Common Metals* **71**, 127, doi:10.1016/0022-5088(80)90108-3 (**1980**).

[62] M. J. G. Fait, H. J. Lunk, M. Feist, M. Schneider, J. N. Dann, T. A. Frisk. "Thermal Decomposition of Ammonium Paratungstate Tetrahydrate under Non-Reducing Conditions Characterization by Thermal Analysis, X-Ray Diffraction and Spectroscopic Methods". *Thermochimica Acta* **469**, 12, doi:10.1016/j.tca.2007.12.007 (**2008**).

[63] G. J. French, F. R. Sale. "A Re-Investigation of the Thermal Decomposition of Ammonium Paratungstate". *Journal of Materials Science* **16**, 3427, doi:10.1007/BF00586305 (**1981**).

[64] K. R. Locherer, I. P. Swainson, E. K. H. Salje. "Phase Transitions in Tungsten Trioxide at High Temperatures - A New Look". *Journal of Physics: Condensed Matter* **11**, 6737, doi:10.1088/0953-8984/11/35/312 (**1999**).

[65] J. Guo, X. Zhou, Y. Lu, X. Zhang, S. Kuang, W. Hou. "Monodisperse Spindle-Like $FeWO_4$ Nanoparticles: Controlled Hydrothermal Synthesis and Enhanced Optical Properties". *Journal of Solid State Chemistry* **196**, 550, doi:10.1016/j.jssc.2012.07.026 (**2012**).

[66] M. Gillet, R. Delamare, E. Gillet. "Growth, Structure and Electrical Properties of Tungsten Oxide Nanorods". *The European Physical Journal D* **34**, 291, doi:10.1140/epjd/e2005-00161-2 (**2005**).

[67] Unpublished work. Manuscript in preparation.

[68] Z. Chen, Z. Jiao, D. Pan, Z. Li, M. Wu, C. H. Shek, C. M. Wu, J. K. Lai. "Recent Advances in Manganese Oxide Nanocrystals: Fabrication, Characterization, and Microstructure". *Chemical Reviews* **112**, 3833, doi:10.1021/cr2004508 (**2012**).

[69] R. Cao, W. Lai, P. Du. "Catalytic Water Oxidation at Single Metal Sites". *Energy & Environmental Science* **5**, 8134, doi:10.1039/c2ee21494f (**2012**).

[70] F. Jiao, H. Frei. "Nanostructured Cobalt and Manganese Oxide Clusters as Efficient Water Oxidation Catalysts". *Energy & Environmental Science* **3**, 1018, doi:10.1039/c002074e (**2010**).

[71] C. M. Parlett, K. Wilson, A. F. Lee. "Hierarchical Porous Materials: Catalytic Applications". *Chemical Society Reviews*, doi:10.1039/c2cs35378d (**2012**).

[72] C. Perego, R. Millini. "Porous Materials in Catalysis: Challenges for Mesoporous Materials". *Chemical Society Reviews*, doi:10.1039/C2CS35244C (**2012**).

[73] B. Babakhani, D. G. Ivey. "Anodic Deposition of Manganese Oxide Electrodes with Rod-Like Structures for Application as Electrochemical Capacitors". *Journal of Power Sources* **195**, 2110, doi:10.1016/j.jpowsour.2009.10.045 (**2010**).

[74] T. Ould-Ely, D. Prieto-Centurion, A. Kumar, W. Guo, W. V. Knowles, S. Asokan, M. S. Wong, I. Rusakova, A. Lüttge, K. H. Whitmire. "Manganese(II) Oxide Nanohexapods:

Insight into Controlling the Form of Nanocrystals". *Chemistry of Materials* **18**, 1821, doi:10.1021/cm052492q (**2006**).

[75] F. Wang, H. Dai, J. Deng, G. Bai, K. Ji, Y. Liu. "Manganese Oxides with Rod-, Wire-, Tube-, and Flower-Like Morphologies: Highly Effective Catalysts for the Removal of Toluene". *Environmental Science & Technology* **46**, 4034, doi:10.1021/es204038j (**2012**).

[76] J. Park, E. Kang, C. J. Bae, J.-G. Park, H.-J. Noh, J.-Y. Kim, J.-H. Park, H. M. Park, T. Hyeon. "Synthesis, Characterization, and Magnetic Properties of Uniform-Sized Mno Nanospheres and Nanorods". *The Journal of Physical Chemistry B* **108**, 13594, doi:10.1021/jp048229e (**2004**).

[77] A Web of Knowledge™ seach for the topic yields more than 80 000 results.

[78] C.-J. Jia, F. Schüth. "Colloidal Metal Nanoparticles as a Component of Designed Catalyst". *Phys Chem Chem Phys* **13**, 2457, doi:10.1039/C0CP02680H (**2011**).

[79] C. Burda, X. Chen, R. Narayanan, M. A. El-Sayed. "Chemistry and Properties of Nanocrystals of Different Shapes". *Chemical Reviews* **105**, 1025, doi:10.1021/cr030063a (**2005**).

[80] J. Wu, P. Li, Y. T. Pan, S. Warren, X. Yin, H. Yang. "Surface Lattice-Engineered Bimetallic Nanoparticles and Their Catalytic Properties". *Chemical Society Reviews*, doi:10.1039/C2CS35189G (**2012**).

[81] F. F. Tao. "Synthesis, Catalysis, Surface Chemistry and Structure of Bimetallic Nanocatalysts". *Chemical Society Reviews*, doi:10.1039/C2CS90093A (**2012**).

[82] H. You, S. Yang, B. Ding, H. Yang. "Synthesis of Colloidal Metal and Metal Alloy Nanoparticles for Electrochemical Energy Applications". *Chemical Society Reviews*, doi:10.1039/C2CS35319A (**2012**).

[83] B. Wen, J. J. Zhao, T. J. Li. "Synthesis and Crystal Structure of N-Diamond". *International Materials Reviews* **52**, 131, doi:10.1179/174328007X160236 (**2007**).

[84] E. F. Antunes, A. O. Lobo, E. J. Corat, V. J. Trava-Airoldi, A. A. Martin, C. Veríssimo. "Comparative Study of First- and Second-Order Raman Spectra of MWCNT at Visible and Infrared Laser Excitation". *Carbon* **44**, 2202, doi:10.1016/j.carbon.2006.03.003 (**2006**).

[85] V. Barbarossa, F. Galluzzi, R. Tomaciello, A. Zanobi. "Raman Spectra of Microcrystalline Graphite and a-C:H Films Excited at 1064 nm". *Chemical Physics Letters* **185**, 53, doi:10.1016/0009-2614(91)80138-N (**1991**).

[86] A. C. Ferrari, J. Robertson. "Resonant Raman Spectroscopy of Disordered, Amorphous, and Diamondlike Carbon". *Physical Review B* **64**, doi:10.1103/PhysRevB.64.075414 (**2001**).

[87] I. Lisiecki, A. Filankembo, H. Sack-Kongehl, K. Weiss, M. P. Pileni, J. Urban. "Structural Investigations of Copper Nanorods by High-Resolution TEM". *Physical Review B* **61**, 4968, doi:10.1103/PhysRevB.61.4968 (**2000**).

[88] C. Ehrhardt, M. Gjikaj, W. Brockner. "Thermal Decomposition of Cobalt Nitrato Compounds: Preparation of Anhydrous Cobalt(II)Nitrate and Its Characterisation by Infrared and Raman Spectra". *Thermochimica Acta* **432**, 36, doi:10.1016/j.tca.2005.04.010 (**2005**).

[89] T. J. W. De Bruijn, W. A. De Jong, P. J. Van Den Berg. "Thermal Decomposition of Aqueous Manganese Nitrate Solutions and Anhydrous Manganese Nitrate. Part 1. Mechanism". *Thermochimica Acta* **45**, 265, doi:10.1016/0040-6031(81)85087-3 (**1981**).

[90] W. Brockner, C. Ehrhardt, M. Gjikaj. "Thermal Decomposition of Nickel Nitrate Hexahydrate, $Ni(NO_3)_2 \cdot 6H_2O$, in Comparison to $Co(NO_3)_2 \cdot 6H_2O$ and $Ca(NO_3)_2 \cdot 4H_2O$". *Thermochimica Acta* **456**, 64, doi:10.1016/j.tca.2007.01.031 (**2007**).

[91] T. Öhlund, J. Örtegren, S. Forsberg, H.-E. Nilsson. "Paper Surfaces for Metal Nanoparticle Inkjet Printing". *Applied Surface Science* **259**, 731, doi:10.1016/j.apsusc.2012.07.112 (**2012**).

[92] P. T. Anastas, W. J. C. *Green Chemistry: Theory and Practice*, Oxford University Press, New York, (**1998**).

[93] M. Romero, A. Steinfeld. "Concentrating Solar Thermal Power and Thermochemical Fuels". *Energy & Environmental Science* **5**, 9234, doi:10.1039/C2EE21275G (**2012**).

[94] S. Roy, V. Jain, R. Bajpai, P. Ghosh, A. S. Pente, B. P. Singh, D. S. Misra. "Formation of Carbon Nanotube Bucky Paper and Feasibility Study for Filtration at the Nano and Molecular Scale". *The Journal of Physical Chemistry C* **116**, 19025, doi:10.1021/jp305677h (**2012**).

[95] A. J. Ragauskas, C. K. Williams, B. H. Davison, G. Britovsek, J. Cairney, C. A. Eckert, W. J. Frederick, Jr., J. P. Hallett, D. J. Leak, C. L. Liotta, J. R. Mielenz, R. Murphy, R. Templer, T. Tschaplinski. "The Path Forward for Biofuels and Biomaterials". *Science* **311**, 484, doi:10.1126/science.1114736 (**2006**).

X. APPENDIX

LIST OF ABBREVIATIONS

BET	*Brunauer-Emmett-Teller*
CDC	carbide derived carbons
CFP	cellulose filter paper
DLC	diamond-like carbon
CMYK	cyan, magenta, yellow, key (colour system)
CNC	computer numerical control
DFT	density functional theory
EDX	energy-dispersive X-ray spectroscopy
FWHM	full width at half maximum
HRSEM	high resolution scanning electron microscopy
HRTEM	high resolution transmission electron microscopy
MCC	micro-crystalline cellulose
NCC	nano-crystalline cellulose
$SA_{BET,\ app.}$	apparent BET surface area
SEM	scanning electron microscopy
TGA	thermo-gravimetric analysis
TEM	transmission electron microscopy
UM	ultra-microtome(d)
XRD	(wide angle) X-ray diffraction

CHEMICALS AND ANALYSIS TECHNIQUES

Chemicals

Microcrystalline cellulose, iron(III) nitrate nonahydrate, copper(II) nitrate hemipentahydrate (98%), manganese(II) acetate tetrahydrate (≥ 99 %) and Nickel(II) nitrate hexahydrate (≥ 99 %) were purchased from Sigma Aldrich. Iron(II) acetate (97%) and ammonium metatungstate hydrate (≥ 99 %) were bought from ABCR. Manganese(II) nitrate tetrahydrate (98%) was acquired from Alfa Aesar. Copper. Cobalt(II) nitrate hexahydrate (99 %) as obtained from Strem Chemicals. The laboratory grade filter paper was made by Macherey-Nagel. All chemicals were used without further purification.

HR SEM

The high resolution SEM micrographs were taken on a JEOL JSM-7001F field emission scanning electron microscope with an Oxford energy dispersive detector.

HR TEM

High resolution TEM images were taken on a JEOL JEM-2100F 200kV Field Emission Transmission Electron Microscope equipped with STEM (dark field imaging) and STEM-EDS and on a Philips CM200 FEG (Field Emission Gun), operated at an acceleration voltage of 200 kV.

in-situ TEM

The *in-situ* TEM videos were taken on a JEOL JEM-2000FXII with heating holder and video camera.

Ink-Jet Printing

Initial printing experiments were conducted with three different commercial printers: HP DeskJet 710C™, HP Deskjet 5900C™ and an Epson™ Stylus S22. All three printers gave satisfactory printing results. Since this was the case the least expensive printer (Epson™ Stylus S22, costs approximately 25 €) was employed to conduct the experiments.

Nitrogen Sorption

Nitrogen sorption experiments were done with a Quantachrome Quadrasorb at liquid nitrogen temperature, and data analysis was performed by Quantachrome QuadraWin software (version 5.05). All the samples were degassed at 150 °C for 20 hours before measurements.

Optical Microscopy

Optical microscope images were taken with a Keyence VHX-100K digital microscope equipped with a VH-Z100 and a VH-Z500 lens.

Photographs

Photographs were taken with a Sony SLT-A55 equipped with a SAL-1855 lens.

Raman

For Raman spectroscopy, a 532 nm Nd:YAG laser (WITec, Ulm, Germany) beam was focused down to a micrometer size spot on the sample through a confocal Raman microscope (CRM300, WITec, Ulm, Germany) equipped with piezo-scanner (P-500, Physik Instrumente, Karlsruhe, Germany). The spectra were acquired using an air-cooled CCD detector (DU401-BV, Andor, Belfast, UK) behind a grating (600 $g \cdot mm^{-1}$) spectrograph (UHTS 300, WITec, Ulm, Germany). The ScanCtrlSpectroscopyPlus (version 2.02, Witec) was used for measurement setup and data processing.

Infrared Raman microspectroscopy, was performed by focussing a continuous laser beam down to a micrometer size spot on the sample through a confocal Raman microscope (CRM200, WITec, Ulm, Germany) equipped with piezo-scanner (P-500, Physik Instrumente, Karlsruhe, Germany). The diode pumped linearly-polarized 785 nm near infra-red (NIR) laser excitation (Toptica Photonics AG, Graefelfing, Germany) was used in combination with × 20 (Nikon, NA = 0.4) microscope objective. The spectra were acquired using an air-cooled CCD (PI-MAX, Princeton Instruments Inc., Trenton, NJ, USA) behind a grating (300 $g \cdot mm^{-1}$) spectrograph (Acton, Princeton Instruments Inc., Trenton, NJ, USA) with a spectral resolution of 6 cm^{-1}. The ScanCtrlSpectroscopyPlus (version 1.38, Witec) was used for measurement setup and spectra processing.

SEM

SEM was performed on a LEO 1550 Gemini instrument. The samples were loaded on carbon coated aluminium stubs and measured without any coating since they were conductive. The reference fibres were coated by sputtering an Au/Pd alloy prior to imaging.

TEM

TEM images were taken using a Zeiss EM 912Ω operated at an acceleration voltage of 120 kV. Samples were Embedded in LR White Resin (Medium Grade, Agar Scientific) and cut with a Leica Ultracut UTC to yield ultramicrotomes of the samples. An ultramicrotome cut was put on a 400 mesh carbon-coated copper grid.

X. Appendix

TGA-MS

Thermo gravimetric analysis was performed with a Netzsch TG-209 F1 Libra and a connected Pfeiffer ThermoStar GSD301-T2 mass spectrometer.

XRD

XRD measurements were performed on a Bruker D8 diffractometer using Cu-Kα radiation (λ = 0.154 nm) and a scintillation counter (KeveX Detector). All reference patterns depicted were taken from the ICDD PDF-4+ database (2011 edition).

ADDITIONAL FIGURES

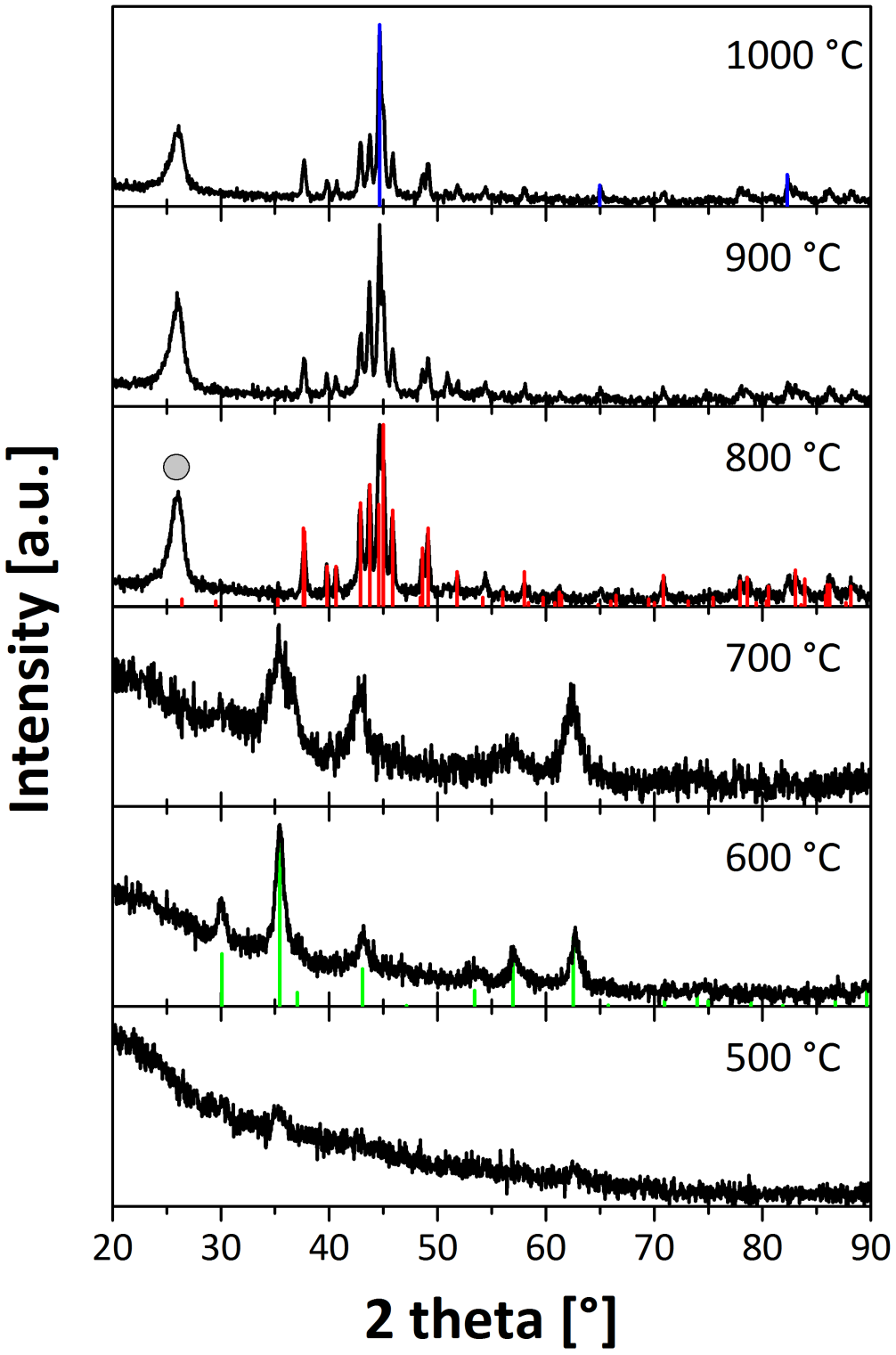

Appendix Figure 1: Enlarged version of **Figure 6 B**. The inserted reference patterns correspond to: Green: Fe_3O_4 (ICDD 01-077-1545), Red: Fe_3C (ICDD 00-035-0772), Blue: Fe^0 (ICDD 04-007-9453) and the grey circle at 26° 2 theta is attributed to graphitic carbon (ICDD 04-015-2407).

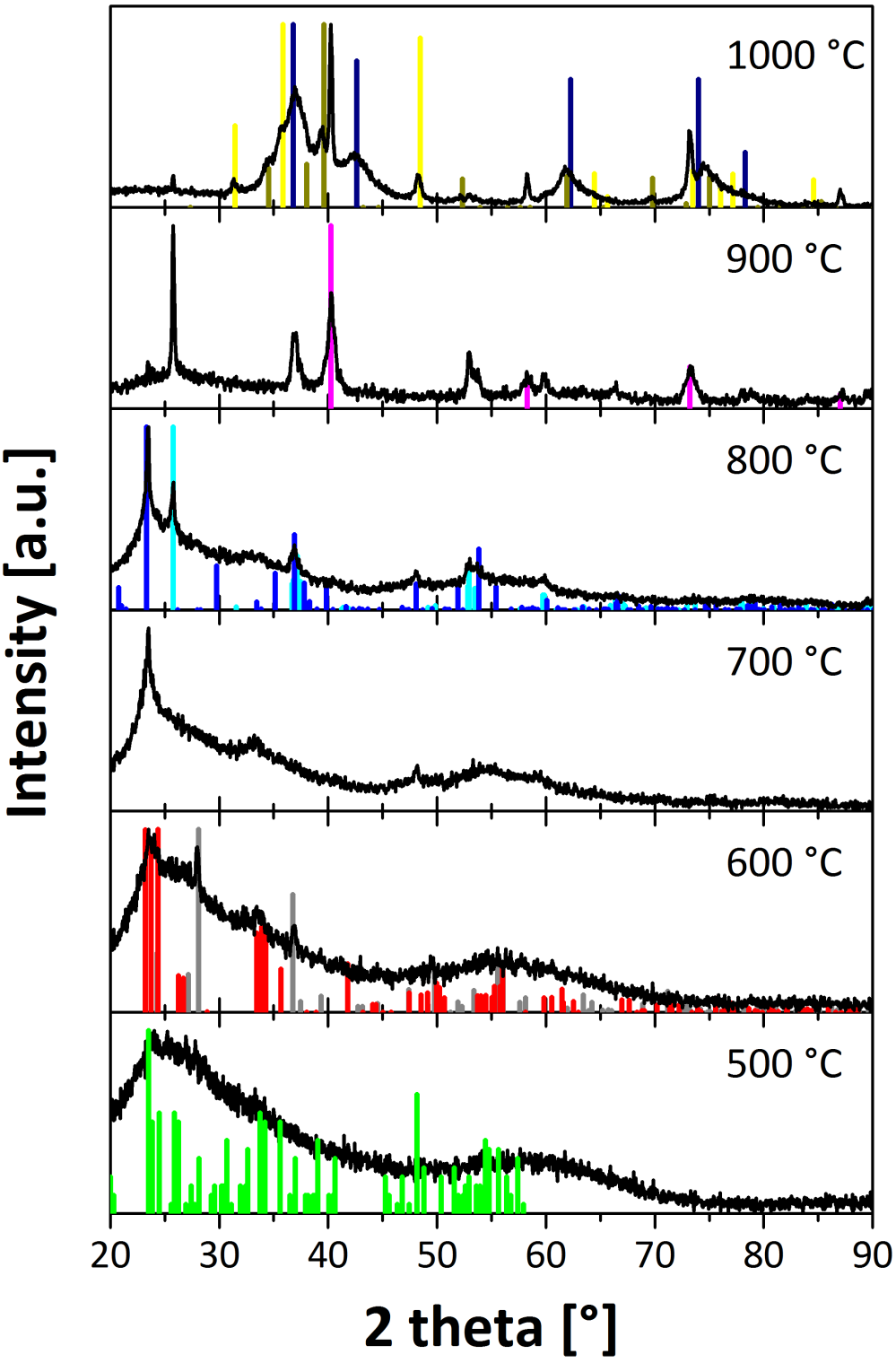

Appendix Figure 2: Enlarged version of **Figure 14 A**. The reference patterns marked are: Green: $W_{18}O_{49}$ (ICDD 00-005-0392), Red: WO_3, triclinic (ICDD 01-073-6498), Grey: WO_3, hexagonal (ICDD 04-007-2322), Blue: WO_2, orthorhombic (ICDD 04-007-0872), Cyan: WO_2, monoclinic (ICDD 04-005-5105), Magenta: W^0 (ICDD 00-004-0806), Yellow: WC (ICDD 01-077-4389), Dark Yellow: W_2C (ICDD 04-014-5679) and Navy: $W_2(C,O)$ (ICDD 00-022-0959).

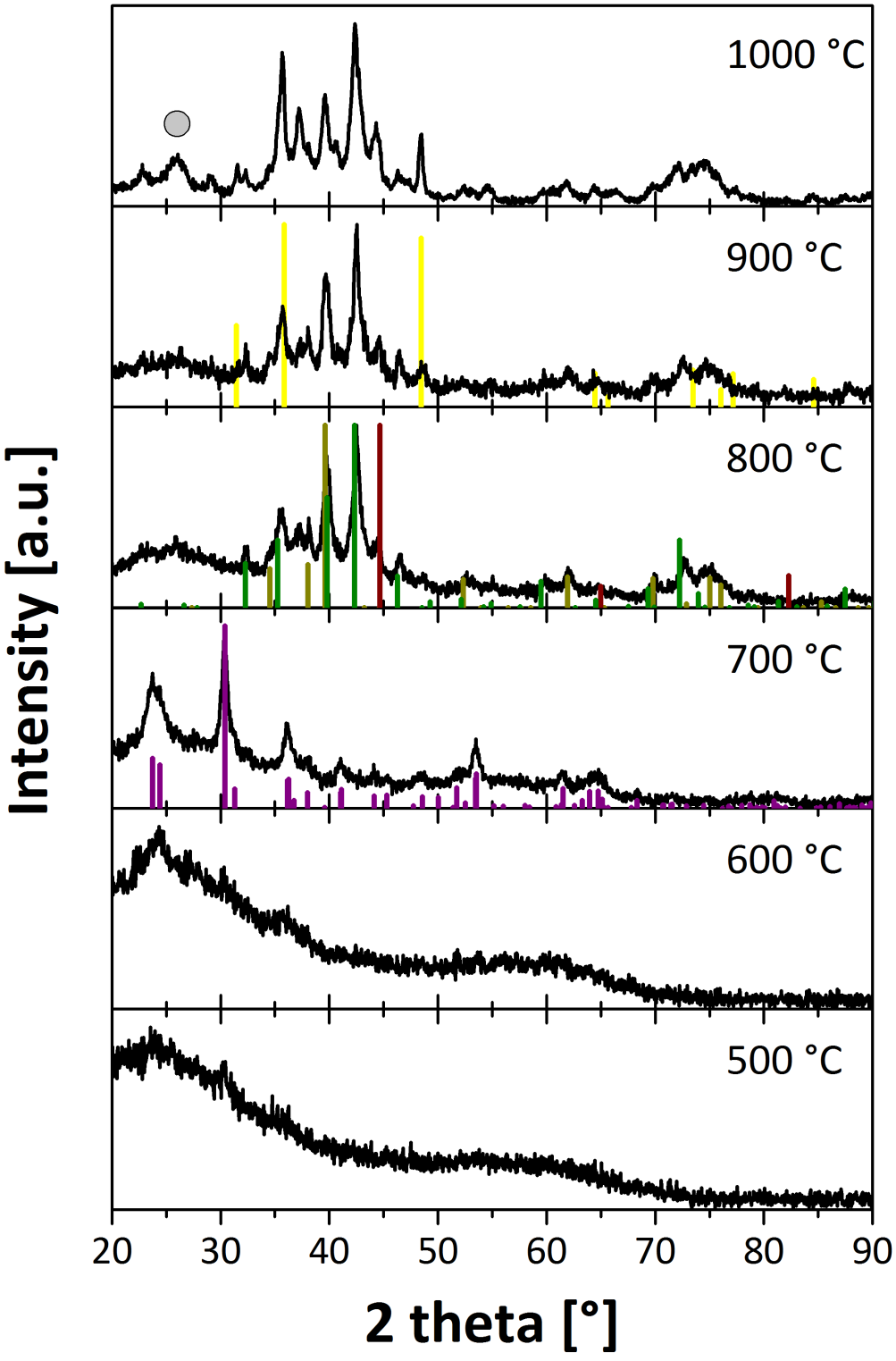

Appendix Figure 3: Enlarged version of **Figure 14 B**. The reference patterns marked are: Purple: $FeWO_4$ (ICDD 04-007-5882), Wine: Fe^0 (ICDD 04-014-0360), Olive: Fe_3W_3C (ICDD 01-078-1990), Yellow: WC (ICDD 01-077-4389) and the grey circle at 26° 2 theta is attributed to graphitic carbon (ICDD 04-015-2407).

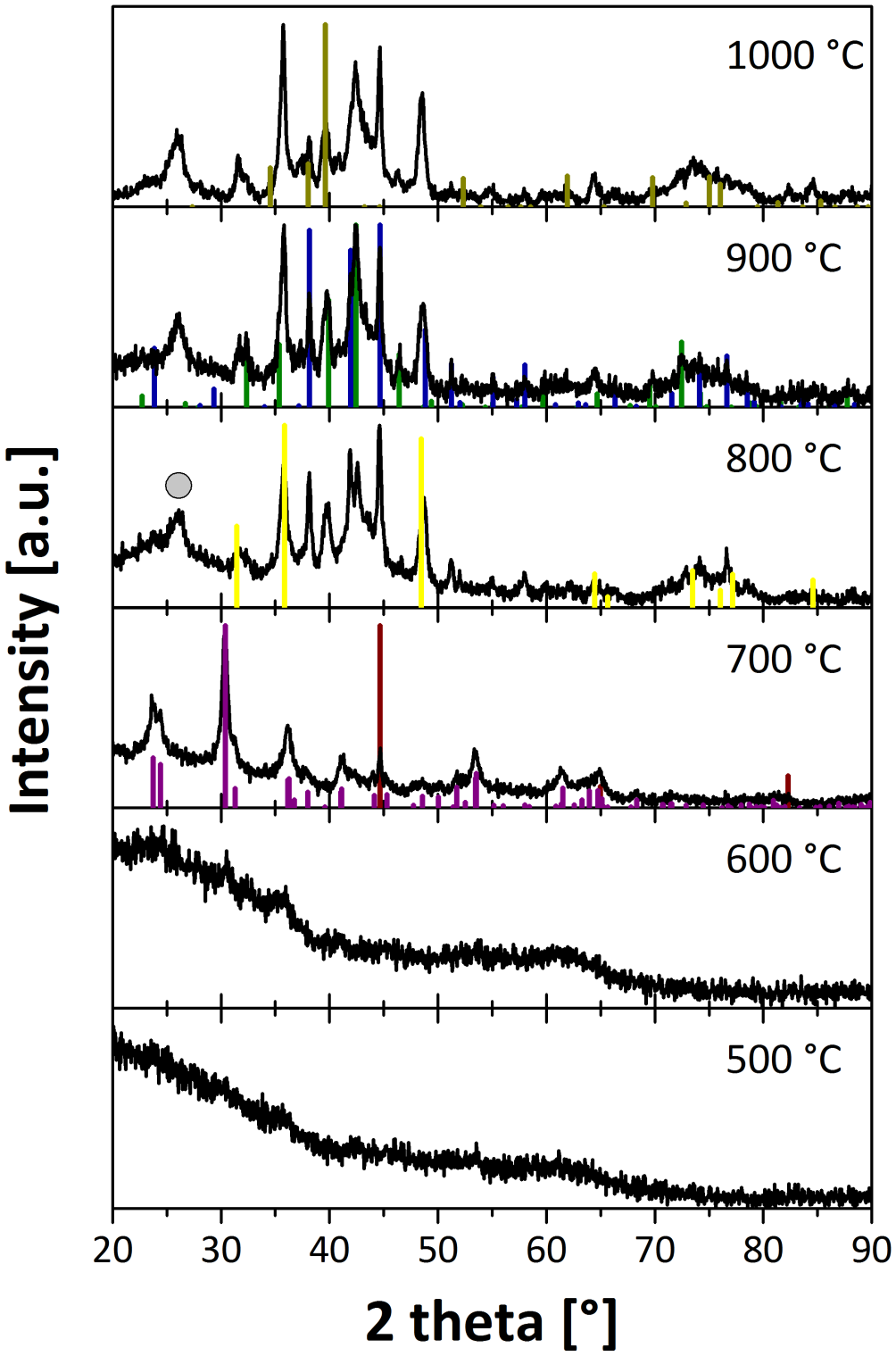

Appendix Figure 4: Enlarged version of **Figure 14 C**. The reference patterns marked are: Dark Yellow: W_2C (ICDD 04-014-5679), Royal Blue: $W_2Fe_{21}C_6$ (ICDD 04-010-7445), Olive: Fe_3W_3C (ICDD 01-078-1990), Yellow: WC (ICDD 01-077-4389), Wine: Fe^0 (ICDD 04-014-0360), Purple: $FeWO_4$ (ICDD 04-007-5882), and the grey circle at 26° 2 theta is attributed to graphitic carbon (ICDD 04-015-2407).

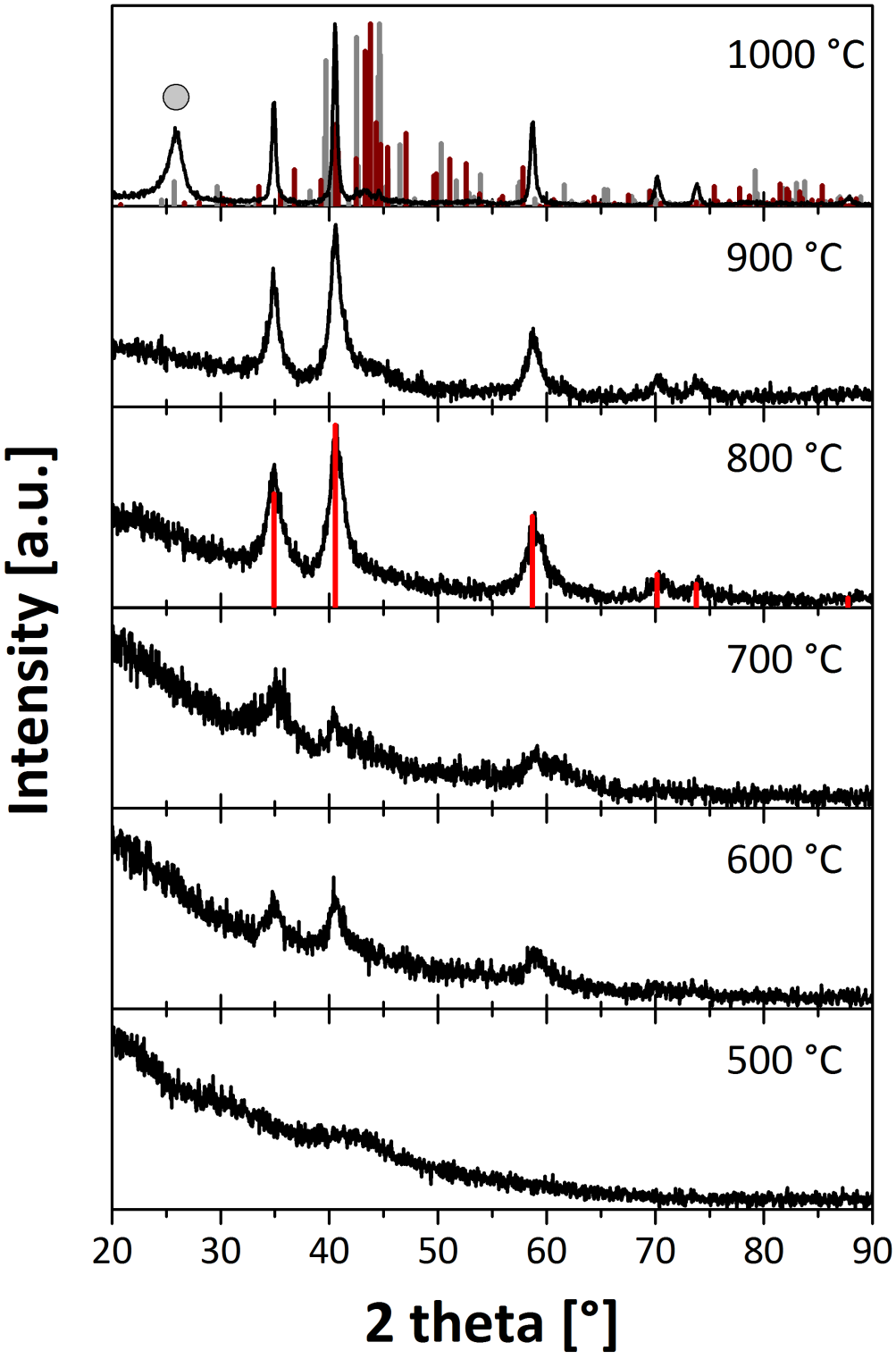

Appendix Figure 5: Enlarged version of **Figure 19 A**. The reference patterns marked are: Red: MnO (ICDD 04-005-4310), Grey: Mn_7C_3 (ICDD 04-007-1048), Wine: Mn_5C_2 (ICDD 04-007-1125) and the grey circle at 26° 2 theta is attributed to graphitic carbon (ICDD 04-015-2407).

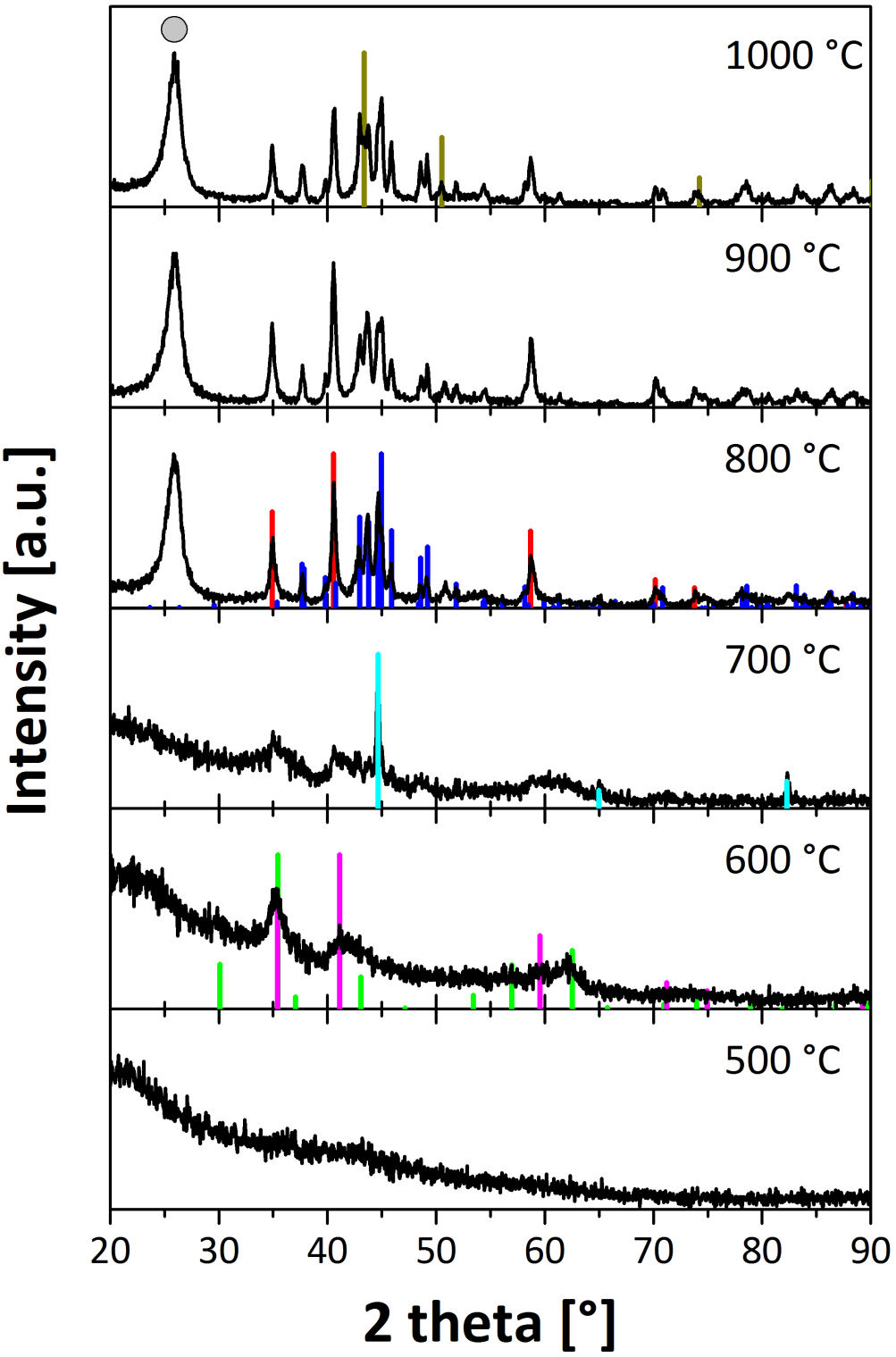

Appendix Figure 6: Enlarged version of **Figure 19 B**. The reference patterns marked are: Blue: $Mn_{0.75}Fe_{2.25}C$ (ICDD 04-002-8999), Red: MnO (ICDD 04-005-4310), Magenta: $Mn_{0.5}Fe_{0.5}O$ (ICDD 04-005-9719), Green: Fe_3O_4 (ICDD 04-015-3102), Dark Yellow: $FeN_{0.0589}$ (ICDD 01-075-2130), Cyan: Fe^0 (ICDD 04-014-0360) and the grey circle at 26° 2 theta is attributed to graphitic carbon (ICDD 04-015-2407).

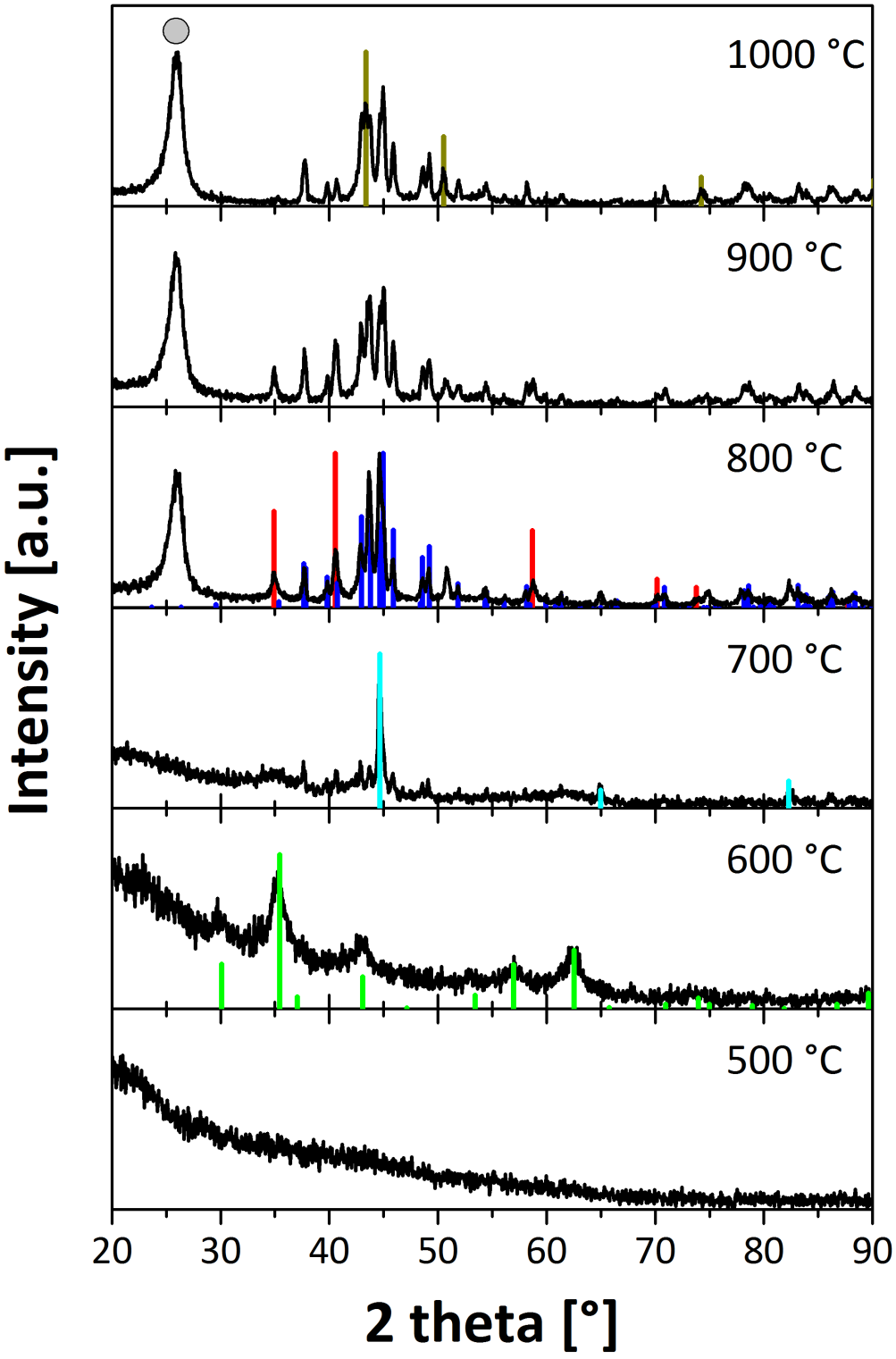

Appendix Figure 7: Enlarged version of **Figure 19 A**. The reference patterns marked are: Blue: $Mn_{0.75}Fe_{2.25}C$ (ICDD 04-002-8999), Red: MnO (ICDD 04-005-4310), Green: Fe_3O_4 (ICDD 04-015-3102), Dark Yellow: $FeN_{0.0589}$ (ICDD 01-075-2130), Cyan: Fe^0 (ICDD 04-014-0360) and the grey circle at 26° 2 theta is attributed to graphitic carbon (ICDD 04-015-2407).

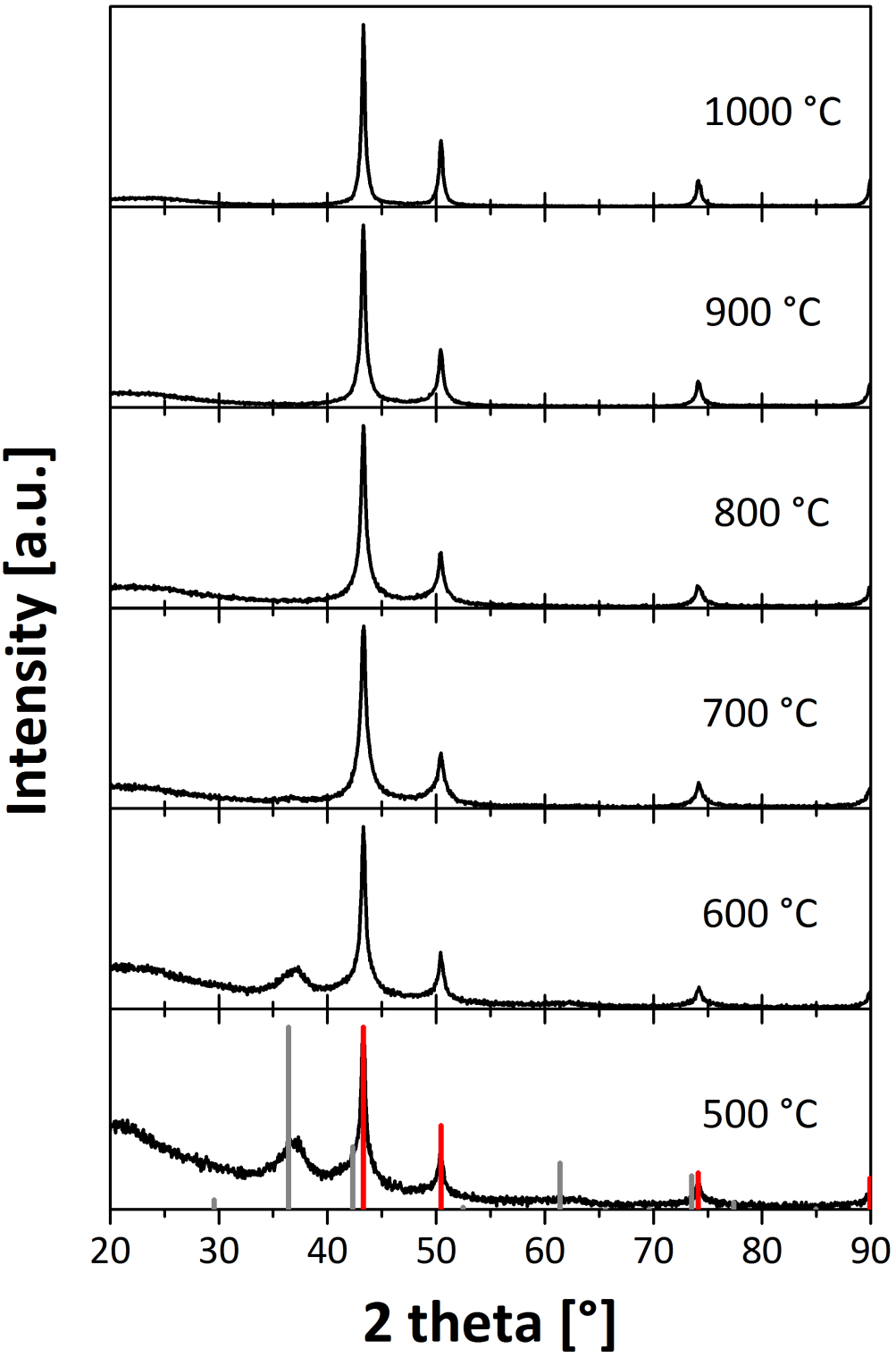

Appendix Figure 8: Enlarged version of **Figure 27 A**. The reference patterns marked are: Grey: Cu_2O (ICDD 04-007-9767) and Red: Cu^0 (ICDD 00-004-0836.

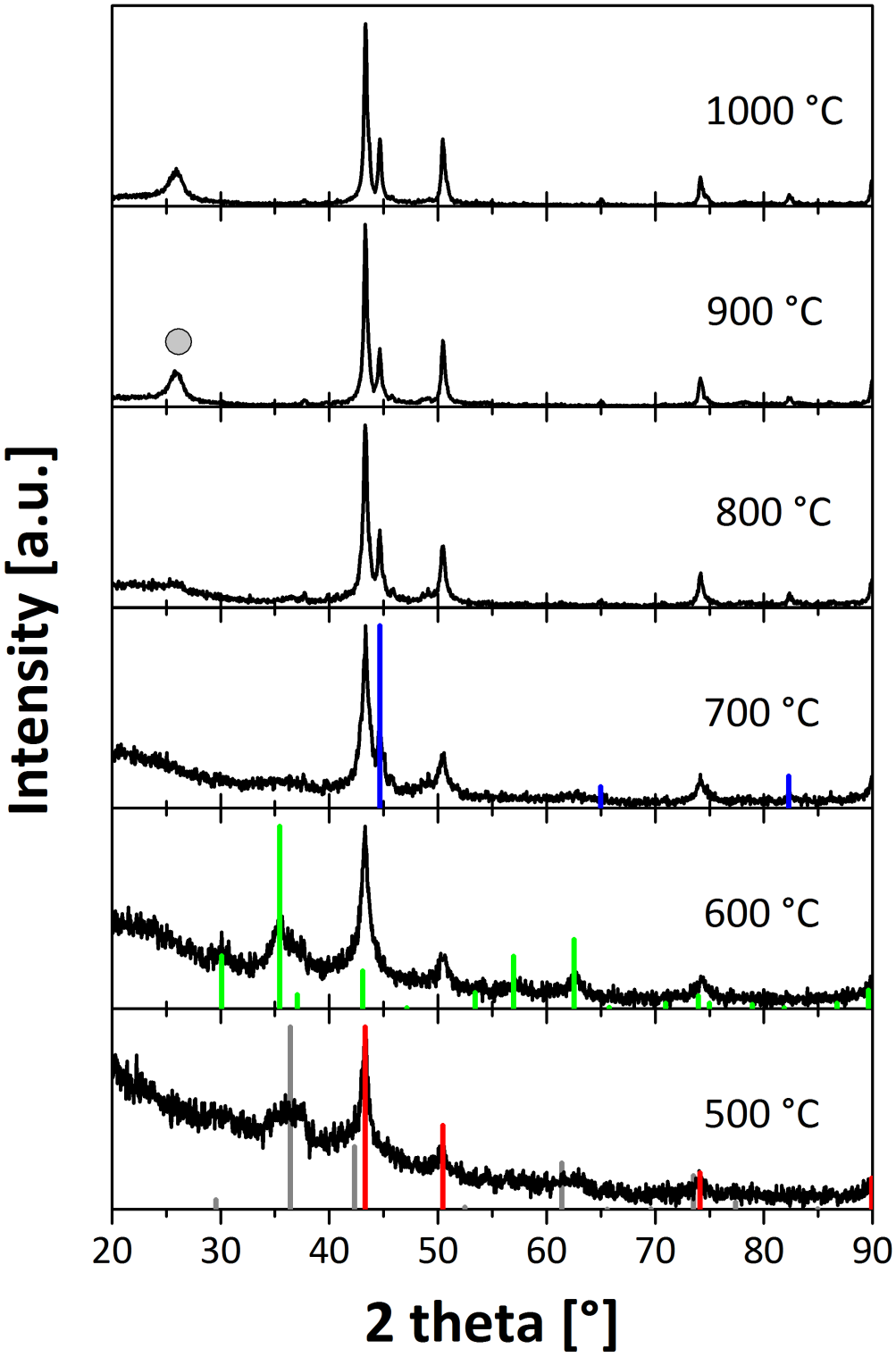

Appendix Figure 9: Enlarged version of **Figure 27 B**. The reference patterns marked are: Grey: Cu_2O (ICDD 04-007-9767), Red: Cu^0 (ICDD 00-004-0836), Green: Fe_3O_4 (ICDD 04-015-3102), Blue: Fe^0 (ICDD 04-014-0360) and the grey circle at 26° 2 theta is attributed to graphitic carbon (ICDD 04-015-2407).

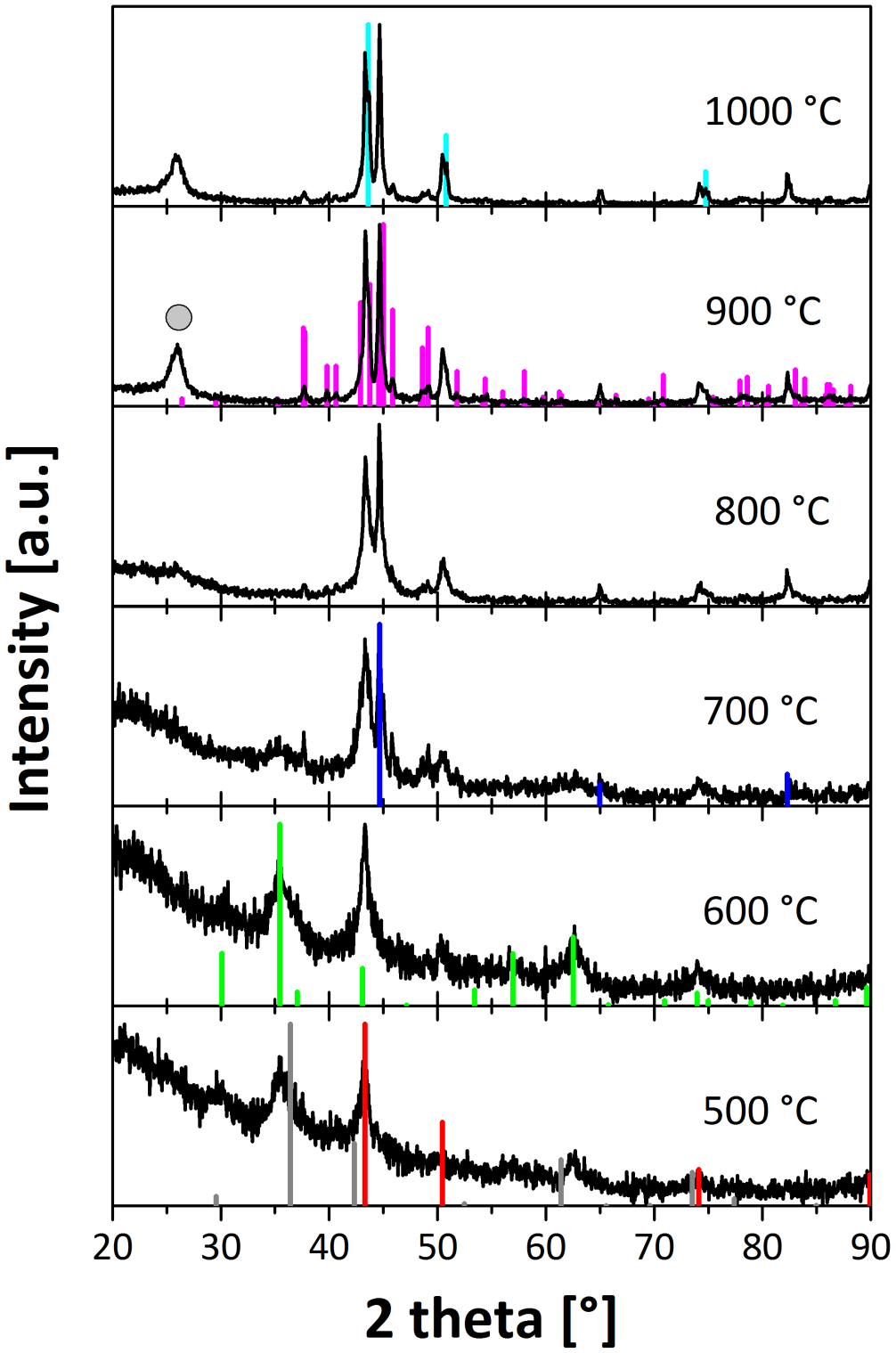

Appendix Figure 10: Enlarged version of **Figure 27 C**. The reference patterns marked are: Grey: Cu_2O (ICDD 04-007-9767), Red: Cu^0 (ICDD 00-004-0836), Green: Fe_3O_4 (ICDD 04-015-3102), Blue: Fe^0 (ICDD 04-014-0360), Magenta: Fe_3C (ICDD 00-035-0772), Cyan: Diamond-Like Carbon (ICDD 00-060-0053) and the grey circle at 26° 2 theta is attributed to graphitic carbon (ICDD 04-015-2407).

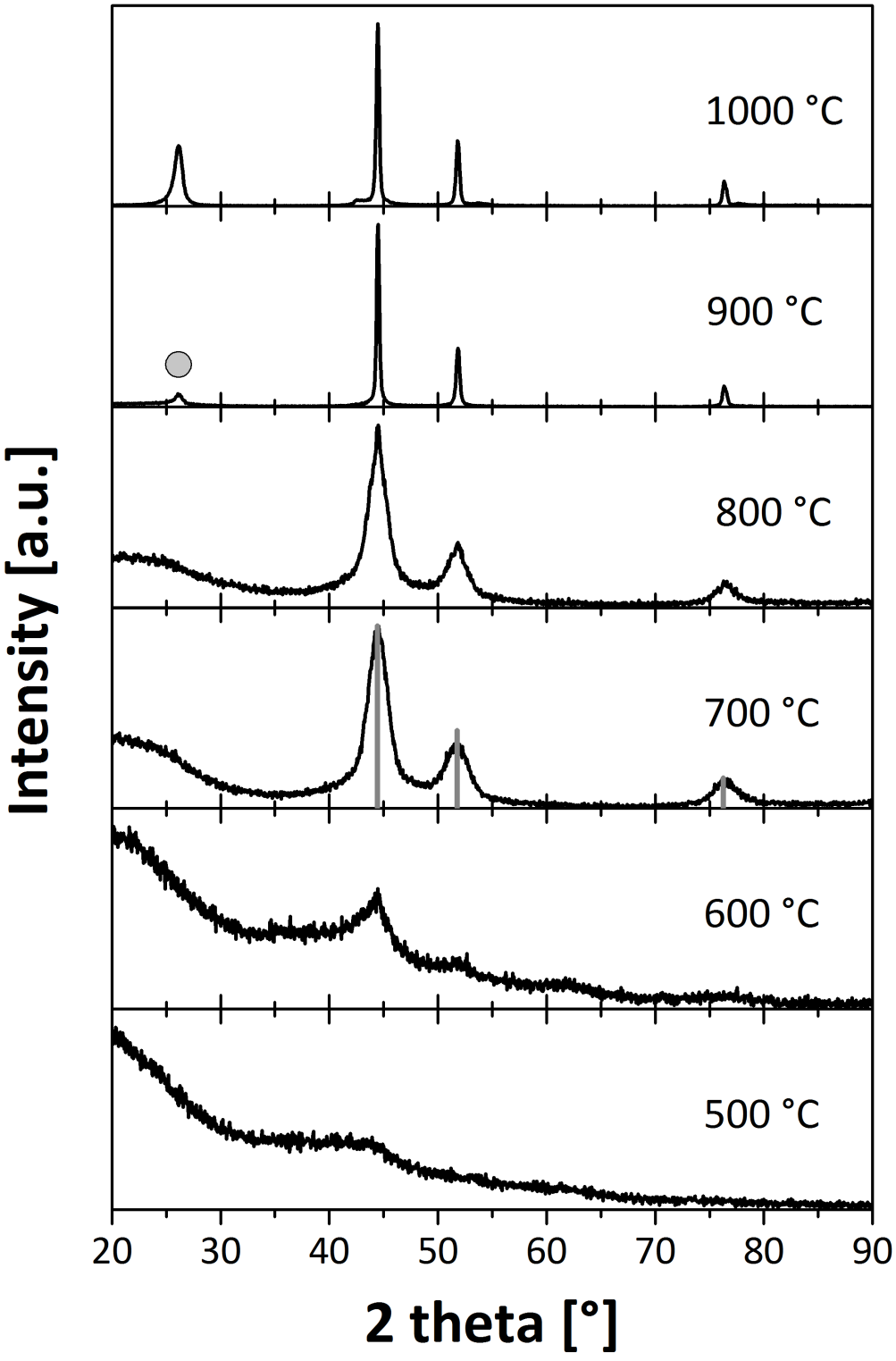

Appendix Figure 11: Enlarged version of **Figure 35 A**. The reference patterns marked are: Grey: Ni^0 (ICDD 04-010-6148) and the grey circle at 26° 2 theta is attributed to graphitic carbon (ICDD 04-015-2407).

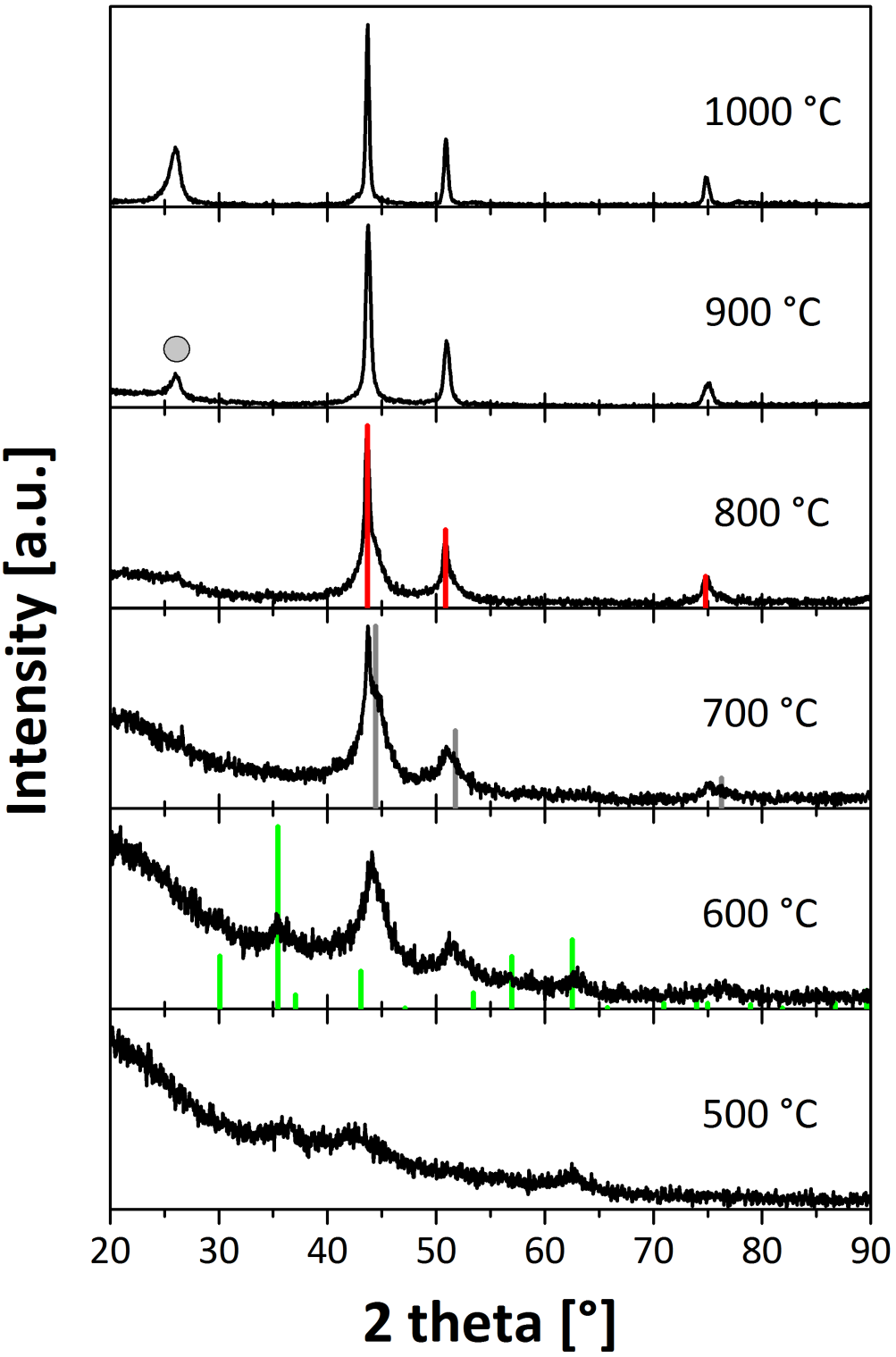

Appendix Figure 12: Enlarged version of **Figure 35 B**. The reference patterns marked are: Grey: Ni^0 (ICDD 04-010-6148), Red: $Ni_{0.5}Fe_{0.5}$ (ICDD 04-003-3531), Green: Fe_3O_4: (ICDD 04-015-3102) and the grey circle at 26° 2 theta is attributed to graphitic carbon (ICDD 04-015-2407).

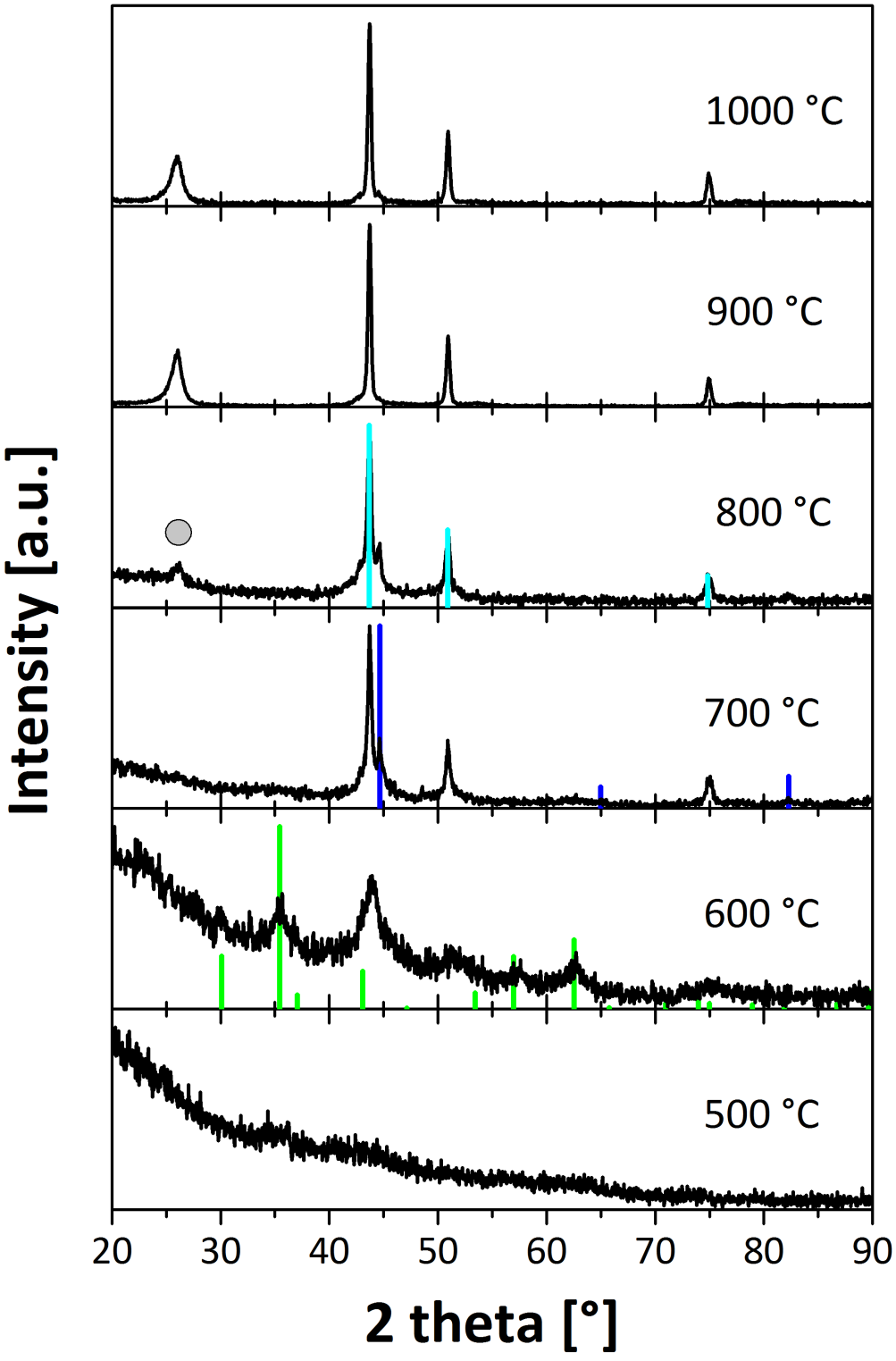

Appendix Figure 13: Enlarged version of **Figure 35 C**. The reference patterns marked are: Green: Fe_3O_4: (ICDD 04-015-3102), Blue: Fe^0 (ICDD 04-014-0360), Cyan: $Ni_{0.32}Fe_{0.68}$ (ICDD 04-002-1863) and the grey circle at 26° 2 theta is attributed to graphitic carbon (ICDD 04-015-2407).

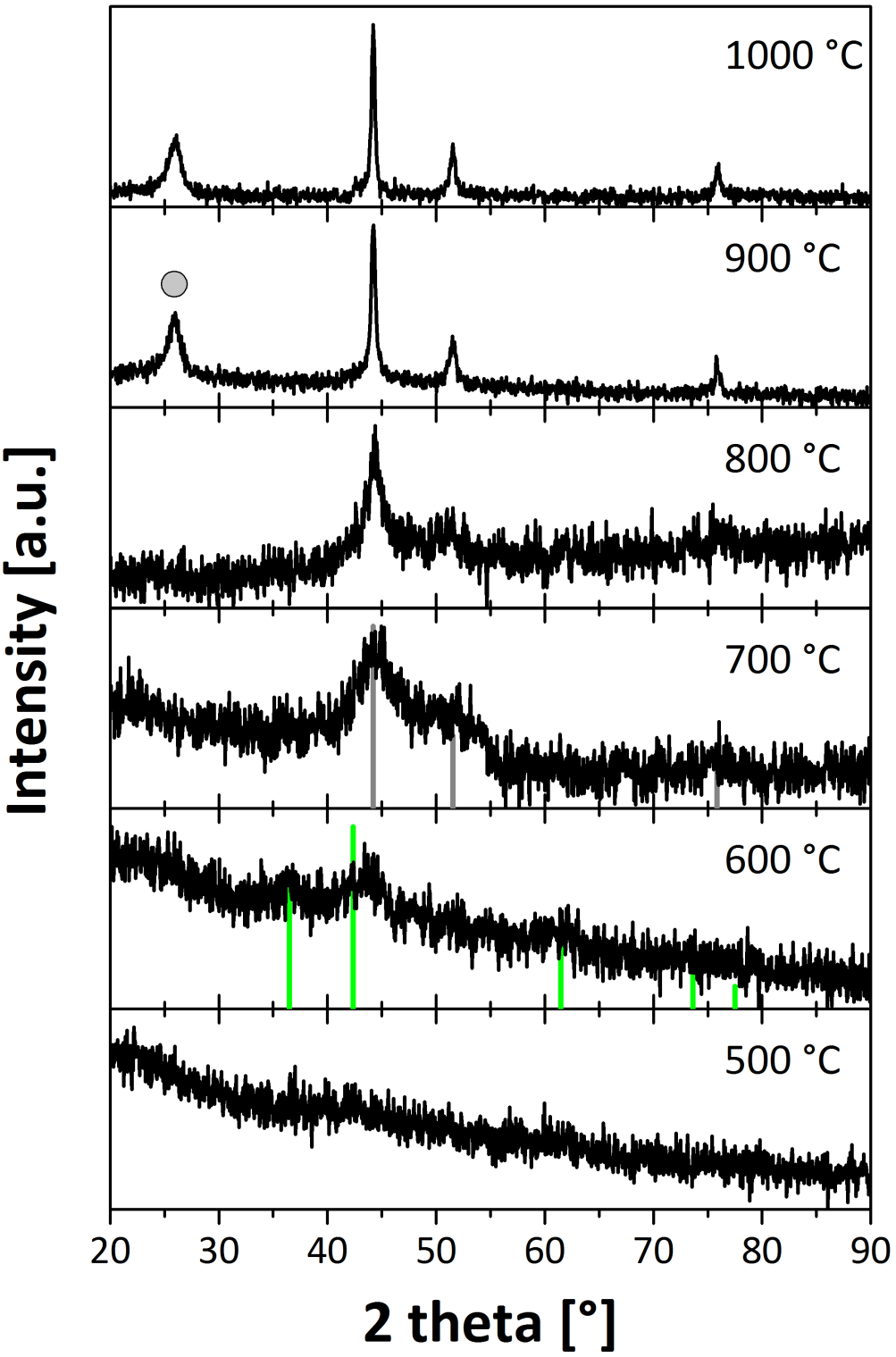

Appendix Figure 14: Enlarged version of **Figure 42 A**. The reference patterns marked are: Grey: Co^0 (ICDD 00-015-0806), Green: CoO (ICDD 01-071-1178) and the grey circle at 26° 2 theta is attributed to graphitic carbon (ICDD 04-015-2407).

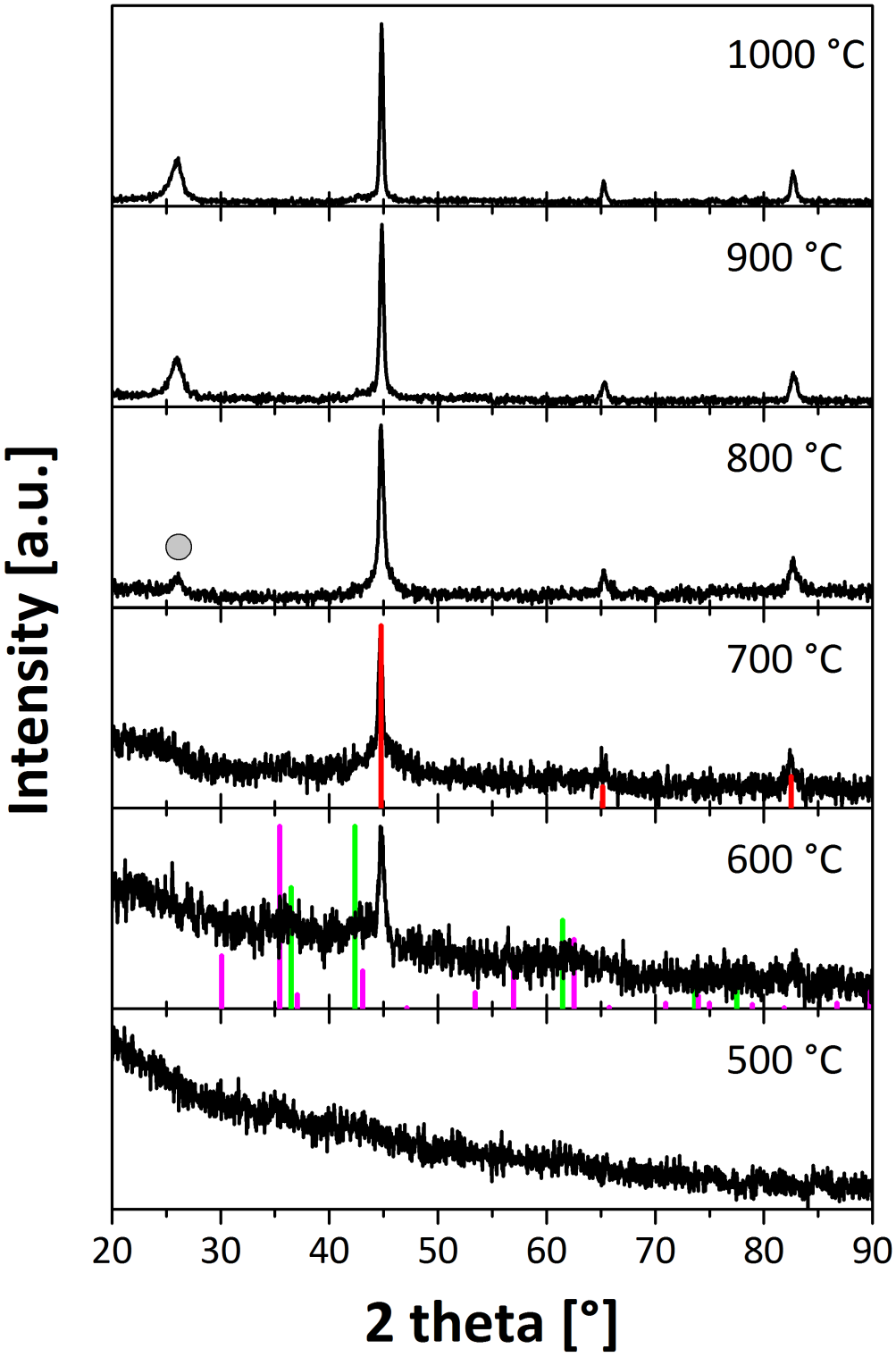

Appendix Figure 15: Enlarged version of **Figure 42 B**. The reference patterns marked are: Green: CoO (ICDD 01-071-1178), Red: CoFe (ICDD 04-014-0310), Magenta: Fe_3O_4 (ICDD 04-015-3102) and the grey circle at 26° 2 theta is attributed to graphitic carbon (ICDD 04-015-2407).

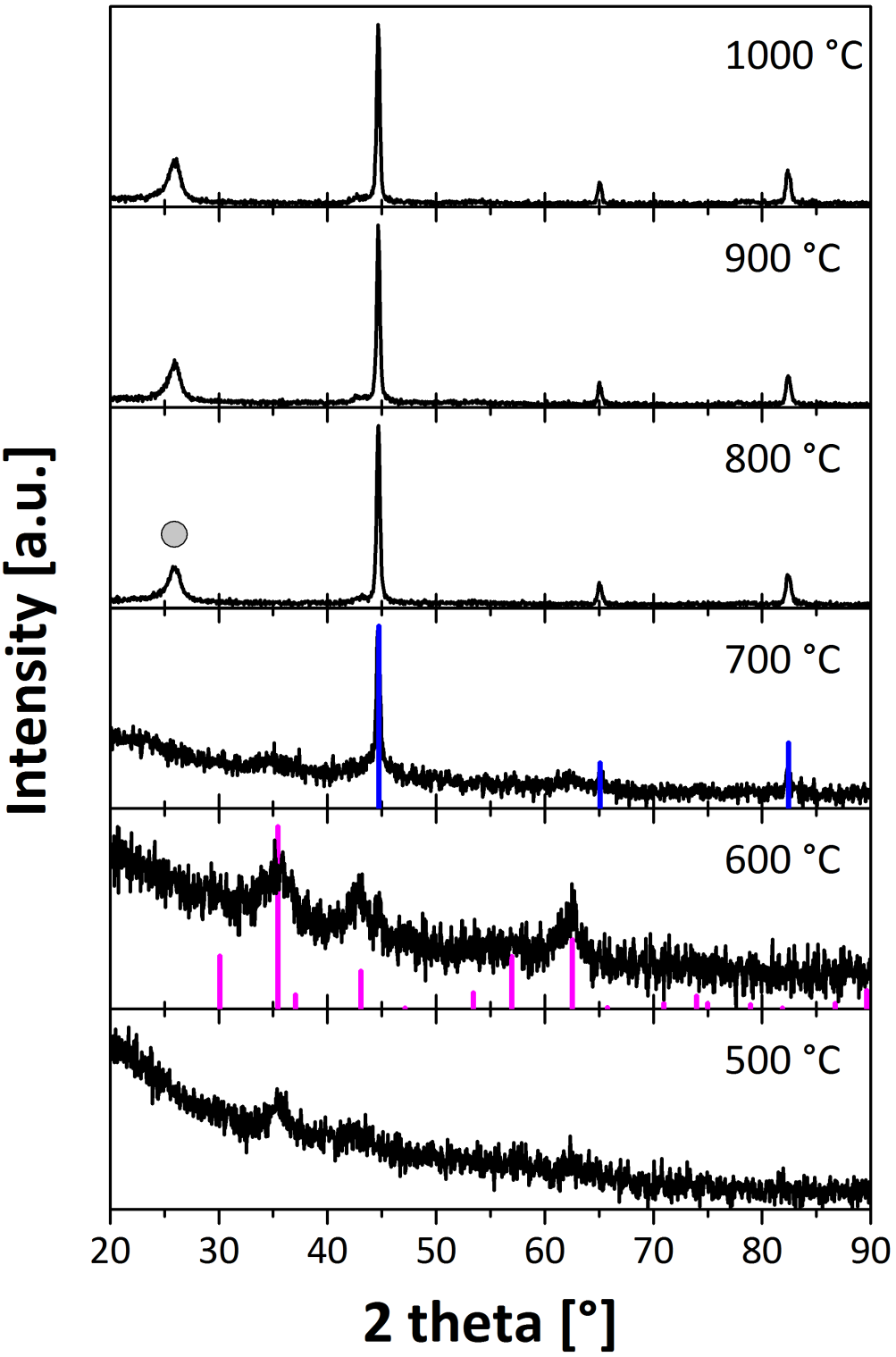

Appendix Figure 16: Enlarged version of **Figure 42 C**. The reference patterns marked are: Magenta: Fe_3O_4 (ICDD 04-015-3102), Blue: Co_3Fe_7 (ICDD 00-048-1817) and the grey circle at 26° 2 theta is attributed to graphitic carbon (ICDD 04-015-2407).

XI. ACKNOWLEDGMENTS

Like a good movie ends with the credits I should like to finish with thanking all the people that have in one way or another contributed to the making of this work.

I would like to sincerely thank Prof. Markus Antonietti and Dr. Cristina Giordano for their help and guidance and for giving me the opportunity to work at one of the acclaimed Max Planck Institutes among not only brilliant scientists but people that, after two and a half exciting years, I consider dear friends.

Ms. Rona Pitschke and Ms. Heike Runge are thanked for cutting countless microtomes and performing the TEM measurements. I would also like to thank Sylvia Pirok and Ursula Lubhan for elemental and TG analysis. Special thanks go to Ms. Ingrid Zenke for all her patience and her never ending willingness to introduce me to the secrets of XRD analysis in general and the D8 in particular. Furthermore, I would like to thank Dr. Xiaofeng Liu for his help and suggestions regarding the printing of SiC nanoparticles and Dr. Klaus Kiefer and Dr. Konrad Siemensmeyer for giving me the opportunity to work at the Helmholtz Centrum Berlin-Wannsee and teaching me everything I never knew about SQUIDs and magnetic measurements. Sincere thanks go to Hiro and Debora for their suggestions regarding this manuscript and for putting me back on track when my sentences became too complicated and even encompassed a whole paragraph ;). Moreover I would like to thank my intern Sabine Eisold for her enthusiasm and willingness to prepare “just one more” batch of nanoparticles. Especially for producing all the copper related samples presented in this work. For restlessly taking hundreds of SEM images and always being there with a helping hand and a supporting word I want to thank Katharina Otte. I am deeply thankful for Zoë Schnepp’s undying passion for science and teaching; it has been a wonderful experience working with you and of course thanks a lot performing the *in-situ* TEM measurements ma’am. Speedy-Fonzales is thanked for showing me the true meaning of restlessness and for many fun hours with the electro-spinning; you’re the MAN! My thanks also go to Regina Rothe for all the fun chats and telling me more about Norway than I ever thought there was to learn. I want to thank my office mate Stanzi for her cheerful and kind nature, for letting me win at kicker, for all the good laughs we had and for just being there; alles wird gut! I also thank the Stephs (yes, both of you) for more WTF-moments than I ever cared to have – you guys are great, I’ll miss you a lot!

I want to thank all my other dear friends at the institute: Regina H (Autsch…), Kraupner! & Kopetzki, Bet-tiny (9gag anyone?!), Nina, Tim-Patrick “wie-heute-mal-ohne-Krücken?” Fellinger, the illustrious Dr. Robin White, Camillo, Sebastian, Davide, Filipe, Dasha (Ma’am), Britta, Flo (Wer nix wird wird Wirt, ne?), Helmut, Fix & Berg and the BM Kicker-Crew and many more for scientific discussions and, more importantly,

for so many non-scientific fun hours! Special thanks go to C.B. for taking care of me in times of need.

I am indebted to so many people for making my days and nights that much fun and the past years the experience of a life time, that I have probably forgotten to mention some of you, but I wholeheartedly thank each and every one of you none the less; it's been an honour meeting you.

Meiner Familie möchte für ihre Geduld, ihr Verständnis und vor allem ihre Liebe und Unterstützung danken. Besonders möchte ich meinen Großeltern dafür danken, dass sie immer an mich geglaubt haben. Ich wünschte ihr wärt hier.

Last, but by no means least, bin ich zwei ganz besonderen Menschen in meinem Leben zu Dank verpflichtet: Bettina & Oliver, danke, dass ihr immer da wart. Ich hab euch lieb.

EIDESSTATTLICHE ERKLÄRUNG / STATUTORY DECLARATION

“Hiermit erkläre ich an Eides statt, dass ich die vorliegende Dissertation selbständig und ohne Hilfe verfasst und keine anderen als die angegebenen Hilfsmittel und Quellen benutzt habe. Wörtlich oder inhaltlich entnommene Stellen habe ich als solche kenntlich gemacht.”

Potsdam, im November 2012

“I herewith formally declare that I myself have independently written the submitted dissertation. I did not use any outside support except for the cited literature and all the other quoted sources which I employed producing this academic work, either literally or in content.”

Potsdam, November 2012

Stefan Glatzel